

Human Hand Neuromechanics for the Design of Robotic Intelligent Upper Limb Protheses

Von der Fakultät für Elektrotechnik und Informatik
der Gottfried Wilhelm Leibniz Universität Hannover
zur Erlangung des akademischen Grades

Doktor-Ingenieurin

(abgekürzt Dr.-Ing.)

genehmigte Dissertation

von Frau
M. Sc. Jumana Ma'touq

geboren am 13.06.1985
in Amman, Jordan

2019

Referent Prof. Dr.-Ing. Matthias Müller
Korreferent Prof. Dr.-Ing. Christof Hurschler

Tag der Promotion 21.10.2019

Printed and/or published with the support of the German Academic Exchange Service

Acknowledgement

Undertaking this Ph.D. has been the most challenging chapter of my life and truly life-changing experience. Though only my name appears on the cover of this dissertation, it would not have been possible to write it without the help and support of the kind people around me, to only some of whom it is possible to give a particular mention here.

First and foremost, I express my sincere appreciation to my supervisor Prof. Dr.-Ing. Matthias Müller, Prof. Dr.-Ing. Bernardo Wagner, and Dr.-Ing. Torsten Lilje. I cannot thank them enough for everything that they have done to make this work possible. Their helping hand, support, and patience paved the way to the completion of this dissertation. I know without your support the final stages of this dissertation would have never seen the light as it is today. I would also like to extend thanks to Prof. Dr.-Ing. Christof Hurschler for his expert advice and extraordinary support during this research. I am amazed that even during his busy schedule, he never said no, instead he was always willing to help me with my dissertation. Thank you, for your valuable time, co-operation, and generosity which made this work possible.

I would like to thank the German Academic Exchange Service (Deutscher Akademischer Austauschdienst DAAD) for the financial support and giving me the rare opportunity to pursue my Ph.D. in Germany. Being awarded the "Research Grants - Doctoral Programmes in Germany, DAAD 2015/2016" has definitely broadened my research perspective and enriched my personal skills. Doing my research in such an inspiring and demanding environment has pushed me to new heights and opened my eyes on new research perspectives. On the personal level, this has enriched my communication skills with diverse communities, and allowed me to discover personal characteristics that I could not have experienced in my comfort zone.

I am always indebted to my family, to whom this dissertation is dedicated, for their unending love, respect, support, and encouragement in all stages of my life. I would not be here if not for you. Thank you for being a constant source of strength and inspiration to me especially in the hard moments of my Ph.D. I have to give a special mention for my uncle and role model Prof. Adel Al Khatib for his continued support and inspiration. Thank you for being close to me each time I needed you.

Many friends and colleagues have helped me to focus on my studies and adjust to the new country. Their support and care helped me to overcome life obstacles during my four years in Germany. My special thanks go to Hala, Hassan, Iyad, Nasim, Ruba, Johannes, Anne-Sophie, Dunia M., Rima, Dunia H., Hazim, Erfan, and Fernando. I have to give special thanks to Krystyna, Rasha, Suzan, Abdulwahab, and Judy for being my family here.

Hanover, Oct. 2019

Kurzfassung

Das Verständnis der menschlichen Neuromechanik ist der erste Schritt zu einer Übertragung der menschlichen Fähigkeiten und des Verhaltens auf intelligente, menschenähnliche Robotersysteme. Das Ziel dieser Arbeit ist die Entwicklung eines neuromuskuloskelettalen Modells der menschlichen Hand, das als Werkzeug zum Verstehen und Nachbilden menschlichen Verhaltens dient. In dieser Arbeit werden fünf Modelle der menschlichen Hand vorgestellt, und zwar die Skelettkinematik und -dynamik, die Kinematik und Dynamik der Muskel-Sehnen-Einheit, sowie die Schätzung der Muskelaktivierung. Das kinematische Modell des Skeletts besteht aus 26 Freiheitsgraden, welches die fünf Finger und den Mittelhand-Bogen beinhaltet. Das Modell schätzt die Gelenkwinkel aus Daten der Bewegungsanalyse (Motion Tracking) basierend auf einer Abbildung zwischen oberflächlichen Markern und den geschätzten Drehzentren der Gelenke. Für die Dynamik auf skelettaler Ebene werden sowohl das Drehmoment jedes Gelenks, aufgrund von Gravitations- und Trägheitskräften, als auch das passive Drehmoment aufgrund der passiven Gelenkeigenschaften geschätzt. Das kinematische Modell liefert die Längen der Muskel-Sehnen-Einheit, die Längenänderungsraten und die Hebelarme der Auslenkung als Funktion der Gelenkconfiguration. Für das Modell der Muskel-Sehnen-Einheit wird ein Hill-Modell verwendet, welches die Muskelkräfte für gegebene Längen der Einheit, die Längenänderungsrate und die Muskelaktivierung prädiziert. Die Länge und ihre Änderungsrate werden aus dem vorgestellten kinematischen Muskel-Sehnen-Modell bestimmt, während die Muskelaktivierung mit Hilfe des Muskelaktivierungsmodells geschätzt wird. Mit diesem Modell werden die Muskelaktivierungen durch Minimierung der Differenz zwischen dem resultierenden Drehmoment aus dem dynamischen Muskel-Sehnen-Modell und dem skelettalem dynamischen Modell bestimmt. Die vorgeschlagenen Modelle wurden entweder experimentell mit einem Motion-Tracking-System oder durch Vergleich der Modellergebnisse mit verfügbaren Kadavermessungen bzw. experimentellen Messungen aus der Literatur validiert. Die sich ergebende Differenz zwischen den gemessenen und geschätzten Oberflächenmarkern liegt im Submillimeterbereich und zeigt, dass das vorgeschlagene skelettkinematische Modell und die zugehörigen Identifikationsverfahren konsistent und hochgenau sind. Die hohe Ähnlichkeit (Ähnlichkeitskoeffizient $s \geq 0.70$ für 92% der Fälle) zwischen den modellierten Hebelarmen und den aus der Literatur verfügbaren Kadavermessungen deuten auf die Korrektheit der modellierten Hebelarme hin und implizieren eine ausreichende Genauigkeit der modellierten Muskel-Sehnen-Bahnen, Längen und Längenänderungsraten. Abschließend wird die Gesamtkonsistenz zwischen den vorgeschlagenen fünf Modellen demonstriert, welche die Qualität der entwickelten Modelle unterstreicht.

Schlagworte: Handkinematik, Gelenkwinkel, Aktivierungsschätzung, Muskel-Sehnen-Bahnen, Handdynamik

Abstract

Understanding human neuromechanics is the first step in transforming human capabilities and behaviour into smart human-like robotic systems. The aim of this thesis is to develop a human hand neuromusculoskeletal model that serves as a tool in understanding and replicating human behaviour. In this thesis, five models of the human hand are proposed, i.e. skeletal kinematics, skeletal dynamics, musculotendon kinematics, musculotendon dynamics, and muscle activation estimation. The skeletal kinematic model is a 26 degree of freedom model that includes the five digits and the palm arc. It estimates skeletal joint rotational angles from motion tracking data based on mapping functions between surface landmarks and the estimated joint centres of rotation. In the skeletal dynamic model, both the link torque due to gravitational and inertial forces and the passive torque due to the passive joint properties are estimated. The musculotendon kinematic model calculates musculotendon lengths, length change rates, and musculotendon excursion moment arms as a function of joint configuration. The musculotendon dynamic model used is a Hill-type muscle model that predicts the musculotendon forces for given musculotendon lengths, length change rates, and muscle activations. The musculotendon length and its rate of change are obtained from the proposed musculotendon kinematic model while muscle activations are obtained from the proposed muscle activation estimation model. Using this model, muscle activations are optimised by minimising the difference between the torque resulting from the musculotendon dynamic model and skeletal dynamic model. The proposed models were validated either experimentally using a motion tracking system or by comparing model results with available cadaver/experimental measurements taken from the literature. The sub-millimetre difference between measured and estimated surface markers indicates that the proposed skeletal kinematic model and associated identification procedure are consistent and highly accurate. The high similarity (similarity coefficient $s \geq 0.70$ for 92% of cases) shown between the modelled moment arms and available cadaver measurements from the literature suggests the correctness of the modelled moment arms, and implies the feasibility of the modelled musculotendon paths, lengths, and length change rates. Finally, the overall consistency between the five models proposed will be demonstrated and highlights the quality of the developed models.

Keywords: Hand kinematics, joint centre of rotation, activation estimation, musculotendon path, hand dynamics

Contents

Acknowledgments	vi
List of Figures	xv
List of Tables	xxi
Abbreviations	xxv
Symbols	xxx
1 Introduction	1
1.1 Motivation	1
1.2 Aim and objectives	2
1.3 Chapter-by-chapter overview	3
2 Skeletal kinematics and dynamics	6
2.1 Introduction	6
2.1.1 Human hand biomechanics	6
2.1.2 Skeletal kinematic model	7
A Model DoFs	9
B Thumb modelling	9
C Centres of rotation estimation	10
D Palm arc modelling	10
E Experimental set-up	11
2.1.3 Skeletal dynamic model	11
2.1.4 Contribution	13
2.2 Methods	14
2.2.1 Skeletal kinematic model	14
A Modelling assumptions	14
A.1 Thumb	14
A.2 Palm arc	15
B Surface and skeletal kinematics model	15
B.1 Intra-level mappings: surface kinematics	17
B.2 Intra-level mappings: skeletal kinematics	20
B.3 Inter-level mappings	21
C Estimation of h_i	21
C.1 DIP joint	24
C.2 PIP joint	24
C.3 MCP joint	25
D Model identification and validation	25
D.1 Algorithmic identification procedure	26

D.2 Experimental set-up	27
2.2.2 Skeletal dynamic model	29
A Link torque	29
B Passive torque	31
B.1 Damping torque	32
B.2 Stiffness torque	33
2.3 Results and discussion	34
2.3.1 Skeletal kinematic model	34
A Joint CoR estimation	34
B Palm arc modelling	34
C Thumb modelling	35
C.1 Rotational relationship between $\{BT\}$ and $\{BH\}$	36
C.2 Thumb model DoFs and accuracy	37
D Surface kinematics and skeleton kinematics	39
D.1 Segment lengths	39
D.2 Joints rotational angles	40
D.3 Errors in Cartesian space	43
2.3.2 Skeletal dynamic model	43
2.4 Conclusion	47
3 Musculotendon kinematics and dynamics	49
3.1 Introduction	49
3.1.1 Biomechanics of skeletal muscle	50
3.1.2 Musculotendon kinematic model	52
A Skeletal kinematic model	54
B Included muscles	55
C Software platform	55
3.1.3 Musculotendon dynamic model	56
A Activation dynamics	57
B Muscle contraction dynamics	57
3.1.4 Contribution	58
3.2 Methodology	62
3.2.1 Musculotendon kinematic model	62
A Mathematical model	62
A.1 Musculoskeletal model	62
A.2 Musculotendon lengths	64
A.3 Musculotendon excursion moment arms	71
A.4 Musculotendon length change rates	72
B Computational model	72
C Model validation	73
3.2.2 Musculotendon dynamic model	74
A Mathematical model	74
B Model parameters	78
C Muscle activation estimation	80
D Model validation	81

3.3 Results and discussion	82
3.3.1 Musculotendon kinematic model	82
3.3.2 Musculotendon dynamic model	86
A Mathematical Hill-type muscle model	86
B Model parameters	86
C Musculotendon force and torque	87
D Muscle activation estimation	89
3.4 Conclusion	92
4 Summary and future work	93
Appendix A Solving for rotational angles	99
Bibliography	101
Publications	116
Curriculum Vitae	118

List of Figures

1.1	Example of the neuromusculoskeletal system function and its forward model. This model consists of five steps: 1) a neural signal arrives to the muscle, 2) the muscle contracts (force production), 3) the muscle force results in joint torques, 4) the joint torques change joint configurations (trajectories), and 5) the movement happens.	2
1.2	Block diagram of the proposed human hand neuromusculoskeletal model, which includes the corresponding chapter number of this thesis. The chapter-by-chapter overview is explained in details in Section 1.3. The symbols \mathbf{q} , $\dot{\mathbf{q}}$, $\ddot{\mathbf{q}}$ denote the angular position, velocity, and acceleration, respectively; τ_{Link} is the link torque; τ_p is the passive torque; τ is the total torque computed from the skeletal dynamic model; \mathbf{J}^T is the matrix of musculotendon excursion moment arms; l_{mt} and \dot{l}_{mt} are the musculotendon unit length and length change rates (shortening/lengthening velocity), respectively; \mathbf{F}_{pe} and \mathbf{F}_{ce} are the passive element force and contractile element force, respectively; \mathbf{u} is the estimated muscle activation; \mathbf{F}_{ce}^* is the contractile element force calculated during the optimisation; and τ_{mt} is the estimated musculotendon unit torque.	4
2.1	Joints and bones of the human hand. Adapted from Lippert (2011). Finger bones are connected with the carpometacarpal (CMC), metacarpophalangeal (MCP), proximal interphalangeal (PIP), and distal interphalangeal (DIP) joints. The thumb has only one interphalangeal (IP) joint.	7
2.2	The DoFs of the MCP joint of the 2 nd – 5 th digits (left) and the CMC joint of the thumb (right). Adapted from Lippert (2011).	8
2.3	The proposed human hand kinematic model with 26 DoFs; 25 actuated DoFs and 1 passive DoF (indicated by “*”). Left: representation of the serial linkages for each digit, which is assumed to be a rigid body segment. Right: the coordinate systems (CS) of the thumb, the index finger (which is similar to the middle finger), the ring finger (which is similar to the pinky finger), and the hand base. The index and middle fingers have 5 CS, while the ring finger, the pinky finger, and the thumb have 7 CS. The alphabet in the CS naming indicates the digit initial.	16

2.4	Two-dimensional finger schematic diagram. A surface link vector \mathbf{L}_\square changes its length during F/E whereas that of a skeletal link vector \mathbf{l}_\square is constant. Bone lengths, $l_\square = \ \mathbf{l}_\square\ $, are calculated from the anthropometric model of Buchholz et al. (1992).	17
2.5	Illustration of the classical D-H convention of the index finger at the surface kinematics level. Top: representation of the links and joints. Bottom: description of the classical D-H convention parameters.	18
2.6	Block diagram of model identification and validation. The symbols are defined in the symbol list. Bone lengths $\{\mathbf{l}_\square\}$ are calculated from the anthropometric model of Buchholz et al. (1992). Both the hand length HL and joint thickness $\ \mathbf{h}_i\ $ are measured for each subject.	26
2.7	Marker placement and labelling. Markers were labelled to indicate the joint names and the digit numbers (1: thumb, 2: index, ..., 5: pinky). A reference marker cluster (BHx-BH0-BHy) was attached to the dorsal side of the hand to establish the hand floating base coordinate system $\{\text{BH}\}$. Another marker cluster (BTx-BT0-BTy) was attached to the base of the first metacarpal bone to establish the thumb reference coordinate system $\{\text{BT}\}$	27
2.8	Experimental subject posture.	29
2.9	Experimental static and dynamic tasks. The static tasks are: S1: relaxed reference posture with all joints extended, and S2: grasping a small paper clip by thumb and pinky digits (thumb-pinky opposition). The dynamic tasks are: D1: MCP joints Ab/Ad, D2: grasp/release a cylinder with diameter of 80 mm, and D3: grasp/release a cylinder with diameter of 40 mm.	30
2.10	CoRs and surface marker locations during Task D2 for one exemplar subject.	36
2.11	Comparison between measured and estimated \mathbf{X}_i in two palm arc models for CMC5 joint during thumb-pinky opposition task (Task S2 in Figure 2.9). Top: modelling the CMC5 joint as static joint (without considering the palm arc). Bottom: modelling the CMC5 joint as 2 DoF joint (with considering the palm arc). The figure shows the pinky finger expressed in $\{\text{BH}\}$	37
2.12	Maximum error (E_i) in the static joint model of CMC5 joint, where the palm arc is not considered. The error is expressed in terms of the Euclidean norm between estimated and measured \mathbf{X}_i in Task S2 (thumb-pinky opposition). Due to a measurement error, the data of subject 3 are not available for analysis in this task.	38
2.13	Comparison between measured and estimated \mathbf{X}_i expressed in $\{\text{BH}\}$ for 4 DoF (left), 5 DoF (middle), and 6 DoF (right) models. The upper row shows a representation of the serial linkage of the compared three models. The numbers between parentheses represent the difference in terms of the Euclidean norm between the estimated and measured \mathbf{X}_i	39

2.14	Comparison between $\ \mathbf{L}_{\square}\ $ and the estimated $\ \mathbf{l}_{\square}\ $ in Task D1 (left) and Task D2 (right). This figure shows segment lengths of an exemplar index finger. The estimated $\ \mathbf{l}_{\square}\ $ are calculated as the distance between the estimated CoRs at the proximal and distal ends of the segment for each time point. The anthropometrically modelled segment lengths are calculated using the model proposed by Buchholz et al. (1992).	41
2.15	Skeleton rotational angles q_k with respect to surface rotational angles Q_k in Task D2. Columns indicate fingers (left to right): index, middle, ring, and pinky. Rows indicate rotational angles (top to bottom): DIP F/E, PIP F/E, MCP F/E. For MCP Ab/Ad, the rotational angles at the surface and skeleton levels are equal with $R^2 = 1.000$, thus they are not shown in this figure.	42
2.16	Skeleton rotational angles q_k with respect to surface rotational angles Q_k in Task D3. Columns indicate fingers (left to right): index, middle, ring, and pinky. Rows indicate rotational angles (top to bottom): DIP F/E, PIP F/E, MCP F/E. For MCP Ab/Ad, the rotational angles at the surface and skeleton levels are equal with $R^2 = 1.000$, thus they are not shown in this figure.	42
2.17	Comparison between measured and estimated \mathbf{X}_i in Task D2 for an exemplar subject at different instants (from T1 to T4). T1: start posture, T2: grasping, T3: start releasing, and T4: complete release.	44
2.18	The resulting link torque τ_{Link} of the four fingers for a simulated repetitive F/E motion (Equation 3.17).	45
2.19	The results of the damping torque τ_d model in the index finger. Top: a simulated repetitive F/E motion for the three joints of the index finger (Equation 3.17). Bottom: the resulting τ_d	46
2.20	The modelled joint stiffness torque τ_s in the three joints of the index finger.	46
2.21	Torque components in the index MCP joint for a given joint configuration. Top: the given MCP joint configuration (Equation 3.17). Middle: the resulting link torque τ_{Link} , damping torque τ_d , and stiffness torque τ_s . Bottom: the resulting total torque, i.e. $\tau_{\text{Link}} + \tau_d + \tau_s$	47
3.1	The connection between the musculotendon kinematic model and the musculotendon dynamic model.	50
3.2	Structure of skeletal muscle. Adapted from Hall (2011).	51
3.3	The sliding filament model. Sliding of the actin chains on the myosin chains results in contraction of the skeletal muscle. Adapted from Oatis (2016).	51
3.4	Length-tension curve. Adapted from Martini et al. (2012).	52
3.5	Steps of excitation-contraction. Adapted from Martini et al. (2012).	53
3.6	The associated time delay between action potential and muscle contraction. Adapted from Linke and Pfitzer (2007) and Hu (2015).	53
3.7	Illustration of the obstacle-set model used to represent the paths of the three heads of the triceps brachii. Adapted from Garner and Pandy (2000).	54

3.8	Graphical representation of obstacle-sets: (A) single sphere, (B) single cylinder, (C) double cylinder, and (D) sphere-capped cylinder. Adapted from Garner and Pandy (2000).	54
3.9	Muscle dynamics, which is divided into activation dynamics and muscle contraction dynamics.	56
3.10	Representation of classical structure of Hill-type muscle model, with contractile element (CE), series element (SE, larger spring) representing the tendon, and parallel element (PE) representing the passive muscle stiffness.	58
3.11	Comparison of different formulations of the Hill-type muscle model.	59
3.12	Modelled extrinsic and intrinsic hand muscles. Table 3.2 provides muscle descriptions and abbreviations.	60
3.13	Proposed complete musculotendon paths and muscle-joint kinematic model.	62
3.14	Three-dimensional visualisation of the proposed 27 muscles/47 musculotendon path model. The 3-D visualisation is implemented in Unity (Unity Technologies, USA).	64
3.15	The musculotendon path is modelled as multiple segments defined by the attachment points. The yellow spheres represent musculotendon origin, via-points, and insertion. The blue spheres denote obstacle via-points and the light blue cylinders denote modelled obstacles. The 3-D visualisation is implemented in Unity.	65
3.16	Graphical representation of the single-cylinder obstacle-set used in this model at the index metacarpophalangeal (MCP2) joint. Top: when MCP2 is at neutral position, no wrapping occurs and the P-S segment is a straight line. Bottom: when MCP2 is flexed, wrapping occurs where the P-Q and Q-S segments are straight lines and the Q-T segment forms an arc. The 3-D visualisation is implemented in Unity.	67
3.17	Flowchart of the single-cylinder obstacle-set algorithm developed by Garner and Pandy (2000).	68
3.18	Illustration of the obstacle cross-section and the geometric conditions. The full musculotendon path is P-Q-T-S with the straight line segments, P-Q and T-S, being tangents to the obstacle surface. There are two possibilities for wrapping: the right-handed sense (solid line) and the left-handed sense (dashed line). Either wrapping direction can be specified using a signed value to the obstacle radius r_O , i.e. positive and negative values for r_O would correspond to right-handed and left-handed wrapping, respectively.	69
3.19	Illustration of the wrapping angle, defined as the angle formed by the arc from Q to T $\angle Q'OT'$. The wrapping condition w_O is <i>true</i> , i.e. $\angle Q'OT' \leq 180^\circ$, and Q and T are <i>active</i> (left and middle). Otherwise w_O is <i>false</i> and Q and T are <i>inactive</i> (right).	70
3.20	The representation of a Hill-type muscle model (left) versus the simplified Hill-type muscle model used in this thesis (right). The simplified model considers the tendon rigid with $l_{t,o} = \text{constant}$ and the pennation angle α_m is zero.	75

3.21	Illustration of the physiological muscle length. The effective operating range of a muscle to produce an active force is roughly between $0.5l_{m,o}$ and $1.5l_{m,o}$. A passive force is generated when a muscle is stretched between $1.2l_{m,o}$ and $1.7l_{m,o}$. Thus, the overall physiological muscle length ranges between $0.5l_{m,o}$ and $1.7l_{m,o}$	80
3.22	Block diagram of the proposed muscle activation model.	81
3.23	Comparison between modelled and measured moment arms (MA) with respect to the index finger metacarpalphalangeal joint (MCP2) degrees of freedom. The two degrees of freedom are presented by flexion/extension (F/E) and abduction/adduction (Ab/Ad).	83
3.24	Comparison between modelled and measured moment arms (MA) with respect to the thumb carpometacarpal (CMC) joint degrees of freedom. These two degrees of freedom are presented by flexion/extension (F/E) and abduction/adduction (Ab/Ad). Error bars denote standard deviations (95% rule in statistics).	84
3.25	Comparison between modelled and measured moment arms (MA) with respect to the thumb metacarpalphalangeal (MCP) and interphalangeal (IP) joint degrees of freedom. The two degrees of freedom are presented by flexion/extension (F/E) and abduction/adduction (Ab/Ad). Error bars denote standard deviations (95% rule in statistics).	85
3.26	Model characteristics: active and passive force–length, and force–velocity relationships.	86
3.27	Normalised muscle length $l_m/l_{m,o}$ for the extrinsic and intrinsic index finger muscles in resting posture (Task S1 in Figure 2.9).	87
3.28	Normalised muscle length $l_m/l_{m,o}$ for a simulated index finger joint flexion/extension motion. Top: the simulated flexion/extension motion, which is obtained using sinusoidal functions as in Equation 3.17. Middle and bottom: the normalised muscle length during the motion for the extrinsic and intrinsic index finger muscles, respectively.	88
3.29	The resulting F_{pe} and $\tau_{mt,pe}$ at the index finger MCP joint. The passive musculotendon torque resulting from the proposed model is compared to the modelled torque from the literature (Kuo and Deshpande 2012).	90
3.30	The resulting muscle activations, forces, and torque for a simulated MCP2 F/E motion. This motion is obtained using sinusoidal functions (Equation 3.17).	91
4.1	Block diagram of the proposed human hand neuromusculoskeletal model illustrates the corresponding objectives.	93

List of Tables

2.1	State-of-the-art hand kinematic models.	11
2.2	The compared thumb models. The passive DoF is indicated by “*”.	15
2.3	D-H parameters of surface kinematics. The offset length D_k is calculated as the translation along the z_k -axis using the optoelectronic motion capture data.	22
2.4	D-H parameters of skeletal kinematics. The offset length d_k is fitted using polynomial regression as a function of q_k (Figure 2.6).	23
2.5	The anthropometric properties of the human hand.	31
2.6	Joint damping coefficients.	32
2.7	State-of-the-art hand stiffness models.	33
2.8	Joint stiffness coefficients.	35
2.9	Comparison of accuracy among different thumb models from literature. The error was calculated as the maximum error of fingertip (Miyata et al. 2004), maximum of the errors in x -, y -, and z -directions (Cordella et al. 2014), and RMS error of the distance between estimated and measured marker positions (Cerveri et al. 2007).	40
2.10	Comparison of accuracy among different finger models (2 nd – 5 th digits) from the literature. The error E_i was calculated as the maximum error of fingertip (Miyata et al. 2004), maximum of the errors in x -, y -, and z -directions (Cordella et al. 2014), and RMS error of the distance between estimated and measured marker positions (Cerveri et al. 2007).	43
3.1	State-of-the-art hand musculoskeletal models and the contribution of the present work.	56
3.2	Modelled human hand muscles. The anatomical descriptions of muscles are based on Lippert (2011).	61
3.3	Index finger muscles pennation angle α_m [°]	76
3.4	The state-of-the-art of muscle modelling parameters.	79
3.5	The calculated tendon slack length.	87
4.1	Summary of the contributions and future work of the models proposed in this thesis.	97

Abbreviations

Ab/Ad	Abduction/adduction
AbDM	Abductor digiti minimi
AbPB	Abductor pollicis brevis
AbPL	Abductor pollicis longus
AdPt/AdPo	Adductor pollicis
CE	Contractile element (Hill-type muscle model)
CLC	Capsule ligament complex
CMC	Carpometacarpal joint
CMC1	Carpometacarpal joint of the thumb
CMC4	Carpometacarpal joint of the ring finger
CMC5	Carpometacarpal joint of the pinky finger
CoR(s)	Centre(s) of rotation
CS	Coordinate systems
D-H	Denavit-Hartenberg
DI	Dorsal interossei
DIP	Distal interphalangeal joint
DoF(s)	Degree(s) of freedom
EDC	Extensor digitorum (communis)
EDM	Extensor digiti minimi
EIP	Extensor indicis (proprius)
EPB	Extensor pollicis brevis
EPL	Extensor pollicis longus
FDM	Flexor digiti minimi
FDP	Flexor digitorum profundus
FDS	Flexor digitorum superficialis
FPB	Flexor pollicis brevis

FPL	Flexor pollicis longus
F/E	Flexion/extension
IP	Interphalangeal joint
ISB	The International Society of Biomechanics
LU	Lumbricals
MCP	Metacarpophalangeal joint
MCP1	Metacarpophalangeal joint of the thumb
MCP2	Metacarpophalangeal joint of the index finger
ODM	Opponens digiti minimi
OMC	Optoelectronic motion capture
OP	Opponens pollicis
PCSA	Physiological cross-sectional area
PE	Parallel element (Hill-type muscle model)
PI	Palmar interossei
PIP	Proximal interphalangeal joint
RoM	Range of motion
SE	Series element
sEMG	Surface electromyography
TM	Trapeziometacarpal joint
2-D	Two dimensional
3-D	Three dimensional

Symbols

Skeletal kinematics

$\{\mathbf{BH}\}$	Hand base frame
$\{\mathbf{BT}\}$	Thumb base frame
$\{\mathbf{B}\}$	Base frames, i.e. $\{\mathbf{BH}\}$ or $\{\mathbf{BT}\}$
$\mathbf{BT0}$	Surface landmark of the $\{\mathbf{BT}\}$ origin
$d_k(t)$	Translation along z -axis between two CoRs (D-H convention)
$d_k(q_k)$	Fitted translation along z -axis between two CoRs (D-H convention)
$D_k(t)$	Translation along z -axis between two surface landmarks (D-H convention)
$f(\cdot)$	Surface forward kinematic function
$f^{-1}(\cdot)$	Surface inverse kinematic function
$g(\cdot)$	Skeletal forward kinematic function
$g^{-1}(\cdot)$	Skeletal inverse kinematic function
h_i	Vector pointing from the joint CoR to the corresponding skin landmark
$\ h_i\ $	Thickness of joint i (constant)
HL	Hand length
\mathbf{L}_{\square}	Segmental vectors in surface kinematics between two surface landmarks. \mathbf{L}_{DP} : surface segmental vector of distal phalanx. \mathbf{L}_{MP} : surface segmental vector of middle phalanx. \mathbf{L}_{PP} : surface segmental vector of proximal phalanx
l_{\square}	Segmental vectors in skeleton kinematics between two joint CoR. l_{DP} : skeletal segmental vector of distal phalanx. l_{MP} : skeletal segmental vector of middle phalanx. l_{PP} : skeletal segmental vector of proximal phalanx

Q	Surface joint configuration vector
Q_k	Rotational angle in surface kinematics (Table 2.3)
q	Skeletal joint configuration vector
q_k	Rotational angle in skeleton kinematics (Table 2.4)
${}^{BH}R_{BT}$	Rotational matrix between $\{BH\}$ and $\{BT\}$
${}^WR_{BH}$	Rotational matrix between $\{W\}$ and $\{BH\}$
R_x, R_y, R_z	Basic rotational matrices about x -, y -, and z -axis, respectively
${}^{BH}T_{BT}$	Transformation matrix between $\{BH\}$ and $\{BT\}$
${}^{k-1}T_k$	Transformation matrix between $\{k\}$ and $\{k-1\}$ in surface kinematics
${}^{k-1}t_k$	Transformation matrix between $\{k\}$ and $\{k-1\}$ in skeletal kinematics
X_i	Cartesian position of skin landmark i
\hat{X}_i	Estimated Cartesian position of skin landmark i
${}^{BH}X_{BT0}$	The vector pointing from the origin of $\{BH\}$ to the origin of $\{BT\}$
kX_i	Cartesian position of skin landmark i expressed in $\{k\}$
${}^{k-1}X_i$	Cartesian position of skin landmark i expressed in $\{k-1\}$
WX_i	Cartesian position of skin landmark i expressed in $\{W\}$
x_i	Cartesian position of joint CoR i
\hat{x}_i	Estimated Cartesian position of CoR i
kx_i	Cartesian position of CoR i expressed in $\{k\}$
${}^{k-1}x_i$	Cartesian position of CoR i expressed in $\{k-1\}$

Skeletal dynamics

$c(q, \dot{q})$	Centrifugal and Coriolis vector
$g(q)$	Gravitational torque
K	Joint damping coefficient vector
l	Bone body length
$M(q)$	Mass matrix
m_{\square}	Bone body mass

$\mathbf{q}, \dot{\mathbf{q}}, \ddot{\mathbf{q}}$	Angular position, velocity, and acceleration, respectively
r_{\square}	Bone body radius
V_{\square}	Volume of the bone body and considered as the volume of a cylinder
ρ	Human body density
τ_{Link}	Joint link torque
τ_{p}	Joint passive torque
τ_{d}	Joint damping torque
τ_{s}	Joint stiffness torque
$\tau_{\text{mt,pe}}$	Joint torque due to passive musculotendon force
τ_{ext}	Joint torque due to environmental interaction force
τ_{mt}	Joint torque due to total musculotendon force

Musculotendon kinematics

$\mathbf{J}^{\text{T}}(\mathbf{q})$	Musculotendon excursion moment arms matrix
$l_{\text{m}}(\mathbf{q})$	Muscle lengths
$l_{\text{mt}}(\mathbf{q})$	Musculotendon lengths
$\dot{l}_{\text{m}}(\mathbf{q}, \dot{\mathbf{q}})$	Muscle lengths change rates (shortening/lengthening velocity)
$\dot{l}_{\text{mt}}(\mathbf{q}, \dot{\mathbf{q}})$	Musculotendon lengths change rates (shortening/lengthening velocity)
$l_{\text{mt},i}(\mathbf{q})$	Length of a musculotendinous unit i
$l_{\text{mt},i}^{\text{Seg},n}(\mathbf{q})$	Length of the n -th segment of the i -th musculotendon's n -th segment
$l_{\widehat{Q'T'}}$	Length of the curved line segment Q-T in the x-y plane of $\{O\}$
$l_{\widehat{QT}}$	Length of the curved line segment Q-T in 3-D
$\{O\}$	Cylinder reference frame
P	Bounding-fixed point
Q	Obstacle via-point
$\mathbf{q}, \dot{\mathbf{q}}, \ddot{\mathbf{q}}$	Angular position, velocity, and acceleration, respectively

$\angle Q'OT'$	Wrapping angle, i.e. the angle formed by the arc from Q to T
$\mathbf{R}_O \in \mathbb{R}^3$	Orthonormal rotation matrix describing obstacle orientation
$r_O \in \mathbb{R}$	Obstacle radius
S	Bounding-fixed point
s	Similarity coefficient
T	Obstacle via-point
${}^O\mathbf{T}_W$	Transformation matrix from {W} to {O}
{W}	World reference frame
w_O	Wrapping condition
$\mathbf{X}_O \in \mathbb{R}^3$	Cartesian position of the obstacle centre

Musculotendon dynamics

\mathbf{F}_{ce}	Contactile element (CE) force
\mathbf{F}_{mt}	Musculotendon force
\mathbf{F}_{pe}	Parallel element (PE) force
\mathbf{F}_{max}	Maximum voluntary isometric contraction force
f_1^{ce}	Force-length relation of CE
f_v^{ce}	Force-velocity relation of CE
f_1^{pe}	Force-length relation of PE
$l_m(\mathbf{q})$	Muscle lengths
$l_{t,o}$	Tendon slack lengths
$l_{m,o}$	Optimal muscle lengths
$l_{mt}(\mathbf{q})$	Musculotendon lengths
$\dot{l}_{mt}(\mathbf{q}, \dot{\mathbf{q}})$	Musculotendon lengths change rates (shortening/lengthening velocity)
$l_{mt,max}$	Maximum muscle physiological length
$l_{mt,min}$	Minimum muscle physiological length
\tilde{l}_m	Normalised muscle length for a single muscle
m_m	Muscle mass
S	Maximum muscle stress

u	Muscle neural activation
Vol_m	Muscle volume
α	Muscle pennation angle
ρ	Muscle density
τ_{mt}	Musculotendon torque
$\tau_{mt,pe}$	Passive musculotendon torque

Chapter 1

Introduction

1.1 Motivation

Bio-inspired robotic systems have opened up entirely new application domains that were not possible before. Studying and replicating human behaviour can provide new insights into safe human-robot interaction, assistive devices, rehabilitation manipulators, as well as prosthetic and orthotic devices. In order to develop such systems, a thorough understanding of human neuromechanics is the first step in transforming human capabilities and behaviour as well as new methods and robotic technologies into smart human-like robotic systems. In particular, the analysis and evaluation of human hand neuromechanics is essential for understanding human hand movements to implement grasping strategies, manipulations, reflexes, and synergies in human-like smart prostheses.

Typically, the neuromechanical analyses rely on neuromusculoskeletal models, which include the description of anatomical and physiological features. The anatomical features include lengths of the actuators (musculotendon lengths), musculotendon excursion moment arms, geometry of the bones, and the lines of action of the actuators (Van Campen 2014). The physiological features describe how the muscles produce force and how it is transferred by the tendons (Van Campen 2014). In other words, the neuromusculoskeletal models describe the interaction between three basic anatomical structures, i.e. the skeleton, the muscles, and the neurones in a model with three levels (Figure 1.1).

The forward neuromusculoskeletal model that describes the system from neural activation to motion production is straight forward only if the neural signal is known (Figure 1.1). It can be estimated non-invasively, for instance, by means of surface electromyography (sEMG). The sEMG is a technique in which electrodes are placed on the skin overlying a muscle to detect the electrical activity of the muscle. However, sEMG has the limitations of: 1) impossibility of measuring all hand muscles, i.e. deep or intrinsic muscles, 2) the likelihood of “cross-talk”, which makes it difficult or even impossible to isolate the sEMG recordings for a specific muscle (Cram and Kasman 1998b), and 3) the existence of skin movement artefacts. Alternatively, mathematical models have been applied to estimate

the neural activation from captured motion dataset as proposed in this thesis. The proposed neuromusculoskeletal model consists of five models: skeletal kinematics, skeletal dynamics, musculotendon kinematics, musculotendon dynamics, and muscle activation estimation. These five models describe the interaction between the three anatomical structures (i.e. the skeleton, the muscles, and the neurones) while performing a specific motion (Figure 1.2).

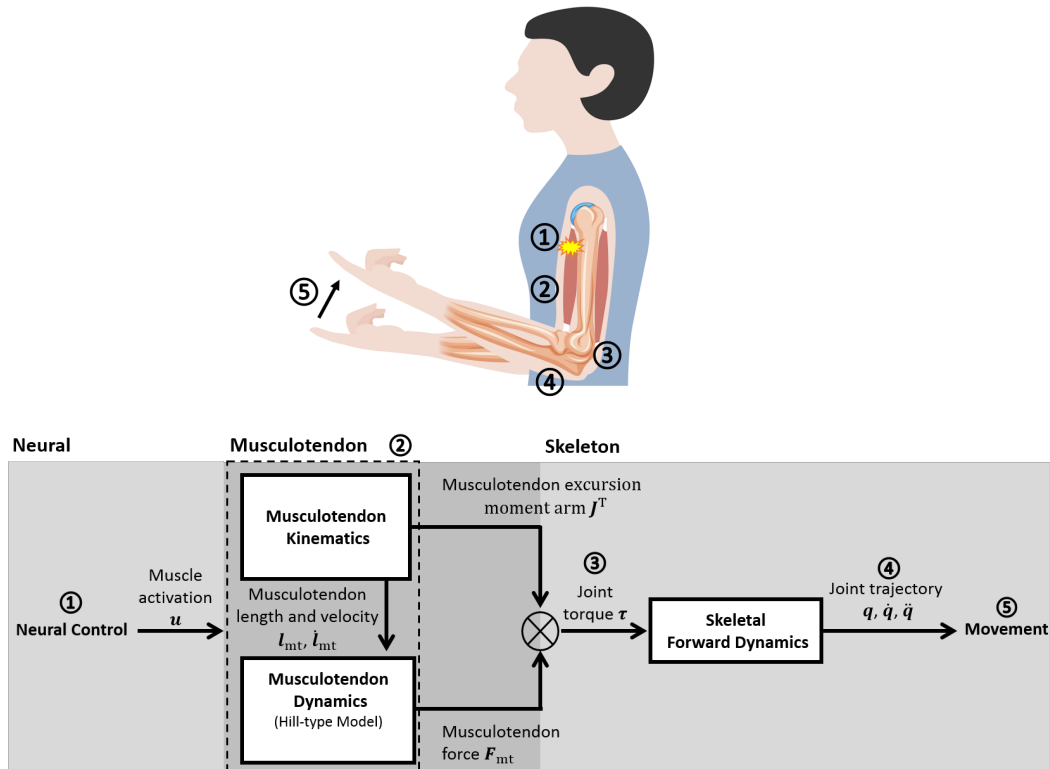


Figure 1.1: Example of the neuromusculoskeletal system function and its forward model. This model consists of five steps: 1) a neural signal arrives to the muscle, 2) the muscle contracts (force production), 3) the muscle force results in joint torques, 4) the joint torques change joint configurations (trajectories), and 5) the movement happens.

1.2 Aim and objectives

The aim of this thesis is to develop a human hand neuromusculoskeletal model that serves as a tool in studying and replicating human behaviour. In particular, the focus of this work can be summarised in five modelling steps (Figure 1.2):

1. Develop a complete highly accurate 26 degree of freedom (DoF) human hand kinematic model. This model includes the four fingers (4 DoFs each), the thumb (6 DoFs), and the palm arc (4 DoFs) based on mapping functions between surface landmarks and estimated joint centre of rotation (CoR), which are estimated using a novel algorithm.

2. Enhance the human hand skeletal dynamic models previously developed in the literature. In particular, A skeletal dynamic model is developed, which is consistent with the proposed musculoskeletal kinematic model and includes the passive visco-elastic properties of finger joints.
3. Develop a complete computational model for musculotendon paths and muscle-joint kinematics. This model includes all intrinsic and extrinsic muscles, which are represented by 47 musculotendon paths. The model takes joint angles as an input and estimates musculotendon lengths, length change rates, and excursion moment arms.
4. Propose a musculotendon dynamic model for the index finger. A Hill-type muscle model is utilised that predicts the musculotendon forces for given musculotendon lengths and length change rates, which are obtained from the musculotendon kinematic model, alongside muscle activations.
5. Propose a muscle activation estimation model for the index finger. This model includes the flexion/extension of the three joints of the index finger. It predicts muscle activation of the seven muscles of the index finger for given joint configurations.

The detailed contribution of each of the five models is presented in the beginning of each model section.

1.3 Chapter-by-chapter overview

The neuromusculoskeletal models describe the interaction between three main structures, i.e. the skeleton, the muscles, and the neurons. In this thesis, the hand neurobiomechanics modelling is limited to muscle activation modelling only and will be discussed and modelled as part of the musculotendon dynamics. Thus, this thesis is structured in two main chapters, each one corresponding to one structure model as follows (Figure 1.2).

Chapter 2. Skeletal kinematics and dynamics. This chapter discusses the kinematic and dynamic models at the skeletal level. The skeletal kinematic model includes forward and inverse models that map joint positions into joint rotations, and vice versa. A systematic flexion/extension CoR estimation algorithm is utilised for this purpose, and mathematically described. Model validation and comparison with different modelling assumptions in the literature are presented. The second section describes the skeletal dynamic model that enhances the human hand skeletal dynamic models previously developed in the literature. In particular, the 16 DoFs human hand link torque model of Serbest et al. (2016) is extended to include the 26 DoFs as implemented in the kinematic model and to furthermore consider the passive visco-elastic properties of the finger joints. The

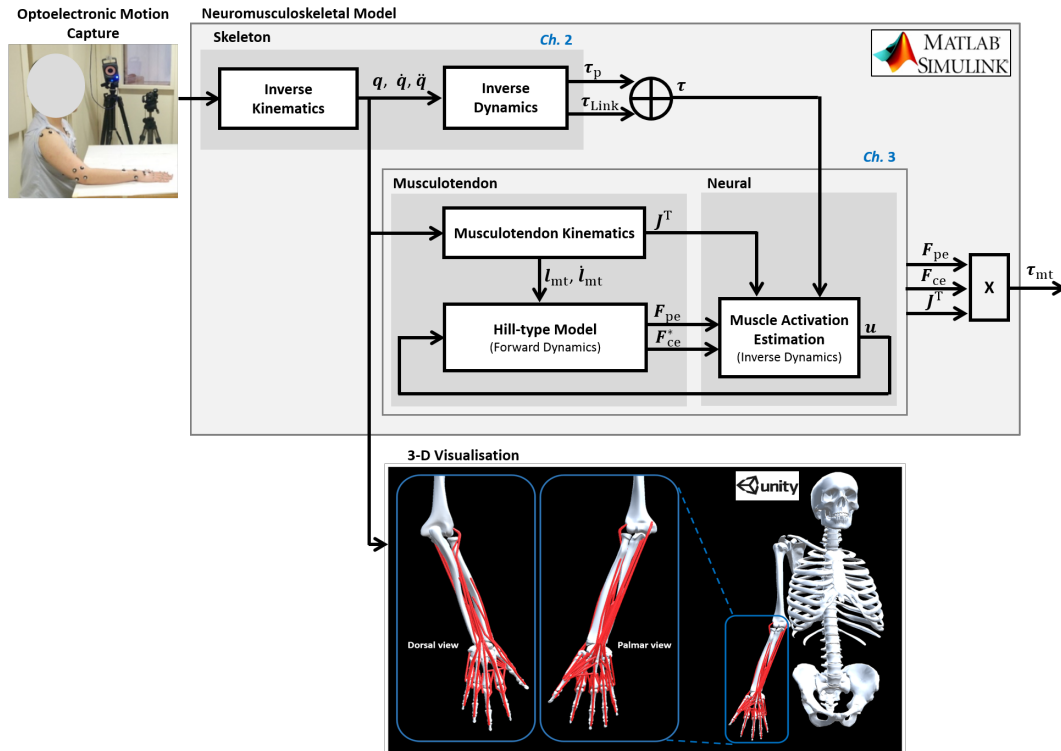


Figure 1.2: Block diagram of the proposed human hand neuromusculoskeletal model, which includes the corresponding chapter number of this thesis. The chapter-by-chapter overview is explained in details in Section 1.3. The symbols q , \dot{q} , \ddot{q} denote the angular position, velocity, and acceleration, respectively; τ_{Link} is the link torque; τ_p is the passive torque; τ is the total torque computed from the skeletal dynamic model; J^T is the matrix of musculotendon excursion moment arms; l_{mt} and \dot{l}_{mt} are the musculotendon unit length and length change rates (shortening/lengthening velocity), respectively; F_{pe} and F_{ce}^* are the passive element force and contractile element force, respectively; u is the estimated muscle activation; F_{ce}^* is the contractile element force calculated during the optimisation; and τ_{mt} is the estimated musculotendon unit torque.

results of the skeletal dynamic model are used in activation estimation model to optimise muscle activations (Chapter 3).

Chapter 3. Musculotendon kinematics and dynamics. This chapter discusses the kinematic and dynamic models of the musculotendon unit. The musculotendon kinematic model estimates length change rates and musculotendon excursion moment arms from musculotendon lengths for different joint configurations. Musculotendon lengths are calculated using the musculotendon path model, which describes the complete route of the musculotendon unit from its origin to its insertion by means of via-points and bony-structure wrapping in 3-D space. The implemented muscle path model including obstacle-set algorithm is also discussed in this section. Model simulation was performed and the resulting moment arms are presented and compared with cadaver measurements

available from the literature in terms of similarity coefficient. The second section explains the mathematics and parameters of the musculotendon dynamic model, which calculates musculotendon forces. The muscle activation model, which connects the proposed models to form the neuromusculoskeletal model, is also discussed in this section. Finally, the resulting muscle activations, forces, and torques are discussed and compared to results available in the literature.

Chapter 4. Summary and future work. This chapter briefly reviews the thesis objectives and outlines the contributions and limitations of the proposed model. Subsequently, it discusses future research opportunities that will enhance and extend the proposed model as well as answer interesting open research questions.

Chapter 2

Skeletal kinematics and dynamics

*Parts of this chapter have been published in
Computer Methods in Biomechanics and Biomedical Engineering, 2018, 21(2): 113-128,
and
The 16th International Symposium on Computer Methods in Biomechanics and
Biomedical Engineering, New York City, United States, Aug 2019.*

2.1 Introduction

2.1.1 Human hand biomechanics

This sub-section explains the human hand biomechanics based on Lippert (2011). In the human hand, each finger (2nd – 5th digits) has four bones and four joints, i.e. distal phalange, middle phalange, proximal phalange, and metacarpal bone (Figure 2.1). These finger bones are connected with joints: carpometacarpal (CMC), metacarpophalangeal (MCP), proximal interphalangeal (PIP), and distal interphalangeal (DIP) joints. The CMC joints are classified as non-axial plane (irregular) synovial joints that provide more stability than mobility. While the second and third CMC are not mobile, the fifth CMC is the most mobile of the fingers and the fourth is slightly mobile. The overall function of the CMC joints is to contribute to the palm arc system (Levangie and Norkin 2005). The MCP joints are biaxial condyloid joints connecting the head of metacarpals with the base of the proximal phalanges. The motions allowed at these joints are flexion/extension (F/E) and abduction/adduction (Ab/Ad) (Figure 2.2). The two interphalangeal joints, i.e. the PIP and DIP joints, are uniaxial hinge joints that allow F/E motion only.

The anatomy of the thumb differs from the other fingers. It consists of only three bones, i.e. the metacarpal bone, the proximal phalange, and the distal phalange, which are connected by the CMC, MCP, and the interphalangeal (IP) joints. The first metacarpal in the thumb articulates with the trapezium, thus it is sometimes called as the trapeziometacarpal joint (TM) instead of CMC (Bullock et al. 2012). The CMC joint of the thumb is a two-

axis joint with non-intersecting, non-orthogonal axes (Hollister et al. 1992). Compared to the CMC joints of the other fingers, the thumb CMC joint has more mobility, i.e. it allows F/E, Ab/Ad, and opposition/reposition (Figure 2.2). The thumb MCP joint is considered as 2 degrees of freedom (DoFs) joint of F/E and Ab/Ad (Kapandji 2007) or 1 degree of freedom (DoF) joint of F/E (Cobos et al. 2010; Lippert 2011). The IP joint, which is the only phalangeal joint, allows only F/E.

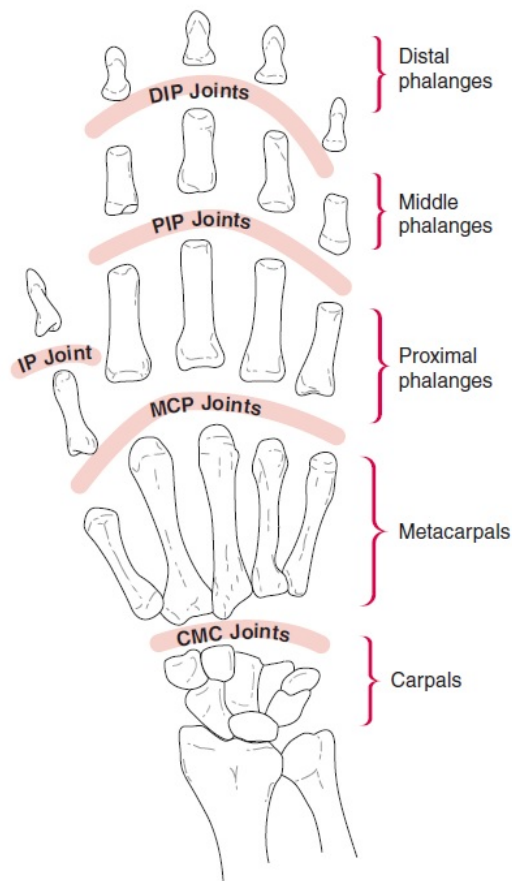


Figure 2.1: Joints and bones of the human hand. Adapted from Lippert (2011). Finger bones are connected with the carpometacarpal (CMC), metacarpophalangeal (MCP), proximal interphalangeal (PIP), and distal interphalangeal (DIP) joints. The thumb has only one interphalangeal (IP) joint.

2.1.2 Skeletal kinematic model

The kinematic complexity of the human hand with its multiple bone and joint structures and with at the very least 20 DoFs makes accurate modelling a challenging task (Bullock et al. 2012). Traditionally, passive range of motion (RoM) of each hand joint is measured using mechanical goniometers or, more recently, potentiometric goniometers, and electrogoniometers (Carpinella et al. 2006). Despite the fact that these methods are inexpensive and require only a minimum subject preparation (Cook et al. 2007), they are

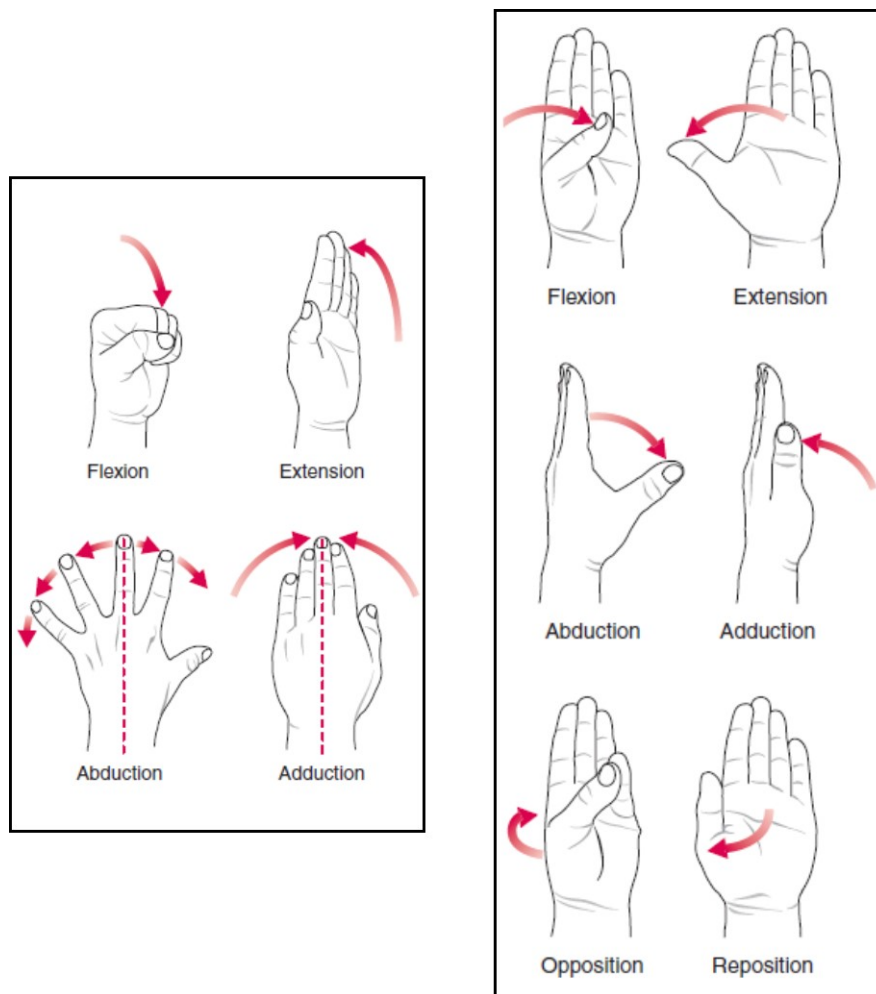


Figure 2.2: The DoFs of the MCP joint of the 2nd – 5th digits (left) and the CMC joint of the thumb (right). Adapted from Lippert (2011).

limited to the examination of static postures only (Cook et al. 2007) and are limited in measuring multiple joints simultaneously (Dipietro et al. 2003). Furthermore, it is quite cumbersome to place the measurement instrument to certain joints (Cook et al. 2007) and the resulting measurement errors depend on the respective examiner and the instrument used (Goodwin et al. 1992). Thus, an alternative method is needed that is able to measure finger angles simultaneously for static tasks and dynamic motions with an adequate degree of precision and sensitivity.

Therefore, optoelectronic motion capture (OMC) methods are regularly used, which employ infrared cameras to track 3-D positions of retro-reflective markers placed at anatomical reference landmarks on the hand and digits (Cook et al. 2007; Nataraj and Li 2013; Nataraj and Li 2015; Parasuraman and Zhen 2009; Veber et al. 2006; Veber and Bajd 2006; Miyata et al. 2004; Metcalf et al. 2008; Cordella et al. 2014). The difficulty in capturing hand kinematics using OMC originates from the relatively large number of DoFs concentrated in a very confined space (Veber et al. 2006). Optoelectronic motion capture methods are capable of marker position measurements with accuracy to sub-millimetre

level (Windolf et al. 2008), provide contact-free measurements, and are less hindering to limb movement (Kofman et al. 2007). Possible error sources are marker positioning, marker occlusions, and soft-tissue artefacts (Nataraj and Li 2013; Metcalf et al. 2008). However, Stillfried et al. (2014) came to the conclusion that soft-tissue artefacts do not have significant effects on the measurement accuracy.

A multitude of kinematic models and evaluation protocols have been proposed to date (Bullock et al. 2012; Carpinella et al. 2006; Cook et al. 2007; Nataraj and Li 2013; Nataraj and Li 2015; Parasuraman and Zhen 2009; Veber et al. 2006; Veber and Bajd 2006; Miyata et al. 2004; Metcalf et al. 2008; Rash et al. 1999; Chiu et al. 1998; Degeorges et al. 2005; Speirs et al. 2001; Braido and Zhang 2004). Certainly, tremendous progress has been made and existing work has unveiled various fundamental properties of the human hand kinematics. Nonetheless, for a number of reasons, a complete and accurate kinematic model with its corresponding identification procedure is still lacking. The most important limitations still present in the state of the art are summarised below.

A Model DoFs

Some models modelled specific joints such as MCP joint only (Speirs et al. 2001), or the long fingers only (Rash et al. 1999; Chiu et al. 1998; Degeorges et al. 2005; Braido and Zhang 2004). Other models modelled a reduced number of finger DoFs (Carpinella et al. 2006; Cook et al. 2007), or only some digits such as the thumb and index finger (Nataraj and Li 2013; Nataraj and Li 2015). Other researchers simplified the five digits into three links, based on the digits' similarities (Parasuraman and Zhen 2009). They modelled the index finger with the middle finger as one link and the ring finger with the pinky finger as a second link, while the thumb represents the third link. More extended models with varying modelling assumptions and accuracy have also been developed (Table 2.1).

B Thumb modelling

The thumb has been modelled with different assumptions regarding its number of DoFs and the definition of axis of rotation. The state-of-the-art thumb models include 3 DoFs (Carpinella et al. 2006), 4 DoFs (Cerveri et al. 2007; Metcalf et al. 2008; Cobos et al. 2010), and 5 DoFs (Miyata et al. 2004; Veber and Bajd 2006; Cordella et al. 2014; Parasuraman and Zhen 2009; Peña-Pitarch et al. 2014) (Table 2.1). Nonetheless, current models are still limited. Despite the fact that few models included thumb kinematics, the thumb was not referenced to its own reference system (Carpinella et al. 2006; Cook et al. 2007). Some models assumed that the axis of rotation of the thumb is perpendicular to the middle finger (Cordella et al. 2014), or is rotated 180° with respect to the wrist reference (Veber and Bajd 2006). However, F/E and Ab/Ad of the thumb metacarpal do not occur about axes that are parallel or perpendicular to the hand plane (Eaton and Littler 1969; Kapandji 2007; Cooney et al. 1981) and thumb movements in the plane of

the hand may occur as a result of combined joint movements (Kuczynski 1974). Thus, a separate coordinate system is required to describe motions at the TM joint as has been recommended by the International Society of Biomechanics (ISB) (Cooney et al. 1981; Wu et al. 2005). Furthermore, a fixed relationship between such a coordinate system and hand dorsal plane reference system was experimentally observed in cadaver specimen using roentgenographic techniques (Cooney et al. 1981).

C Centres of rotation estimation

Most available models rely on surface landmark calculations without taking into consideration the relation between the surface landmarks and the associated joint centres of rotation (CoRs) (Carpinella et al. 2006; Cook et al. 2007; Metcalf et al. 2008; Cordella et al. 2014). Since finger joint markers must be placed on the dorsal surfaces of the fingers, they are not coincident with the CoRs, and thus finger joint CoRs cannot be simply substituted by surface landmark positions. A suitable technique relating finger centre of rotation (CoR) with surface markers is required (Supuk et al. 2004). The identification of the CoRs is important in attaining more accurate description of the underlying bone kinematics, and thus recognising possible kinematic alteration due to pathological conditions (Zhang et al. 2003).

To date, few researchers proposed CoR estimation methods. The most straight forward approach is the direct translation in which the corresponding marker coordinates are translated by half of the joint thickness (Cerveri et al. 2007). However, Cerveri et al. pointed out that the direct translation method is not sufficient and a more accurate identification protocol is required for improving results. Others used optimisation routines (Zhang et al. 2003; Supuk et al. 2004) or a circle intersection method to estimate CoRs (Veber and Bajd 2006; Miyata et al. 2004). However, no forward and inverse functions between surface landmarks and CoRs were proposed in the aforementioned works, and thumb joint CoRs have not yet been identified.

D Palm arc modelling

Typically, the CMC joints of 2nd – 5th digits are ignored in most hand models (Carpinella et al. 2006; Cook et al. 2007; Parasuraman and Zhen 2009; Veber and Bajd 2006; Miyata et al. 2004; Cordella et al. 2014; Cerveri et al. 2007), which results in a completely rigid palm skeletal structure, and further more entirely ignores the palm arc. The palm arc, however, is important in specific tasks such as thumb opposition to pinky finger and grasping tasks. Ignoring the palm arc results in significant errors, in particular in the ring and pinky fingers.

E Experimental set-up

One of the most challenging problems when identifying hand kinematics using motion capture methods is the need for special experimental set-up. The use of rather bulky tripods of markers does not allow the simultaneous recording of all finger movements (Degeorges et al. 2005). Some models need specially designed clusters (e.g. a nail cluster), or special calibration tools (e.g. digit alignment devices) (Nataraj and Li 2013; Shen et al. 2012). Such tools need special design and are obviously affected by subject hand size. These limitations make it difficult to extend the approach to the full hand DoFs or to different subjects with different hand size. In addition, nail clusters for five fingers in a small area might occlude markers or accidentally merge markers. Thus, a practical experimental set-up that can be extended to measure the full hand DoFs of different subjects is required. In this model, a practical marker configuration, which is simple to apply, is proposed. This configuration provides the maximal inter-distance among markers, which make it suitable to be used for the full hand DoFs and minimise the possibility of markers merge.

Table 2.1: State-of-the-art hand kinematic models.

Model	DoFs			Error ^a	CoR Identification
	Digit		Palm arc		
	1 st	2 nd – 5 th			
Miyata et al. (2004)	5 ^b	5	✓	up to 2.98 mm	✓
Veber and Bajd (2006)	5	4	×	n.a.	✓
Cerveri et al. (2007)	4	4	×	up to 3.25 mm	✓ ^c
Carpinella et al. (2006)	3	2	×	n.a.	×
Metcalf et al. (2008)	4	4	✓	n.a.	×
Cordella et al. (2014)	5	4	×	up to 10.67 mm	×
Cobos et al. (2010)	4	4 ^d	✓	n.a	×
Parasuraman and Zhen (2009)	5	4 ^e	×	n.a	×
Peña-Pitarch et al. (2014)	5	4 ^f	✓	n.a	×
Proposed Model	6	4	✓	sub-millimetre	✓

^a The error was calculated as the maximum error of fingertip in Miyata et al. (2004), the maximum of the errors in x -, y -, and z -directions in Cordella et al. (2014), the RMS error of the distance between estimated and measured marker positions in Cerveri et al. (2007), and the Euclidean norm between estimated and measured surface landmarks in the proposed model.

^b Although “8 DoFs” is mentioned explicitly in (Miyata et al. 2004), but 3 of them are the translation from {BH} to {BT}. Thus, it is considered here as a 5 DoF model.

^c CoR estimation includes simple translation.

^d The CMC1 – CMC4 DoFs are considered here in palm arc DoFs.

^e Middle and ring fingers only.

^f The CMC4 and CMC5 DoFs are considered here in palm arc DoFs.

2.1.3 Skeletal dynamic model

The hand has a complex network of muscles and tendons that allow it to generate its movement. The activations of the muscles produce forces and in turn move the joints in a

controlled fashion to accomplish a specific task motion. The relationship between skeletal motion and muscle forces or joint torques occurring during the movements is described by skeletal dynamics. In general, there are two types of dynamic analysis: inverse and forward. The inverse dynamic problem allows the calculation of an estimate of forces and moments driving the motion. In other words, it is an approach that estimates internal forces and joint torques for given kinematic data and external force. On the other hand, the forward dynamic problem simulates and predicts the system's response as a consequence of the applied forces and given initial conditions.

Determining joint torques of the hand is a useful design parameter for humanoid mechanism, rehabilitation robots, and orthotic and prosthetic devices (Serbest et al. 2016). The description of multi-joint dynamic movement has largely focused on the arm and less work has focused on the hand (Gialias and Matsuoka 2006). In most of the studies in the literature, the dynamic analysis of the human hand either focuses on the link torque τ_{Link} only that results from the inertial and gravitational forces (Matsuoka and Afshar 2004; Serbest et al. 2016), or on the passive torque τ_p only that results from the visco-elastic properties of the joints (Agarwal et al. 2013; Kuo and Deshpande 2010; Kuo and Deshpande 2012). However, considering τ_{Link} only would be correct for motions where it is dominant, e.g. shoulder-elbow movements (Hollerbach and Flash 1982; Gribble and Ostry 1999; Dounskaia et al. 2005; Deshpande et al. 2012), and not in human hand movements where τ_p is more dominant (Deshpande et al. 2012). Moreover, determining the role of the passive joint properties in hand control is critical for hand surgery, hand therapy, and mathematical modelling of the hand (Kuo and Deshpande 2010).

The analysis of forces and moments that occur on the joints during movement has been accomplished using external devices (Esteki and Mansour 1996), mathematical models (Fok and Chou 2010; Yun et al. 2002), and simulation tools (e.g. using the MATLAB[®] SimMechanics[™] Toolbox (The MathWorks, Inc., USA)) (Daumas et al. 2005; Jamshidi et al. 2009; Serbest et al. 2015; Serbest et al. 2016; Hu 2015; Hu 2016). SimMechanics[™] is a software in which the geometric and mass attributes of real dimension physical systems are modelled as block diagrams, and dynamic simulations are carried out in accordance with the laws of Newton mechanics (Serbest et al. 2015). While SimMechanics[™] allows kinematic and kinetic analysis of movements without the need to derive the dynamic equations or to use external devices, which can limit the movement and hinder accurate measurement (Serbest et al. 2015; Serbest et al. 2016), it provides τ_{Link} only and lacks τ_p . The torque τ_{Link} is defined as

$$\tau_{\text{Link}} = \mathbf{M}(\mathbf{q})\ddot{\mathbf{q}} + \mathbf{c}(\mathbf{q}, \dot{\mathbf{q}}) + \mathbf{g}(\mathbf{q}), \quad (2.1)$$

where \mathbf{q} , $\dot{\mathbf{q}}$, $\ddot{\mathbf{q}}$ are the angular position, velocity, and acceleration, respectively and are obtained from the kinematic model in Section 2.2.1, $\mathbf{M}(\mathbf{q})$ is the mass matrix, $\mathbf{c}(\mathbf{q}, \dot{\mathbf{q}})$ is the centrifugal and Coriolis vector, and $\mathbf{g}(\mathbf{q})$ is the gravitational torque.

As the passive properties of the finger and wrist musculature influence the hand posture and movement patterns (Esteki and Mansour 1996; Esteki and Mansour 1997; Gialias and Matsuoka 2006), incorporating human-like passive compliance could improve object grasping and manipulation abilities of robotic hands (Kuo and Deshpande 2010). The torque τ_p is defined as

$$\tau_p = \tau_d + \tau_s, \quad (2.2)$$

(Gialias and Matsuoka 2006; Deshpande et al. 2012) where τ_d is the damping passive joint torque, and τ_s is the stiffness passive joint torque, which represents more than 90% of the total passive torque based on two-link planar model dynamics during repetitive hand movements (Gialias and Matsuoka 2006).

In modelling the human hand, each finger is considered as a flexible joint robotic arm. By incorporating the inertial and gravitational torque as well as the visco-elastic torque (Equations 2.1–2.2), the skeleton equation of motion can be rewritten as

$$\tau_{mt} + \tau_{ext} = \tau_{Link} + \tau_p, \quad (2.3a)$$

$$\tau_{mt} + \tau_{ext} = \mathbf{M}(\mathbf{q})\ddot{\mathbf{q}} + \tau_d + \tau_s + \mathbf{c}(\mathbf{q}, \dot{\mathbf{q}}) + \mathbf{g}(\mathbf{q}), \quad (2.3b)$$

(Gialias and Matsuoka 2006; Deshpande et al. 2012) where τ_{ext} is the joint torque due to environmental interaction force, and τ_{mt} the joint torque due to the total musculotendon force.

2.1.4 Contribution

In this chapter, both skeletal kinematic and dynamic models are developed. The focus in the skeletal kinematic model is to propose a highly accurate computational human hand kinematic model, whose correctness is validated via suitable motion capture identification experiments. Specifically, the contributions are:

1. Developing a complete highly accurate 26 DoF hand model, including the four fingers (4 DoFs each), the thumb (4 active DoFs and 2 passive DoFs), and the palm arc (4 DoFs).
2. Developing a thumb kinematic model that is associated to its own frame of reference. Another aim of this specifically is enabling the identification of subject-specific relationships between the thumb reference frame and the hand dorsal reference frame. Based on an in-depth literature review, this is to the authors' knowledge the first study investigating such relationships using motion tracking technique.
3. Underlining the importance of considering passive DoFs on kinematic model accuracy, i.e. additional passive DoFs in the thumb. This forms the first step towards investigating joint elasticity and physical finger-object interaction.

4. Proposing a systematic flexion/extension CoR estimation algorithm, including the forward and inverse kinematics mapping between surface and skeleton kinematics.
5. Proposing a practical identification procedure that can be executed with standard motion tracking techniques.

In the skeletal dynamic model, the focus is to enhance the human hand skeletal dynamic models previously developed in the literature. In particular, the aim is to:

1. Extend the 16 DoF hand model of Serbest et al. (2016) to include the 26 DoFs as proposed in the kinematic model (Section 2.2.1).
2. Include the passive visco-elastic properties of finger joints. The passive visco-elastic properties of the complete hand joints are rarely studied in the literature. Thus, the passive torque model is limited to modelling 6 DoFs of the thumb and F/E DoF of the MCP joint, PIP joint, and DIP joint in the fingers.

2.2 Methods

2.2.1 Skeletal kinematic model

A Modelling assumptions

The human hand is composed of the thumb, four fingers, and the palm. The 2nd - 5th digits have 4 DoFs, i.e. 2 DoFs for MCP joint F/E and Ab/Ad, and 2 DoFs for PIP and DIP joints. The modelling assumptions of the thumb and palm are discussed in the following.

Thumb

The thumb is particularly difficult to model accurately and even harder to simplify (Bullock et al. 2012). Although the motion of the CMC joint of the thumb occurs in the three anatomical planes, the amount of pronation can be determined from the amount of flexion and abduction, thus there remain only two true DoFs (Cooney et al. 1981; Bullock et al. 2012). The thumb MCP joint is modelled with 2 DoFs, i.e. F/E and Ab/Ad (Kapandji 2007). In our pilot experiments, a significant passive DoF (elastic behaviour which might originate from joint capsule elasticity) was noticed in the IP joint due to physical interaction between objects and thumb. Therefore, it may cause inaccuracy in reconstructing fingertip orientation if this passive movement is not considered. Such interactions result in thumb distal phalange pronation, which is modelled by 1 passive DoF (Ab/Ad) in the IP joint. Thus, the proposed thumb model has 6 DoFs (5 actuated and 1 passive). To investigate the importance of the additional passive DoF and the accuracy of the proposed 6 DoFs thumb model in comparison with the state-of-the-art

thumb models, three thumb models are compared and discussed, i.e 4 DoF model, 5 DoF model, and 6 DoF model (Table 2.2).

Table 2.2: The compared thumb models. The passive DoF is indicated by “*”.

Joint	DoF	State-of-the-art models		Proposed model
		4 DoF	5 DoF	6 DoF
CMC	Ab/Ad	✓	✓	✓
	F/E	✓	✓	✓
MCP	Ab/Ad		✓	✓
	F/E	✓	✓	✓
IP	Ab/Ad			✓*
	F/E	✓	✓	✓

Palm arc

The precise positions of the four CMC joints, which contribute to the palm arc system (Levangie and Norikin 2005), are difficult to estimate from motion because of their very small range of movement (Miyata et al. 2004). The 4th – 5th CMC joints rotate with F/E and Ab/Ad and the 2nd – 3rd CMC are static (Peña-Pitarch et al. 2005). Consequently, the formed palm arc is modelled as two palm joints, i.e. the 4th – 5th CMC joints, with 2 DoFs of F/E and Ab/Ad each. In order to underline the importance of considering palm arc on the accuracy of hand kinematics modelling, more specifically on pinky finger pose estimation, two models of the 2nd palm joint are compared and discussed. The compared models have the following characteristics:

- Two DoFs, where the palm arc is modelled,
- A static joint, where the palm arc is not modelled.

In summary, the overall proposed model has 26 DoFs, of which 4 DoFs describe each of 2nd – 5th digits, 4 DoFs describe the palm arc, and 6 DoFs (5 actuated and 1 passive DoF) describe the thumb (Figure 2.3). For the sake of simplification, the bases of the four metacarpal bones have been grouped into a single point.

B Surface and skeletal kinematics model

The human hand is a multibody system where changes in joint configuration result in Cartesian segment movements. With the rigid body assumption about segments, every point on/in a certain segment including the CoRs and surface points moves accordingly. Consequently, joint configurations may be estimated from Cartesian configurations of segment points, which would be straight forward if the CoRs are known. However, since this is generally not the case, one may make use of skin landmarks to estimate joint

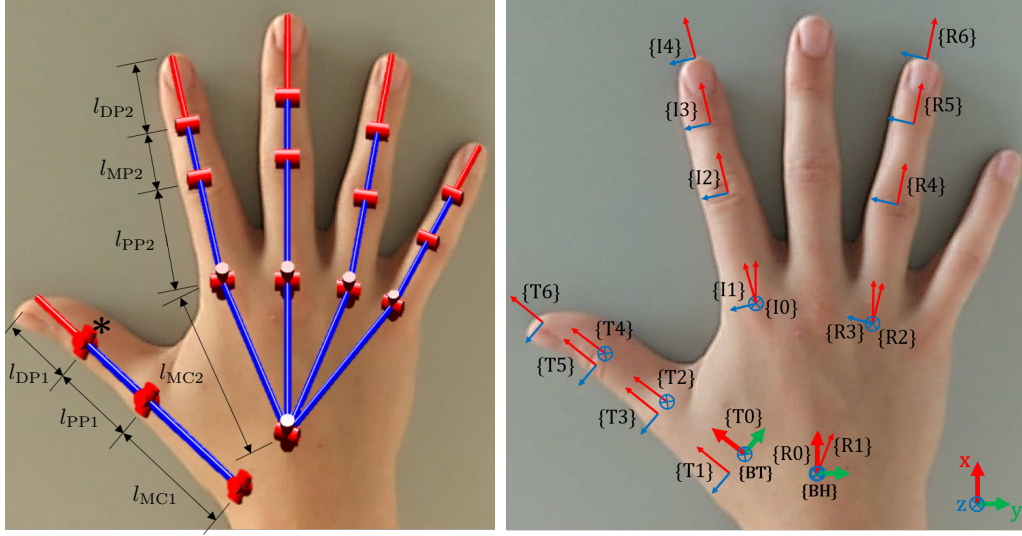


Figure 2.3: The proposed human hand kinematic model with 26 DoFs; 25 actuated DoFs and 1 passive DoF (indicated by “*”). Left: representation of the serial linkages for each digit, which is assumed to be a rigid body segment. Right: the coordinate systems (CS) of the thumb, the index finger (which is similar to the middle finger), the ring finger (which is similar to the pinky finger), and the hand base. The index and middle fingers have 5 CS, while the ring finger, the pinky finger, and the thumb have 7 CS. The alphabet in the CS naming indicates the digit initial.

configurations alternatively. To systematically represent this problem, a novel kinematics model is introduced.

The proposed model connects two representation levels, namely the *skeletal level*, which corresponds to *centres of rotation*, and the *surface level*, which corresponds to *skin landmarks* (Figure 2.4). At the skeletal level, the *skeletal joint configuration vector* $\mathbf{q} := [q_1 \dots q_{26}]^T \in \mathbb{R}^{26}$ and the set of *joint CoR positions* $\{\mathbf{x}_i\}$ are introduced. On the other hand, the *surface joint configuration* (the rotational angles on the *surface level*) $\mathbf{Q} := [Q_1 \dots Q_{26}]^T \in \mathbb{R}^{26}$ and the set of surface Cartesian positions $\{\mathbf{X}_i\}$ are introduced in the surface level. The desired mapping $\{\mathbf{X}_i\} \rightarrow \mathbf{q}$ is divided into composable sub-mappings. These mappings are categorised as follows.

1. Intra-level mappings:
 - Skeletal level, CoR and skeletal joint configuration: $\{\mathbf{x}_i\} \leftrightarrow \mathbf{q}$.
 - Surface level, surface landmark and surface joint configuration: $\{\mathbf{X}_i\} \leftrightarrow \mathbf{Q}$.
2. Inter-level mapping: denoting the transition between surface and skeletal level representations.

Both the Intra-level and inter-level mappings are discussed in the following.

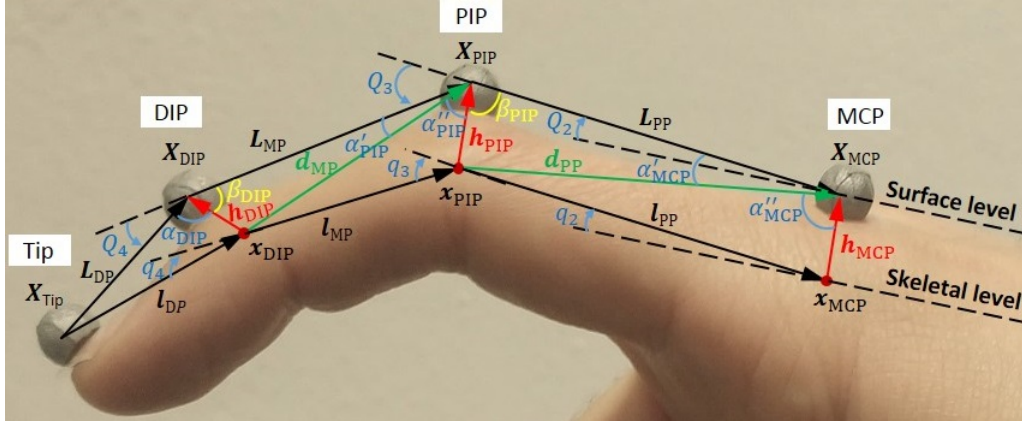


Figure 2.4: Two-dimensional finger schematic diagram. A surface link vector L_{\square} changes its length during F/E whereas that of a skeletal link vector l_{\square} is constant. Bone lengths, $l_{\square} = \|l_{\square}\|$, are calculated from the anthropometric model of Buchholz et al. (1992).

Intra-level mappings: surface kinematics

In the intra-level mappings, surface kinematics describe the relationship between the skin landmark Cartesian positions $\mathbf{X}_i \in \mathbb{R}^3$ and the *surface joint configuration* $\mathbf{Q} \in \mathbb{R}^{26}$ as

$$\mathbf{X} := (\mathbf{X}_1 \ \mathbf{X}_2 \ \cdots \ \mathbf{X}_i \ \cdots \ \mathbf{X}_{25})^{\top}, \quad (2.4a)$$

$$\mathbf{Q} := (Q_1 \ Q_2 \ \cdots \ Q_k \ \cdots \ Q_{26})^{\top}, \quad (2.4b)$$

$$\mathbf{X} = \mathbf{f}(\mathbf{Q}), \quad (2.4c)$$

$$\mathbf{Q} = \mathbf{f}^{-1}(\mathbf{X}), \quad (2.4d)$$

where $\mathbf{f}(\cdot)$ and $\mathbf{f}^{-1}(\cdot)$ denote the forward and inverse surface kinematics, respectively. Two base frames and a frame for each joint DoF are established to find $\mathbf{f}(\cdot)$ and $\mathbf{f}^{-1}(\cdot)$ (Figure 2.3). The base frames are denoted by *Hand Base frame* $\{\text{BH}\}$ and the *Thumb Base frame* $\{\text{BT}\}$. The transformation between the base frames $\{\text{BH}\}$ and $\{\text{BT}\}$ is defined as

$${}^{\text{BH}}\mathbf{T}_{\text{BT}} = \begin{pmatrix} {}^{\text{BH}}\mathbf{R}_{\text{BT}} & {}^{\text{BH}}\mathbf{X}_{\text{BT0}} \\ \mathbf{0}^{\top} & 1 \end{pmatrix}, \quad (2.5)$$

where ${}^{\text{BH}}\mathbf{R}_{\text{BT}} = \mathbf{R}_x \mathbf{R}_y \mathbf{R}_z$ consists of basic rotational matrices about x -, y -, and z -axis, respectively. The vector ${}^{\text{BH}}\mathbf{X}_{\text{BT0}}$ points from the origin of $\{\text{BH}\}$ to the origin of $\{\text{BT}\}$, which is represented by the surface landmark BT0, expressed in $\{\text{BH}\}$.

Joint DoF frames k are determined using the classical Denavit-Hartenberg (D-H) convention (Denavit and Hartenberg 1955), and the transformation between the joint DoF frames. The link and joints parameters in the classical D-H convention are defined as (Reddy 2014):

1. Joint angle θ_k is the angle between the x_{k-1} -axis and the x_k -axis about the z_{k-1} -axis. This angle represents the DoF of the joint.
2. Offset length D_k is the distance from the origin of the $(k-1)$ frame to the intersection of the z_{k-1} -axis with the x_k -axis along the z_{k-1} -axis.
3. Link length a_k is the offset distance from the origin of the frame k to the intersection of the z_{k-1} -axis and the x_k -axis along the x_k -axis.
4. Twist angle α_k is the angle from the z_{k-1} -axis to the z_k -axis about the x_k -axis.

An illustration of the classical D-H convention of the index finger at the surface kinematics level is shown in Figure 2.5, as an example. The index finger has 4 DoFs ($k=1, \dots, 4$) of which 2 DoFs represent the MCP joint DoFs (F/E and Ab/Ad), and 2 DoFs represent the F/E of the PIP and DIP joints. These DoFs are represented by $\theta_1, \dots, \theta_4$. The link length a_k for $k > 1$ is calculated as the distance between two surface landmarks, i.e. L_{PP} , L_{MP} , and L_{DP} . For $k = 0$, the F/E DoF and the Ab/Ad DoF of the MCP joint have the same origin. Thus, the z_0 -axis intersects with the x_1 -axis, which results in $a_1 = 0$. The parameter α_k has only a non zero value at α_1 , where a rotation of $\pi/2$ is required between the Ab/Ad DoF and F/E DoF at the MCP joint. Finally, the offset length D_k is calculated as the translation along the z_k -axis based on the experimental measurements from optoelectronic motion capture data. A summary of the D-H parameters of the surface kinematics is shown in Table 2.3

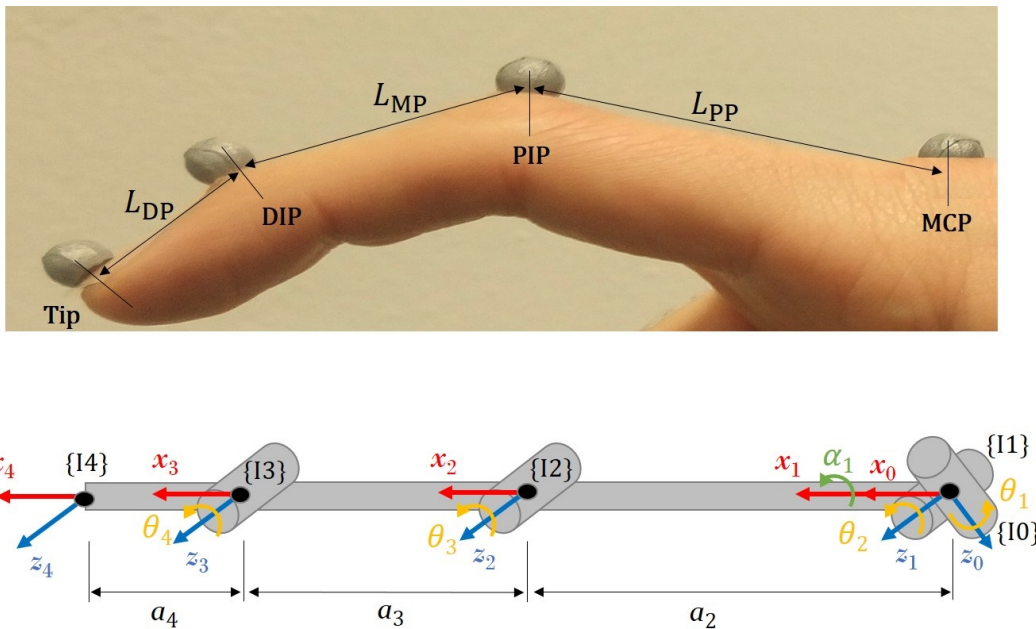


Figure 2.5: Illustration of the classical D-H convention of the index finger at the surface kinematics level. Top: representation of the links and joints. Bottom: description of the classical D-H convention parameters.

The transformation between the joint DoF frames is defined as

$$\begin{pmatrix} {}^{k-1}\mathbf{X}_i \\ 1 \end{pmatrix} = {}^{k-1}\mathbf{T}_k(\mathbf{Q}) \begin{pmatrix} {}^k\mathbf{X}_i \\ 1 \end{pmatrix}, \quad (2.6)$$

(Craig 1989), where ${}^{k-1}\mathbf{X}_i$ and ${}^k\mathbf{X}_i$ are the Cartesian position of the joint landmark i expressed in $\{k-1\}$ and $\{k\}$, respectively, ${}^{k-1}\mathbf{T}_k \in \mathbb{SE}(3)$ are the transformation matrices and formulated as a function of $\mathbf{Q} := (Q_1 \ Q_2 \ \dots \ Q_k)^\top$ using the D-H parameters (Table 2.3) as

$${}^{k-1}\mathbf{T}_k(Q_k) = \begin{bmatrix} \cos Q_k & -\cos \alpha_k \sin Q_k & \sin \alpha_k \sin Q_k & a_k \cos Q_k \\ \sin Q_k & \cos \alpha_k \cos Q_k & -\sin \alpha_k \cos Q_k & a_k \sin Q_k \\ 0 & \sin \alpha_k & \cos \alpha_k & d_k \\ 0 & 0 & 0 & 1 \end{bmatrix}, \quad (2.7)$$

(Reddy 2014).

Equation 2.6 can be solved for \mathbf{Q}_k by using the property ${}^k\mathbf{X}_i = (0 \ 0 \ 0)^\top$, i.e. being the origin of frame k , and by knowing ${}^0\mathbf{X}_i \in \mathbb{R}^3$. For the 2nd and 3rd digits, as an example, the 4 DoFs are calculated as in the following.

For the first two DoFs (Q_1 and Q_2), Equation 2.6 is given as

$$\begin{pmatrix} {}^0\mathbf{X}_{\text{PIP}} \\ 1 \end{pmatrix} = {}^0\mathbf{T}_1(Q_1) {}^1\mathbf{T}_2(Q_2) \begin{pmatrix} {}^2\mathbf{X}_{\text{PIP}} \\ 1 \end{pmatrix}, \quad (2.8)$$

where the transformation matrices ${}^0\mathbf{T}_1(Q_1)$ and ${}^1\mathbf{T}_2(Q_2)$ are defined using Equation 2.7 and the D-H parameters (Table 2.3), ${}^2\mathbf{X}_{\text{PIP}} = (0 \ 0 \ 0)^\top$, and ${}^0\mathbf{X}_{\text{PIP}}$ is known. Thus, Equation 2.8 can be rewritten as

$$\begin{pmatrix} {}^0X_{\text{PIP}} \\ {}^0Y_{\text{PIP}} \\ {}^0Z_{\text{PIP}} \\ 1 \end{pmatrix} = \begin{pmatrix} L_{\text{PP}} \cos Q_1 \cos Q_2 \\ L_{\text{PP}} \cos Q_2 \sin Q_1 \\ L_{\text{PP}} \sin Q_2 \\ 1 \end{pmatrix}, \quad (2.9)$$

where ${}^0X_{\text{PIP}}$, ${}^0Y_{\text{PIP}}$, and ${}^0Z_{\text{PIP}}$ are the x -, y -, and z -components of the PIP landmark position in $\{0\}$, respectively. Consequently, Q_1 and Q_2 can be calculated by

$$Q_1 = \text{atan2}({}^0Y_{\text{PIP}}, {}^0X_{\text{PIP}}), \quad (2.10a)$$

$$Q_2 = \text{atan2}({}^0Z_{\text{PIP}}, \frac{{}^0X_{\text{PIP}}}{\cos Q_1}). \quad (2.10b)$$

The third DoF Q_3 is calculated using Equation 2.6 as

$$\begin{pmatrix} {}^2\mathbf{X}_{\text{DIP}} \\ 1 \end{pmatrix} = {}^2\mathbf{T}_3(Q_3) \begin{pmatrix} {}^3\mathbf{X}_{\text{DIP}} \\ 1 \end{pmatrix}, \quad (2.11a)$$

$$\begin{pmatrix} {}^2X_{\text{DIP}} \\ {}^2Y_{\text{DIP}} \\ {}^2Z_{\text{DIP}} \\ 1 \end{pmatrix} = \begin{pmatrix} L_{\text{MP}} \cos Q_3 \\ L_{\text{MP}} \sin Q_3 \\ 0 \\ 1 \end{pmatrix}, \quad (2.11b)$$

where ${}^2\mathbf{X}_{\text{DIP}}$ is the Cartesian position of the DIP joint landmark expressed in $\{2\}$ using Equation 2.6 and the calculated Q_1 and Q_2 (Equation 2.9), ${}^2X_{\text{DIP}}$, ${}^2Y_{\text{DIP}}$, and ${}^2Z_{\text{DIP}}$ are the x -, y -, and z -components of the DIP landmark position in $\{2\}$, respectively. Using Equation 2.13b, Q_3 is calculated as

$$Q_3 = \text{atan2}({}^2Y_{\text{DIP}}, {}^2X_{\text{DIP}}). \quad (2.12)$$

Analogous to Q_3 , Q_4 is calculated after expressing the Tip landmark position in $\{3\}$ using Equation 2.6 and the calculated $Q_{1\dots3}$ from the previous steps as

$$\begin{pmatrix} {}^3\mathbf{X}_{\text{Tip}} \\ 1 \end{pmatrix} = {}^3\mathbf{T}_4(Q_4) \begin{pmatrix} {}^4\mathbf{X}_{\text{Tip}} \\ 1 \end{pmatrix}, \quad (2.13a)$$

$$\begin{pmatrix} {}^3X_{\text{Tip}} \\ {}^3Y_{\text{Tip}} \\ {}^3Z_{\text{Tip}} \\ 1 \end{pmatrix} = \begin{pmatrix} L_{\text{DP}} \cos Q_4 \\ L_{\text{DP}} \sin Q_4 \\ 0 \\ 1 \end{pmatrix}, \quad (2.13b)$$

$$Q_4 = \text{atan2}({}^3Y_{\text{Tip}}, {}^3X_{\text{Tip}}), \quad (2.13c)$$

where ${}^3X_{\text{Tip}}$ and ${}^3Y_{\text{Tip}}$, and ${}^3Z_{\text{Tip}}$ are the x -, y -, and z -components of the Tip landmark position in $\{3\}$, respectively.

The rotational angles in the other digits are solved similar to the 2nd – 3rd digits (Appendix A).

Intra-level mappings: skeletal kinematics

The skeletal kinematics in the intra-level mapping connects Cartesian positions of joint CoRs $\mathbf{x}_i \in \mathbb{R}^3$ with the *skeletal joint configuration* $\mathbf{q} \in \mathbb{R}^{26}$, i.e.

$$\mathbf{x} := \left(\mathbf{x}_1 \quad \mathbf{x}_2 \quad \cdots \quad \mathbf{x}_i \quad \cdots \quad \mathbf{x}_{15} \right)^{\text{T}}, \quad (2.14a)$$

$$\mathbf{q} := \left(q_1 \quad q_2 \quad \cdots \quad q_k \quad \cdots \quad q_{26} \right)^{\text{T}}, \quad (2.14b)$$

$$\mathbf{x} = \mathbf{g}(\mathbf{q}), \quad (2.14c)$$

$$\mathbf{q} = \mathbf{g}^{-1}(\mathbf{x}), \quad (2.14d)$$

where $\mathbf{g}(\cdot)$ and $\mathbf{g}^{-1}(\cdot)$ are the skeletal forward and inverse kinematics, respectively. These functions are calculated similar to the surface kinematics. A set of reference frames is established using a different D-H parameter set (Table 2.4). The transformation between the joint DoF frames in the skeletal kinematics is defined as

$$\begin{pmatrix} {}^{k-1}\mathbf{x}_j \\ 1 \end{pmatrix} = {}^{k-1}\mathbf{t}_k(\mathbf{q}) \begin{pmatrix} {}^k\mathbf{x}_i \\ 1 \end{pmatrix}, \quad (2.15)$$

(Craig 1989), where the transformation matrices ${}^{k-1}\mathbf{t}_k \in \mathbb{SE}(3)$ are functions of $\mathbf{q}_k := (q_1 \ q_2 \ \cdots \ q_k)^\top$ and calculated using Equation 2.7 along with the D-H parameters (Table 2.4), ${}^{k-1}\mathbf{x}_i$ and ${}^k\mathbf{x}_i$ are the Cartesian positions of the CoR of the joint i expressed in $\{k-1\}$ and $\{k\}$, respectively. By using the property ${}^k\mathbf{x}_i = (0 \ 0 \ 0)^\top$ and knowing ${}^B\mathbf{x}_i \in \mathbb{R}^3$, Equation 2.15 can be solved for \mathbf{q} analogous to Equations 2.10-2.13.

Inter-level mappings

In the previous section, the intra-level mappings, i.e. the surface kinematics and the skeletal kinematics, were introduced. The mapping between these two levels is done by the inter-level mapping. The surface and skeletal level positions are related to each other by a vector \mathbf{h}_i (Figure 2.4), as

$$\mathbf{X}_i = \mathbf{x}_i + \mathbf{h}_i, \quad (2.16)$$

where \mathbf{h}_i is defined as the vector pointing from a given joint CoR to the corresponding skin landmark with constant length and changing orientation (Zhang et al. 2003). It can be estimated geometrically as explained in the next section.

C Estimation of \mathbf{h}_i

As the F/E motions of the three finger joints occur in a single plane, the considered problem is expressed as 2-D to minimise the number of unknowns (Zhang et al. 2003) (Figure 2.4). In the 2nd – 5th digits, the 2-D frame should be chosen such that F/E motions occur without being affected by the MCP Ab/Ad DoF. In Supuk et al. (2004) the F/E plane, which represents the 2-D plane, is defined based on wrist-hand reference frame without considering the MCP Ab/Ad DoF. The best frame is the MCP F/E frame, e.g. $\{I1\}$ in the 2nd digit (Figure 2.3), which moves with Ab/Ad motion accordingly.

Compared to the 2nd – 5th digits, the 1st digit has an additional Ab/Ad DoF in the second and third joints. This makes the F/E frame move with Ab/Ad motion accordingly. Thus, the F/E of the three joints of the 1st digit is not happening in a single plane as in the other digits. Thus, calculating CoR cannot be performed by expressing positions in $\{T1\}$, as the F/E of CMC resides in a different plane than in the MCP and IP joints. To overcome this issue, the CoR of CMC joint is calculated in frame $\{T1\}$, while the CoRs of MCP and IP joints are obtained in frames $\{T3\}$ and $\{T5\}$, respectively (Figure 2.3).

Table 2.3: D-H parameters of surface kinematics. The offset length D_k is calculated as the translation along the z_k -axis using the optoelectronic motion capture data.

1st digit					
Frame k	θ_k	D_k	a_k	α_k	DoF
1	Q_1	0	0	$\pi/2$	CMC Ab/Ad
2	Q_2	0	L_{MC}	$-\pi/2$	CMC F/E
3	Q_3	0	0	$\pi/2$	MCP Ab/Ad
4	Q_4	0	L_{PP}	$-\pi/2$	MCP F/E
5	Q_5	0	0	$\pi/2$	IP Ab/Ad
6	Q_6	0	L_{DP}	0	IP F/E
2nd – 3rd digits					
Frame k	θ_k	D_k	a_k	α_k	DoF
1	Q_1	0	0	$\pi/2$	MCP Ab/Ad
2	Q_2	0	L_{PP}	0	MCP F/E
3	Q_3	D_3	L_{MP}	0	PIP F/E
4	Q_4	D_4	L_{DP}	0	DIP F/E
4th – 5th digits					
Frame k	θ_k	D_k	a_k	α_k	DoF
1	Q_1	0	0	$\pi/2$	CMC Ab/Ad
2	Q_2	0	L_{MC}	$-\pi/2$	CMC F/E
3	Q_3	0	0	$\pi/2$	MCP Ab/Ad
4	Q_4	0	L_{PP}	0	MCP F/E
5	Q_5	D_5	L_{MP}	0	PIP F/E
6	Q_6	D_6	L_{DP}	0	DIP F/E

Table 2.4: D-H parameters of skeletal kinematics. The offset length d_k is fitted using polynomial regression as a function of q_k (Figure 2.6).

1st digit					
Frame k	θ_k	d_k	a_k	α_k	DoF
1	q_1	0	0	$\pi/2$	CMC Ab/Ad
2	q_2	0	l_{MC}	$-\pi/2$	CMC F/E
3	q_3	0	0	$\pi/2$	MCP Ab/Ad
4	q_4	0	l_{PP}	$-\pi/2$	MCP F/E
5	q_5	0	0	$\pi/2$	IP P/S
6	q_6	0	l_{DP}	0	IP F/E
2nd – 3rd digits					
Frame k	θ_k	d_k	a_k	α_k	DoF
1	q_1	0	0	$\pi/2$	MCP Ab/Ad
2	q_2	0	l_{PP}	0	MCP F/E
3	q_3	d_3	l_{MP}	0	PIP F/E
4	q_4	d_4	l_{DP}	0	DIP F/E
4th – 5th digits					
Frame k	θ_k	d_k	a_k	α_k	DoF
1	q_1	0	0	$\pi/2$	CMC Ab/Ad
2	q_2	0	l_{MC}	$-\pi/2$	CMC F/E
3	q_3	0	0	$\pi/2$	MCP Ab/Ad
4	q_4	0	l_{PP}	0	MCP F/E
5	q_5	d_5	l_{MP}	0	PIP F/E
6	q_6	d_6	l_{DP}	0	DIP F/E

In the 2-D spaces, the Law of Cosines is used to estimate \mathbf{h}_i . The vector \mathbf{h}_i in the thumb joints is estimated analogously to the other fingers with considering the difference in defining the joint F/E plane. Figure 2.3 shows the fingers' 2-D F/E plane and the parameters definition to calculate \mathbf{h}_i . The vector \mathbf{h}_i for different joints of the 2nd – 5th digits is calculated as follows.

DIP joint

The vector \mathbf{h}_{DIP} is defined as

$$\mathbf{h}_{\text{DIP}} = \|\mathbf{h}_{\text{DIP}}\| \mathbf{e}_{h_{\text{DIP}}}, \quad (2.17)$$

where $\|\mathbf{h}_{\text{DIP}}\|$ is the DIP joint thickness and can be measured, and the unit vector $\mathbf{e}_{h_{\text{DIP}}}$ is obtained as in Supuk et al. (2004) from

$$\mathbf{L}_{\text{DP}} \cdot \mathbf{e}_{h_{\text{DIP}}} = \|\mathbf{L}_{\text{DP}}\| \|\mathbf{e}_{h_{\text{DIP}}}\| \cos \alpha_{\text{DIP}}, \quad (2.18a)$$

$$-\mathbf{L}_{\text{MP}} \cdot \mathbf{e}_{h_{\text{DIP}}} = \|\mathbf{L}_{\text{MP}}\| \|\mathbf{e}_{h_{\text{DIP}}}\| \cos \beta_{\text{DIP}}, \quad (2.18b)$$

as

$$\mathbf{e}_{h_{\text{DIP}}} = \begin{pmatrix} \mathbf{L}_{\text{DP}}^{\text{T}} \\ -\mathbf{L}_{\text{MP}}^{\text{T}} \end{pmatrix}^{-1} \begin{pmatrix} \|\mathbf{L}_{\text{DP}}\| \cos \alpha_{\text{DIP}} \\ \|\mathbf{L}_{\text{MP}}\| \cos \beta_{\text{DIP}} \end{pmatrix}, \quad (2.19)$$

where \mathbf{L}_{DP} and \mathbf{L}_{MP} are projected on the 2-D plane and should be linearly independent (i.e. $Q_4 \neq 0$ so that the matrix is invertible), and α_{DIP} is obtained from the Law of Cosines as

$$\alpha_{\text{DIP}} = \arccos \frac{\|\mathbf{L}_{\text{DP}}\|^2 - \|\mathbf{L}_{\text{MP}}\|^2 - \|\mathbf{h}_{\text{DIP}}\|^2}{-2\|\mathbf{L}_{\text{DP}}\| \|\mathbf{h}_{\text{DIP}}\|}, \quad (2.20)$$

and β_{DIP} is calculated from

$$\beta_{\text{DIP}} = \pi - (Q_4 + \alpha_{\text{DIP}}). \quad (2.21)$$

PIP joint

Analogous to Equation 2.17, the vector \mathbf{h}_{PIP} is defined as

$$\mathbf{h}_{\text{PIP}} = \|\mathbf{h}_{\text{PIP}}\| \mathbf{e}_{h_{\text{PIP}}}, \quad (2.22)$$

where $\|\mathbf{h}_{\text{PIP}}\|$ is the PIP joint thickness and can be measured, and the unit vector $\mathbf{e}_{h_{\text{PIP}}}$ is found from solving

$$\mathbf{e}_{h_{\text{PIP}}} = \begin{pmatrix} \mathbf{L}_{\text{MP}}^{\text{T}} \\ -\mathbf{L}_{\text{PP}}^{\text{T}} \end{pmatrix}^{-1} \begin{pmatrix} \|\mathbf{L}_{\text{MP}}\| \cos \alpha_{\text{PIP}} \\ \|\mathbf{L}_{\text{PP}}\| \cos \beta_{\text{PIP}} \end{pmatrix}. \quad (2.23)$$

where \mathbf{L}_{MP} and \mathbf{L}_{PP} are projected on the 2-D plane and should be linearly independent (i.e. $Q_3 \neq 0$ so that the matrix is invertible). The angle α_{PIP} is defined as

$$\begin{aligned}\alpha_{PIP} &= \alpha'_{PIP} + \alpha''_{PIP} \\ \alpha'_{PIP} &= \arccos \frac{\|\mathbf{h}_{DIP}\|^2 - \|\mathbf{L}_{MP}\|^2 - \|\mathbf{d}_{MP}\|^2}{-2\|\mathbf{L}_{MP}\|\|\mathbf{d}_{MP}\|} \\ \alpha''_{PIP} &= \arccos \frac{\|\mathbf{L}_{MP}\|^2 - \|\mathbf{h}_{PIP}\|^2 - \|\mathbf{d}_{MP}\|^2}{-2\|\mathbf{h}_{PIP}\|\|\mathbf{d}_{MP}\|}\end{aligned}\quad (2.24)$$

and β_{PIP} is

$$\beta_{PIP} = \pi - (Q_3 + \alpha_{PIP}). \quad (2.25)$$

MCP joint

The vector \mathbf{h}_{MCP} is defined analogous to Equation 2.17, where the unit vector $\mathbf{e}_{h_{MCP}}$ is calculated as

$$\mathbf{e}_{h_{MCP}} = \begin{pmatrix} \mathbf{L}_{PP}^T \\ \mathbf{d}_{PP}^T \end{pmatrix}^{-1} \begin{pmatrix} \|\mathbf{L}_{PP}\| \cos(\alpha'_{MCP} + \alpha''_{MCP}) \\ \|\mathbf{d}_{PP}\| \cos \alpha''_{MCP} \end{pmatrix}, \quad (2.26)$$

where \mathbf{L}_{PP} is projected on the 2-D space and α'_{MCP} and α''_{MCP} are calculated via the Law of Cosines similar to Equation 2.24.

D Model identification and validation

The ideal model validation method would be the simultaneous measurement of motion capture data synchronised with online high frequency imaging. As this is technically not feasible, the proposed model is evaluated according to the consistency scheme shown in Figure 2.6. The model self-consistency and accuracy are evaluated by quantifying the difference $\{\mathbf{E}_i\}$ between the measured marker positions $\{\mathbf{X}_i\}$ using an optoelectronic motion capture system and the estimated ones $\{\hat{\mathbf{X}}_i\}$. The identification and validation procedure consists of two main calculation paths: the inverse path, which is indicated as 1, and the forward path, which is indicated as 2 (Figure 2.6). In the inverse calculation path, only model parameters, i.e. $\{\|\mathbf{h}_i\|\}$ and HL , and measurements $\{\mathbf{X}_i\}$ are required as an input to estimate the skeletal joint configuration $\{\mathbf{q}\}$. In the forward calculation path, $\{\mathbf{q}\}$ and the fitted model relation $\{d_k(q_k)\}$ are required to estimate $\{\hat{\mathbf{x}}_i\}$. Then, $\{\hat{\mathbf{X}}_i\}$ is calculated as

$$\hat{\mathbf{X}}_i = \hat{\mathbf{x}}_i + \mathbf{h}_i, \quad (2.27)$$

and $\{\mathbf{E}_i\}$ is calculated as

$$\mathbf{E}_i = \|\mathbf{X}_i - \hat{\mathbf{X}}_i\|. \quad (2.28)$$

Based on our experiments, it was noticed that the D-H parameters D_k and d_k are changing over time ($D_k \neq 0$ and $d_k \neq 0$) while performing tasks, which consequently affects the accuracy of the kinematic model. This might be related to the nature of the fingers, which are actually slightly curved rather than straight (Cordella et al. 2014), joint capsule elasticity, and the physical finger-object interaction. To overcome this issue, in the proposed model D_k is calculated based on the experimental measurements from motion tracking data, while d_k is fitted as a function of q_k (in our case polynomial regression) (Figure 2.6). This improves the model accuracy to a sub-millimetre error in most cases. Only in one case, an error of nearly 2 mm was observed due to the d_k - q_k fitting used. This, however, might be solved using other fitting functions. In addition, the variance of d_k during tasks should be further investigated with respect to joint DoFs, joint capsule elasticity, and physical finger-object interaction in the future.

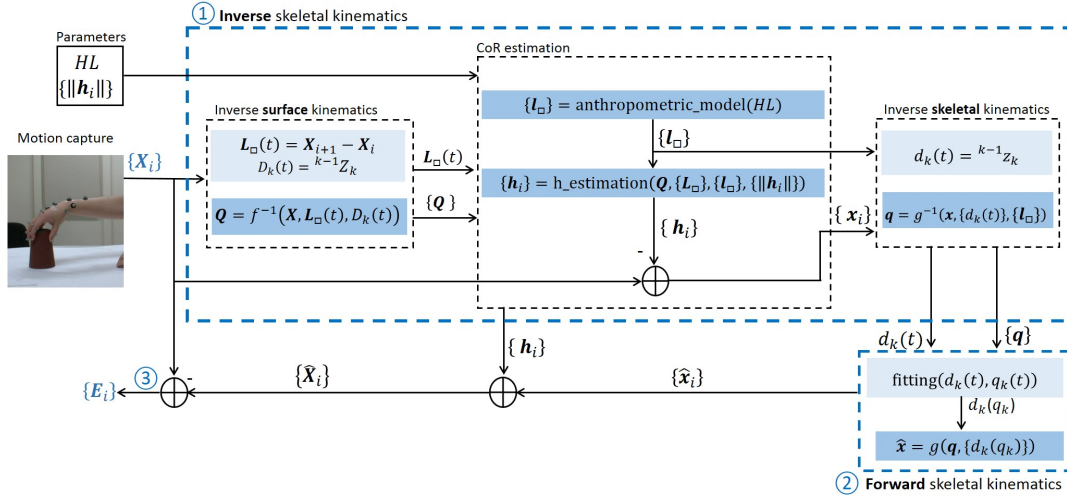


Figure 2.6: Block diagram of model identification and validation. The symbols are defined in the symbol list. Bone lengths $\{L_{\square}\}$ are calculated from the anthropometric model of Buchholz et al. (1992). Both the hand length HL and joint thickness $\|h_i\|$ are measured for each subject.

Algorithmic identification procedure

Two algorithmic identifications are used: identification of the rotational matrices (${}^W R_{BH}$), and ${}^{BH} R_{BT}$ and hand kinematics. In the identification of ${}^W R_{BH}$ and ${}^{BH} R_{BT}$, a floating base coordinate system is established in which \mathbf{X}_i are expressed. In the proposed model, two base coordinate systems, defined as $\{BH\}$ and $\{BT\}$, are used (Figure 2.7). The identification of $\{BH\}$ is performed every time step, while $\{BT\}$ is established by defining a rotational matrix between $\{BH\}$ and $\{BT\}$ in the reference posture task (Algorithm 2.1). After defining the floating base coordinate systems, the overall identification of hand kinematics procedure that estimates the joint angles \mathbf{q} from measured marker positions \mathbf{X}_i is performed (Algorithm 2.2).

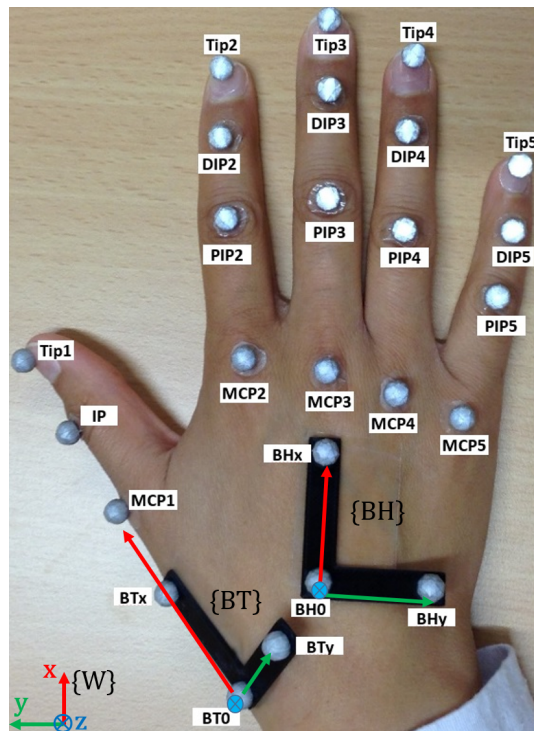


Figure 2.7: Marker placement and labelling. Markers were labelled to indicate the joint names and the digit numbers (1: thumb, 2: index, ..., 5: pinky). A reference marker cluster (BHx-BH0-BHy) was attached to the dorsal side of the hand to establish the hand floating base coordinate system $\{BH\}$. Another marker cluster (BTx-BT0-BTy) was attached to the base of the first metacarpal bone to establish the thumb reference coordinate system $\{BT\}$.

Experimental set-up

Nine neurologically normal subjects (two females and seven males, aged = 29.11 ± 4.20 years, right-handed, $HL = 183.83 \pm 8.35$ mm) volunteered for the study. All participants provided written consent prior to their participation. The test procedures were conducted according to the guidelines of the *Declaration of Helsinki* and approved by the ethics committee of *Leibniz Universität Hannover, Germany*.

An optoelectronic motion capture system (©Vicon Motion Systems Ltd., UK with its associated software Nexus 2.0) with eight infrared video cameras were used at a sampling rate of 500 Hz. The working volume ($80 \times 80 \times 100$ cm³) was calibrated using an active L-wand based on the manufacturer instructions to provide a global measurement error of ≤ 0.09 mm and in most of the cases ≤ 0.06 mm.

Twenty-five reflective spherical markers, with a diameter of 6 mm were attached to the right hand on specific bony landmarks (Figure 2.7). In the 2nd – 5th digit markers were attached to the heads of the metacarpals, the heads of the proximal phalanges, the heads of the middle phalanges, and the fingertips. For the thumb, four markers were attached to the head and base of the metacarpal, the head of the proximal phalange, and the tip.

Algorithm 2.1 Identification of ${}^W R_{BH}$ and ${}^{BH} R_{BT}$

-
- 1: **Input:** $\{{}^W X_i\}$ ▷ In Task S1 (Figure 2.9)
 - 2: **Output:** ${}^W R_{BH}, {}^{BH} R_{BT}$ ▷ Equation 2.5
 - 3: **Procedure:**
 - 4: $e_x := \frac{{}^W X_{BHx} - {}^W X_{BH0}}{\|{}^W X_{BHx} - {}^W X_{BH0}\|}$; ▷ establish $\{BH\}$, x -axis
 - 5: $e_y := \frac{{}^W X_{BHy} - {}^W X_{BH0}}{\|{}^W X_{BHy} - {}^W X_{BH0}\|}$; ▷ y -axis
 - 6: $e_z := e_x \times e_y$; ▷ z -axis (right-hand rule)
 - 7: ${}^W R_{BH} := \begin{pmatrix} e_x & e_y & e_z \end{pmatrix}$; ▷ Establish ${}^W R_{BH}$
 - 8: $\begin{pmatrix} {}^{BH} X_i \\ 1 \end{pmatrix} := \begin{pmatrix} {}^W R_{BH} & {}^W X_{BH0} \\ \mathbf{0}^T & 1 \end{pmatrix}^{-1} \begin{pmatrix} {}^W X_i \\ 1 \end{pmatrix}$; ▷ Express positions in $\{BH\}$
 - 9: $e_x := \frac{{}^{BH} X_{BTx} - {}^{BH} X_{BT0}}{\|{}^{BH} X_{BTx} - {}^{BH} X_{BT0}\|}$; ▷ Establish $\{BT\}$, x -axis
 - 10: $e_y := \frac{{}^{BH} X_{BTy} - {}^{BH} X_{BT0}}{\|{}^{BH} X_{BTy} - {}^{BH} X_{BT0}\|}$; ▷ y -axis
 - 11: $e_z := e_x \times e_y$; ▷ z -axis (right-hand rule)
 - 12: ${}^{BH} R_{BT} := \begin{pmatrix} e_x & e_y & e_z \end{pmatrix}$; ▷ Establish ${}^{BH} R_{BT}$
-

Algorithm 2.2 Identification of hand kinematics

-
- 1: **Inputs:** $\{{}^{BH} X_i\}, \{\|h_i\|\}, HL, {}^{BH} R_{BT}$ ▷ HL : hand length
 - 2: **Output:** q
 - 3: **Procedure:**
 - 4: $L_{PP} := {}^{BH} X_{MCP} - {}^{BH} X_{PIP}$;
 - 5: $L_{MP} := {}^{BH} X_{PIP} - {}^{BH} X_{DIP}$;
 - 6: $L_{DP} := {}^{BH} X_{DIP} - {}^{BH} X_{Tip}$;
 - 7: $Q := f^{-1}(X)$; ▷ Surface kinematics (Equation 2.4)
 - 8: $\{l_\square\} := \text{anthropometric_model}(HL)$; ▷ Anthropometric model (Buchholz et al. 1992)
 - 9: $\{h_i\} := h_estimation(Q, \{L_\square\}, \{l_\square\}, \{\|h_i\|\})$; ▷ Estimation of h_i (Section C)
 - 10: $x_i := X_i - h_i$;
 - 11: $q := g^{-1}(x)$; ▷ Skeletal kinematics (Equation 2.14)
-

This marker configuration is recommended by Metcalf et al. (2008) as it has proven to be intuitive, simple to apply in a clinical research setting, and does not interfere with finger movements. In addition, it provides maximal inter-distance among markers where improved results can be obtained (Veber and Bajd 2006).

A three-marker reference system (BHx-BH0-BHy) was used to establish the hand floating base coordinate system $\{BH\}$ (Figure 2.7). This cluster was aligned with the 3rd

metacarpal, which has special significance due to its use in the definition of the global wrist motion (Wu et al. 2005). Another reference cluster (BT_x-BT₀-BT_y) was fixed on the base of the first metacarpal bone to identify the thumb reference coordinate system {BT}. The plastic L-frames were used to have a standard reference for all subjects. However, hand reference cluster markers can be attached directly to the skin.

Subjects were seated upright on a chair behind a table with the x -axis of {BH} in reference posture parallel to the anterior axis of the subject (Figure 2.8). The chair height and position were adjusted to provide the best camera view and focus. In each trial, marker coordinates were acquired for a duration of 6 s during two static tasks (relaxed reference posture and thumb-pinky opposition), and three dynamic tasks (i.e. grasp/release of cylinders) (Figure 2.9).



Figure 2.8: Experimental subject posture.

2.2.2 Skeletal dynamic model

The dynamics of the human hand is modelled using Equation 2.3 with assuming τ_{ext} to be zero, i.e. $\tau_{\text{ext}} = \mathbf{0}$, thus Equation 2.3 can be rewritten as

$$\tau_{\text{mt}} = \tau_{\text{Link}} + \tau_{\text{p}}, \quad (2.29\text{a})$$

$$\tau_{\text{mt}} = \mathbf{M}(\mathbf{q})\ddot{\mathbf{q}} + \tau_{\text{d}} + \tau_{\text{s}} + \mathbf{c}(\mathbf{q}, \dot{\mathbf{q}}) + \mathbf{g}(\mathbf{q}), \quad (2.29\text{b})$$

The left-hand side of Equation 2.29 is modelled in the Musculotendon dynamic model (Section 3.2.2) while the components of the right-hand side are modelled in the following.

A Link torque

The link torque τ_{Link} , represented in Equation 2.1, was implemented using the MATLAB[®] SimMechanics[™] Toolbox. SimMechanics[™] has been widely used for numerical dynamic

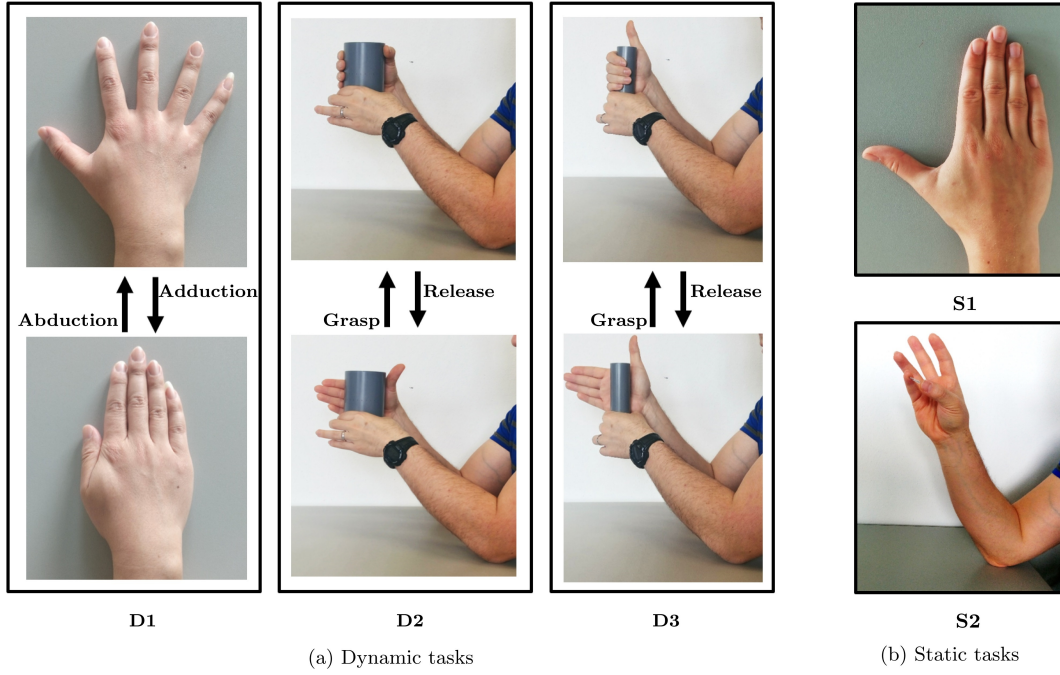


Figure 2.9: Experimental static and dynamic tasks. The static tasks are: S1: relaxed reference posture with all joints extended, and S2: grasping a small paper clip by thumb and pinky digits (thumb-pinky opposition). The dynamic tasks are: D1: MCP joints Ab/Ad, D2: grasp/release a cylinder with diameter of 80 mm, and D3: grasp/release a cylinder with diameter of 40 mm.

analysis of human motion (Daumas et al. 2005; Jamshidi et al. 2009; Serbest et al. 2015; Serbest et al. 2016; Hu 2015; Hu 2016). In order to implement the hand model in SimMechanicsTM, a kinematic model as well as anthropometric properties should be defined. The kinematic structure of the hand is described as an open chain link-segment model. It consists of 19 segments and 26 revolute joints (Figure 2.3). In order to determine the anthropometric properties, the hand finger bones are assumed to be rigid cylinders with uniform mass distribution moving in a fixed plane. The phalanx centre of mass is assumed to be on the midpoint of the phalanx. Consequently the phalanx body mass m_{\square} and inertia tensor I_{\square} for each phalanx are calculated as

$$m_{\square} = \rho V_{\square}, \quad (2.30a)$$

$$I_{\square} = \begin{pmatrix} \frac{1}{2}m_{\square}r_{\square}^2 & 0 & 0 \\ 0 & \frac{1}{12}m_{\square}(3r_{\square}^2 + l_{\square}^2) & 0 \\ 0 & 0 & \frac{1}{12}m_{\square}(3r_{\square}^2 + l_{\square}^2) \end{pmatrix}, \quad (2.30b)$$

where ρ is the human body density 1.1 g/cm^3 (Esteki and Mansour 1997; Sancho-Bru et al. 2001; Kamper et al. 2002; Qiu and Kamper 2014), V_{\square} is the volume of the phalanx body and considered as the volume of a cylinder, r_{\square} and l_{\square} are the phalanx body radius and length, respectively. After defining the required anthropometric properties, i.e. r_{\square} , l_{\square} ,

and m_{\square} , for each phalanx (Table 2.5), SimMechanicsTM computes the joint link torque for a given motion input.

B Passive torque

Finger passive properties, defined by joint stiffness and damping, are critical in all human movements since these properties allow us to interact safely, reliably, and efficiently with the world around us (Deshpande et al. 2013). Despite this being a critical issue in hand movements during grasping and manipulation (Gialias and Matsuoka 2006; Deshpande et al. 2012; Deshpande et al. 2013), very few robotic hands imitate human-like passive properties (Pylatiuk et al. 2004; Lotti et al. 2005; Deshpande et al. 2013). The passive torque τ_p is modelled as a summation of the damping torque τ_d and the stiffness torque τ_s (Equation 2.2).

Table 2.5: The anthropometric properties of the human hand.

Digit	Phalanx	r_{\square} [mm]	l_{\square} [mm]	m_{\square} [g]	I_{\square} [g.cm ²]		
					$I_{\square,x}$	$I_{\square,y}$	$I_{\square,z}$
Thumb	Metacarpal (MC)	10.3	52.4	18.5	40.7218	40.72180	9.8161
	Proximal (PP)	10.3	35.28	12.5	10.6234	10.6234	6.6115
	Distal (DP)	10.3	28.44	10.0	9.4372	9.4372	5.3297
Index	Metacarpal (MC)	9.9	64.6	20.9	70.7716	70.7716	10.0128
	Proximal (PP)	9.9	44.1	14.2	20.6548	20.6548	6.9121
	Medial (MP)	9.1	25.7	7.0	5.3136	5.3136	2.8749
	Distal (DP)	8.2	20.5	4.6	2.3683	2.3683	1.5402
Middle	Metacarpal (MC)	10.0	64.4	21.4	70.9481	70.9481	10.0723
	Proximal (PP)	10.0	47.9	15.9	30.4447	30.4447	7.9722
	Medial (MP)	9.1	30.6	8.5	8.3869	8.3869	3.5325
	Distal (DP)	8.3	25.8	5.8	4.2387	4.2387	1.9900
Ring	Metacarpal (MC)	9.4	56.7	16.5	40.7734	40.7734	7.2102
	Proximal (PP)	9.4	43.9	12.8	20.3348	20.3348	5.5890
	Medial (MP)	8.5	29.7	7.2	6.5896	6.5896	2.6119
	Distal (DP)	7.7	24.3	4.8	3.0592	3.0592	1.4200
Pinky	Metacarpal (MC)	8.3	49.2	11.2	20.4420	20.4420	3.7965
	Proximal (PP)	8.3	36.7	8.3	10.0768	10.0768	2.8323
	Medial (MP)	7.6	21.1	4.1	2.0997	2.0997	1.1853
	Distal (DP)	7.0	18.7	3.1	1.2695	1.2695	0.7491

Damping torque

The damping torque τ_d is modelled to be dependent on the joint velocity \dot{q} only as

$$\tau_d = \mathbf{K}\dot{q}, \quad (2.31)$$

(Gialias and Matsuoka 2006; Deshpande et al. 2012; Agarwal et al. 2013), where \mathbf{K} is the joint damping coefficient vector (considered to be constant), and can be chosen based on previous studies (Barnett and Cobbold 1968; Hajian 1997; Hajian and Howe 1997; Kamper et al. 2002; Jindrich et al. 2004; Gialias and Matsuoka 2006; Xu et al. 2011; Deshpande et al. 2012; Vignais and Marin 2014; Agarwal et al. 2013). The damping coefficients that were used in the proposed model are shown in Table 2.6.

Table 2.6: Joint damping coefficients.

Digit	Joint j	Damping ^a
		K_j [N.mm.s/°]
1 st	CMC Ab/Ad	0.262 ^b
	CMC F/E	0.262
	MCP Ab/Ad	0.175 ^b
	MCP F/E	0.175
	IP Ab/Ad	0.087 ^b
	IP F/E	0.087
2 nd – 3 rd	MCP Ab/Ad	1.27 ^b
	MCP F/E	1.27
	PIP F/E	0.419
	DIP F/E	0.237
4 th – 5 th	CMC Ab/Ad	0.262 ^c
	CMC F/E	0.262 ^c
	MCP Ab/Ad	1.27 ^b
	MCP F/E	1.27
	PIP F/E	0.419
	DIP F/E	0.237

^a Vignais and Marin (2014).

^b The damping coefficient in Ab/Ad DoF is assumed to be identical to that in F/E DoF (Tkany 2018).

^c The damping coefficients in CMC4 and CMC5 are assumed to be identical to that in CMC1 (Tkany 2018).

Table 2.7: State-of-the-art hand stiffness models.

Model	Modelling function	Joint				
		Thumb	Index	Middle	Ring	Pinky
Kamper et al. (2002)	Polynomial		3 DoFs			
Jindrich et al. (2004)	Linear		3 DoFs			
Galias and Matsuoka (2006)	Exponential functions		1 DoF			
Wu et al. (2009a)	Linear	5 DoFs				
Kuo and Deshpande (2010)	Double exponential		1 DoF			
Kuo and Deshpande (2012)	Double exponential		1 DoF			
Deshpande et al. (2012)	Double exponential		1 DoF			
Deshpande et al. (2013)	Double exponential		1 DoF			
Agarwal et al. (2013)	Double exponential		3 DoFs			
Vignais and Marin (2014)	Linear	5 DoFs	4 DoFs	4 DoFs	4 DoFs	4 DoFs
Proposed model	Double exponential and linear	6 DoFs	3 DoFs	3 DoFs	3 DoFs	3 DoFs

Stiffness torque

Previously developed stiffness torque models are based on three modelling functions, i.e. linear, polynomial, and double exponential (Table 2.7). The double exponential function model is preferred in the literature and used in the proposed model as it: 1) provides good fits to many types of passive moment-angle or force-length data (Esteki and Mansour 1996; Keir et al. 1996; Knutson et al. 2000), and 2) results in a natural finger movement in simulation (Tkany 2018). The passive stiffness properties of the complete hand joints are rarely studied in the literature, i.e. most of the studies focus on the index finger F/E DoFs and more specifically on the MCP F/E DoF (Table 2.7). To the best of our knowledge, stiffness coefficients for some joints, e.g. CMC4 and CMC5, have not been reported in experimental studies. Therefore, the proposed stiffness model has a few limitations/assumptions including:

1. The proposed model is limited to model F/E of the three joints of the index finger and the 6 DoFs of the thumb.
2. The model of the middle, ring, and pinky fingers is assumed to be the same as the index finger.

The model of the index finger and the thumb are explained in the following.

The passive stiffness torque at the index MCP F/E joint increases exponentially as the joint angle extends or flexes (Deshpande et al. 2013) and shows a double exponential response based on human subject experiment (Kuo and Deshpande 2012). Thus, it is modelled using exponential functions in the form of

$$\tau_{s,j}(q_j) = A_j(e^{-B_j(q_j-E_j)} - 1) - C_j(e^{D_j(q_j-F_j)} - 1),^1 \quad (2.32)$$

¹ This equation represents a difference between two exponential functions. However, it is widely referred to as a double exponential function in the literature (Table 2.7).

(Esteki and Mansour 1996; Knutson et al. 2000; Silder et al. 2007; Kuo and Deshpande 2010; Deshpande et al. 2012; Kuo and Deshpande 2012; Agarwal et al. 2013), where j indicates the finger joint which is the index MCP F/E in this case, and $A_j, B_j, C_j, D_j, E_j,$ and F_j are parameters of the modelled joint stiffness torque (Table 2.8). A similar double exponential nature was also noticed at the PIP joint in stiffness experimental results of 89 subjects (Dionysian et al. 2005; Agarwal et al. 2013). Therefore, the double exponential model can be used for all finger joint F/E DoF for consistency (Agarwal et al. 2013).

The thumb stiffness torque is modelled as a linear function, which is proportional to the joint angle q_j and the displacement from its neutral position $q_{j,0}$ as

$$\tau_{s,j}(q_j) = -h_j(q_j - q_{j,0}), \quad (2.33)$$

(Wu et al. 2009a; Vignais and Marin 2014), where $\tau_{s,j}$ is the stiffness torque at thumb joint j , q_j is the current joint angle, h_j and $q_{j,0}$ are the joint stiffness constant and the joint neutral position given in Table 2.8, respectively. Similar to the assumption made by Wu et al. (2009a) that the stiffness in F/E is identical to that in Ab/Ad at the thumb MCP and CMC joints, the stiffness of F/E and Ab/Ad is assumed to be identical at the IP joint as well.

2.3 Results and discussion

2.3.1 Skeletal kinematic model

A Joint CoR estimation

Joint CoRs x_i are calculated using the estimated h_i in the inter-level mapping (Equation 2.16 and Algorithm 2.2). A comparison between the resulting joint CoRs and the surface markers during Task D2 is shown in Figure 2.10. The plausibility of the kinematic model is illustrated by the fact that as expected, all CoRs are located beneath the surface markers.

B Palm arc modelling

Modelling the palm arc is essential in specific tasks such as thumb opposition to pinky finger and various grasping tasks. Not considering the palm arc in modelling the human hand results in significant errors in ring and pinky finger pose estimation. This section highlights the effect of modelling the palm arc on the pose estimation accuracy of the pinky finger. This is performed by comparing the difference between the estimated and measured X_i resulting from static joint and 2 DoF joint palm arc models. The error between the estimated and measured X_i increases from Tip5 to MCP5 in the static palm joint model (Figure 2.11). The error E_i is calculated in terms of the Euclidean norm using Equation 2.28 and the model validation scheme in Figure 2.6. Among different subjects,

Table 2.8: Joint stiffness coefficients.

Digit	Joint j	Stiffness ^{a,b}					
		h_j [N.mm/°]			$q_{j,0}$ [°]		
1 st	CMC Ab/Ad	2.618			0		
	CMC F/E	2.618			0		
	MCP Ab/Ad	1.745			10		
	MCP F/E	1.745			10		
	IP Ab/Ad	0.873 ^c			5		
	IP F/E	0.873			5		
2 nd – 3 rd	MCP Ab/Ad	A_j	B_j	C_j	D_j	E_j	F_j
	MCP F/E	n.a.	n.a.	n.a.	n.a.	n.a.	n.a.
	PIP F/E	1.01	0.05	3.39	0.05	70.96	13.68
	DIP F/E	0.70	0.05	2.35	0.05	36.3	23.31
4 th – 5 th	MCP Ab/Ad	0.31	0.05	1.04	0.05	-10.99	06.06
	CMC Ab/Ad	n.a.	n.a.	n.a.	n.a.	n.a.	n.a.
	CMC F/E	n.a.	n.a.	n.a.	n.a.	n.a.	n.a.
	MCP Ab/Ad	n.a.	n.a.	n.a.	n.a.	n.a.	n.a.
	MCP F/E	1.01	0.05	3.39	0.05	70.96	13.68
	PIP F/E	0.70	0.05	2.35	0.05	36.3	23.31
DIP F/E	0.31	0.05	1.04	0.05	-10.99	06.06	

^a The coefficients in the 1st digit are based on Wu et al. (2009a) and Vignais and Marin (2014).

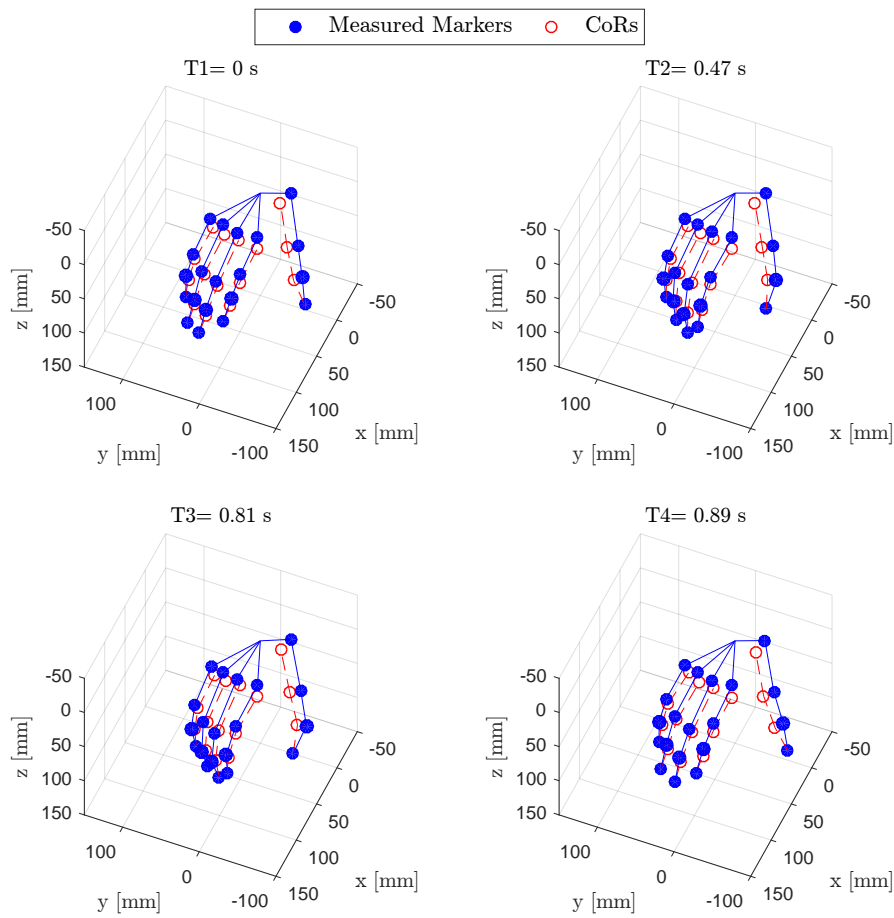
^b The coefficients in the index finger (2nd digit) are based on Agarwal et al. (2013) and are assumed to be the same in the other digits.

^c The coefficient in Ab/Ad DoF is assumed to be identical to that in F/E DoF.

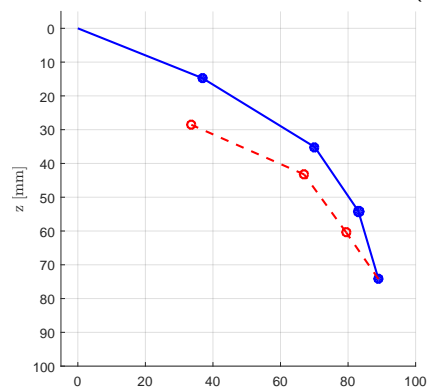
this error E_i is up to 70.0 mm, 20.4 mm, 10.6 mm, and 9.3 mm for \mathbf{X}_{MCP5} , \mathbf{X}_{PIP5} , \mathbf{X}_{DIP5} , and \mathbf{X}_{Tip5} , respectively (Figure 2.12). As one may notice, \mathbf{X}_{MCP5} exhibits the largest error, especially along the z -axis of the {BH} coordinate system (Figure 2.11 top). This phenomenon emphasises that the static joint model estimates \mathbf{X}_{MCP5} on the x - y plane of the {BH} (z -component close to zero), while the true position is shifted downwards to form the palm arc. In our proposed 2 DoF model, only sub-millimetre errors could be observed between estimated and measured \mathbf{X}_i (Figure 2.11 bottom).

C Thumb modelling

The proposed 6 DoF thumb model is compared with the state-of-the-art thumb models to highlight the accuracy of the proposed one, see Sub-section A Modelling assumptions for modelling details. In this section, thumb modelling results and considerations are discussed including the rotational relationship between {BT} and {BH} as well as thumb model DoFs and accuracy.



(a) A 3-D representation at four different instants (from T1 to T4).



(b) A 2-D representation of the index finger at the instant T2.

Figure 2.10: CoRs and surface marker locations during Task D2 for one exemplar subject.

Rotational relationship between $\{BT\}$ and $\{BH\}$

The identification of ${}^W R_{BH}$ and ${}^{BH} R_{BT}$ is explained in the Sub-section D Model identification and validation and Algorithm 2.1. A difference ranging between 10.6° –

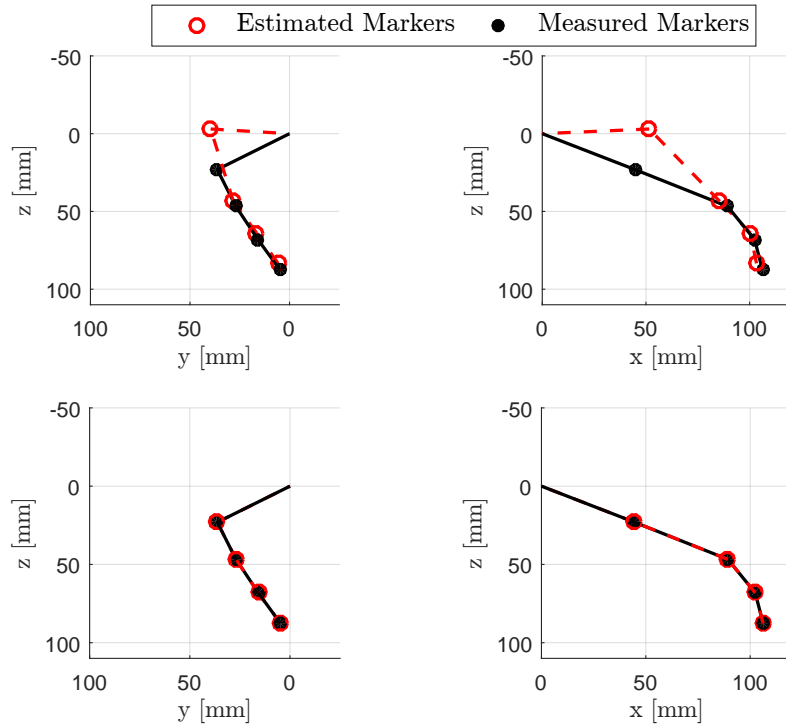


Figure 2.11: Comparison between measured and estimated \mathbf{X}_i in two palm arc models for CMC5 joint during thumb-pinky opposition task (Task S2 in Figure 2.9). Top: modelling the CMC5 joint as static joint (without considering the palm arc). Bottom: modelling the CMC5 joint as 2 DoF joint (with considering the palm arc). The figure shows the pinky finger expressed in $\{BH\}$.

24.3° was noticed among the subjects in ${}^{BH}\mathbf{R}_{BT}$. This difference is probably caused by the physiologic variation in the population and marker placement. Thus, the implemented identification of ${}^{BH}\mathbf{R}_{BT}$ for each subject results in a more accurate adaptable model that minimises the effect of the individual variations.

Thumb model DoFs and accuracy

The 6 DoF thumb model, which is the proposed model, is compared with 4 DoF and 5 DoF models, which are state-of-the-art thumb models (Figure 2.13). Clearly, the simplification of the DoFs in the state-of-the-art models affects the accuracy of the model, i.e. the difference in terms of the Euclidean norm between the estimated and measured \mathbf{X}_i . The estimated \mathbf{X}_i are calculated using the model validation scheme (Figure 2.6) while the measured \mathbf{X}_i are obtained using the optoelectronic motion capture system. In the 4 DoF model and due to not considering the Ab/Ad DoF of the MCP and IP joints, the error is up to 1.7 mm, 5.4 mm, 5.1 mm, and 2.1 mm for \mathbf{X}_{CMC1} , \mathbf{X}_{MCP1} , \mathbf{X}_{IP1} , and \mathbf{X}_{Tip1} , respectively. Compared to the 4 DoF model, the 5 DoF model shows improved

² The angular difference is defined as $\arccos(2\langle \xi_1, \xi_2 \rangle^2 - 1)$, where ξ_1 and ξ_2 denote the quaternions of two rotation matrices, and $\langle \cdot, \cdot \rangle$ is the inner product.

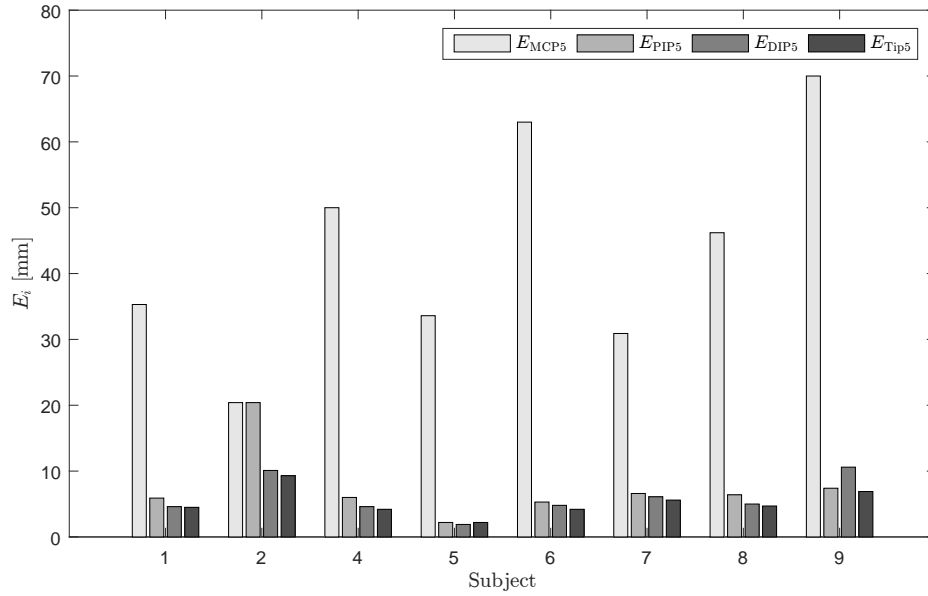


Figure 2.12: Maximum error (E_i) in the static joint model of CMC5 joint, where the palm arc is not considered. The error is expressed in terms of the Euclidean norm between estimated and measured \mathbf{X}_i in Task S2 (thumb-pinky opposition). Due to a measurement error, the data of subject 3 are not available for analysis in this task.

accuracy for all \mathbf{X}_i nearly to almost negligible error except in \mathbf{X}_{Tip1} . This is due to including the Ab/Ad DoF of the MCP joint but still lacking the Ab/Ad DoF of the IP joint. Similar results exist in the literature models (Table 2.9). This table shows that the 5 DoF models of (Cordella et al. 2014) and (Miyata et al. 2004) have an improved accuracy at CMC1, MCP1, and IP joints compared to the 4 DoF model of Cerveri et al. Yet, an error up to nearly 4 mm is observed in these models.

Although the IP joint has been modelled as a single DoF in the available thumb models (Parasuraman and Zhen 2009; Miyata et al. 2004; Metcalf et al. 2008; Cordella et al. 2014; Cerveri et al. 2007; Cobos et al. 2010), considering the Ab/Ad DoF is of vital importance to reconstruct tip positions accurately. A combination of F/E and Ab/Ad DoFs at the IP joint was observed in our pilot experiment, especially during interactions between the thumb segments and the grasped object, where the DP of the thumb rolls over the object's surface to achieve a stable grasp. This might be due to elastic joint capsules. Besides, there are non-constant bone segment lengths being reconstructed by 4 DoF and 5 DoF models. To tackle these issues, a 6 DoF model is proposed which includes 5 actuated DoFs and 1 passive DoF. This proposed model has an improved accuracy in all \mathbf{X}_i compared to the other two models (4 DoF and 5 DoF models) (Figure 2.13). Compared to the literature models (Table 2.9), the proposed 6 DoF model has proved to provide significantly better accuracy without a noticeable difference between measured and estimated \mathbf{X}_i .

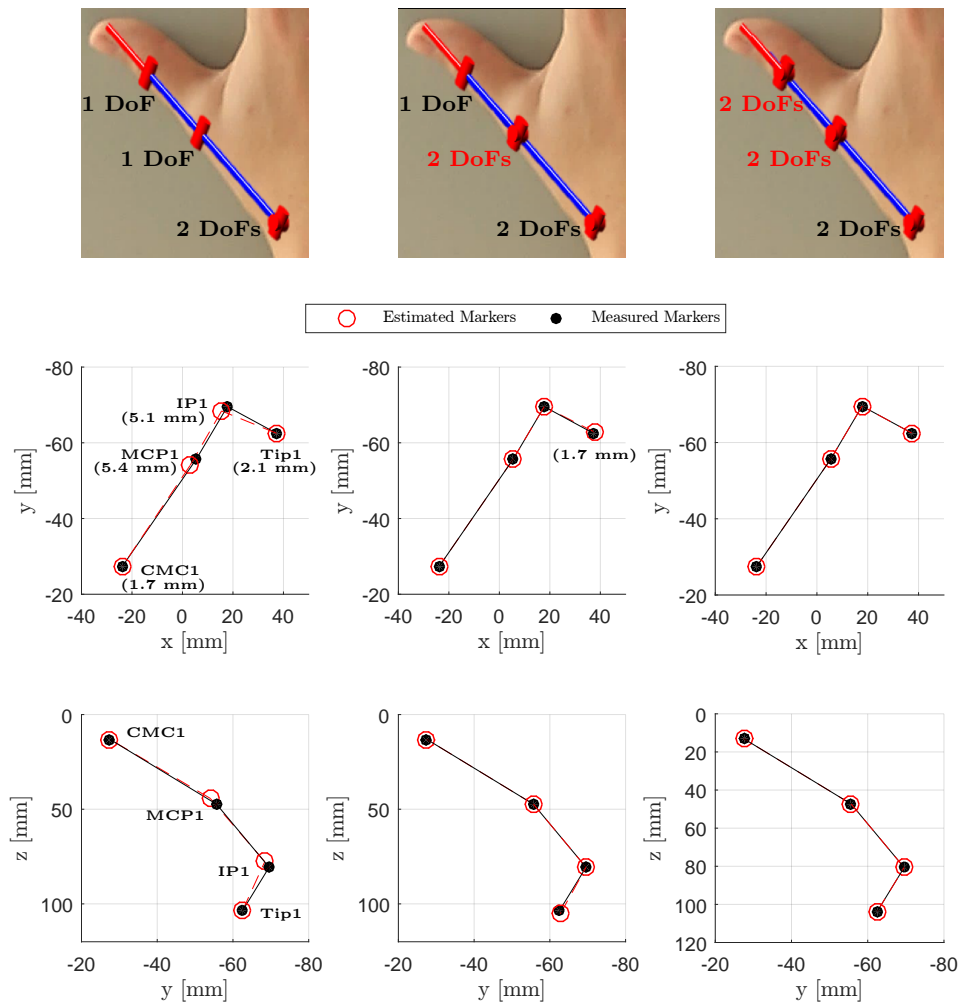


Figure 2.13: Comparison between measured and estimated X_i expressed in $\{BH\}$ for 4 DoF (left), 5 DoF (middle), and 6 DoF (right) models. The upper row shows a representation of the serial linkage of the compared three models. The numbers between parentheses represent the difference in terms of the Euclidean norm between the estimated and measured X_i .

D Surface kinematics and skeleton kinematics

In this section, three main issues are discussed and compared between surface and skeleton kinematics. These issues are: segment lengths, joint rotational angles, and Cartesian errors.

Segment lengths

In surface kinematics, $\|L_{\square}\|$ are calculated as the distance between the landmarks at the proximal and distal ends of the segment for each time point. On the other hand, in skeletal kinematics $\|l_{\square}\|$ are calculated as the distance between the estimated CoRs at the proximal and distal ends of the segment for each time point. The values $\|L_{\square}\|$ are different

Table 2.9: Comparison of accuracy among different thumb models from literature. The error was calculated as the maximum error of fingertip (Miyata et al. 2004), maximum of the errors in x -, y -, and z -directions (Cordella et al. 2014), and RMS error of the distance between estimated and measured marker positions (Cerveri et al. 2007).

Model	DoFs	E_{TM} [mm]	E_{MCP1} [mm]	E_{IP} [mm]	E_{Tip1} [mm]
Miyata et al. (2004)	5 ^a	n.a.	n.a.	n.a.	2.00
Cordella et al. (2014)	5	n.a.	0	0.77	4.33
Cerveri et al. (2007)	4	1.99 – 2.01	0.57 – 0.93	1.19 – 1.51	1.99 – 2.18

^a Although “8 DoFs” is mentioned explicitly in Miyata et al., three of them are the translation from {BH} to {BT}. Due to that, it has been considered as a 5 DoF model in this discussion for consistency.

from the estimated $\|\mathbf{l}_{\square}\|$ in Task D1 and Task D2 (Figure 2.14). Surface segmental length $\|\mathbf{L}_{\square}\|$ varies over time due to: 1) skin displacement relative to skeleton, and 2) rotation of markers about the DoF axes during movements. These reasons are more obvious in Task D2 and result in a larger variation in $\|\mathbf{L}_{\square}\|$ with the lowest and highest changes being observed in $\|\mathbf{L}_{DIP}\|$ and $\|\mathbf{L}_{PP}\|$, respectively. The lowest change is noted in $\|\mathbf{L}_{DIP}\|$ due to: 1) the skin stretching less over DIP joint compared to that over the other two joints (PIP and MCP), 2) placing the distal marker on the nail where no joint is located, and 3) having the smallest joint (DIP joint) diameter, which results in the least marker excursion. On the other hand, the highest change is noted in $\|\mathbf{L}_{PP}\|$ due to having: 1) the large mobility of the MCP joint which has 2 DoFs, 2) the greater skin stretching over the PIP and MCP joints, and 3) the large diameters of the PIP and MCP joints. The difference $\|\mathbf{L}_{\square}\|$ and $\|\mathbf{l}_{\square}\|$ shows that surface kinematics is different from skeletal kinematics. Consequently, $\|\mathbf{l}_{\square}\|$ should be used to calculate joint angles. As expected, the resulting segment lengths in the four fingers are equal to the anthropometrically modelled segment lengths from Buchholz et al. (1992) (Figure 2.14).

Joints rotational angles

Experimental data revealed a highly linear relationship between q_k and Q_k in Task D2 and Task D3 in F/E DoF with a coefficient of determination $R^2 \geq 0.94$ in most of the joints (Figures 2.15 and 2.16). From the linear regression fitting between q_k and Q_k , the difference between them in both slopes and intersects is clear.

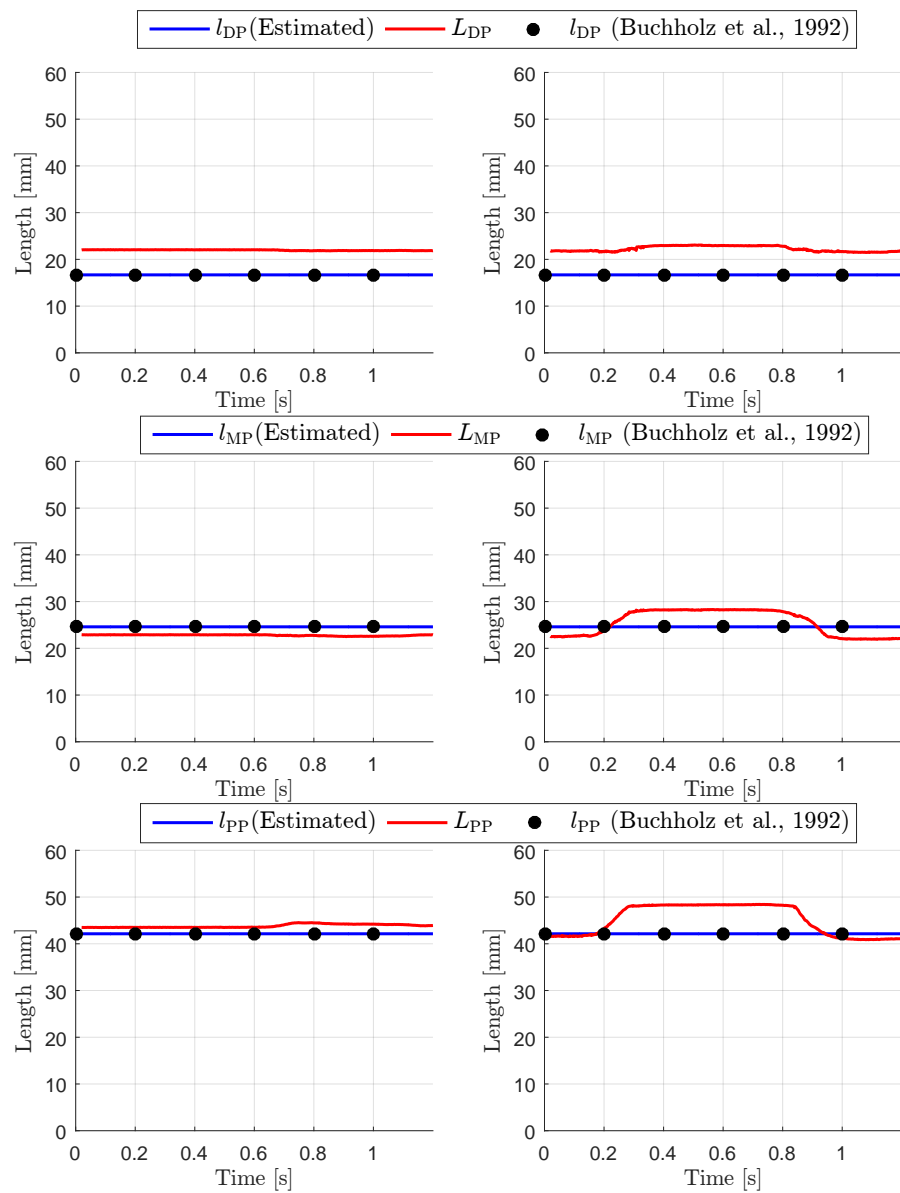


Figure 2.14: Comparison between $\|L_{\square}\|$ and the estimated $\|l_{\square}\|$ in Task D1 (left) and Task D2 (right). This figure shows segment lengths of an exemplar index finger. The estimated $\|l_{\square}\|$ are calculated as the distance between the estimated CoRs at the proximal and distal ends of the segment for each time point. The anthropometrically modelled segment lengths are calculated using the model proposed by Buchholz et al. (1992).

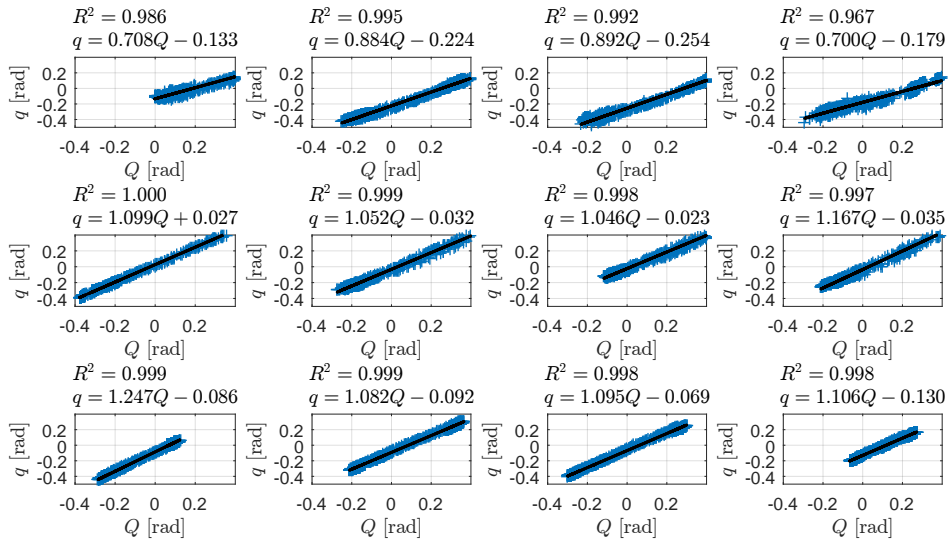


Figure 2.15: Skeleton rotational angles q_k with respect to surface rotational angles Q_k in Task D2. Columns indicate fingers (left to right): index, middle, ring, and pinky. Rows indicate rotational angles (top to bottom): DIP F/E, PIP F/E, MCP F/E. For MCP Ab/Ad, the rotational angles at the surface and skeleton levels are equal with $R^2 = 1.000$, thus they are not shown in this figure.

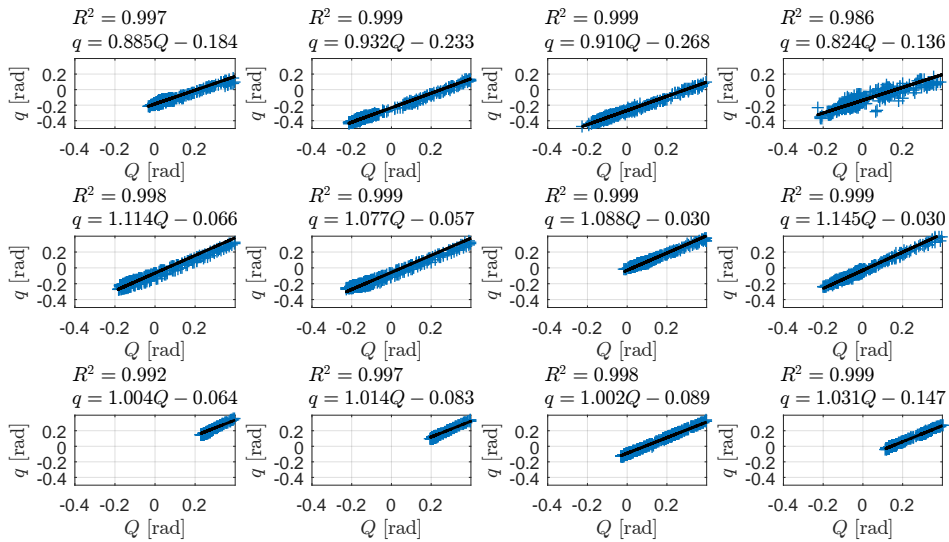


Figure 2.16: Skeleton rotational angles q_k with respect to surface rotational angles Q_k in Task D3. Columns indicate fingers (left to right): index, middle, ring, and pinky. Rows indicate rotational angles (top to bottom): DIP F/E, PIP F/E, MCP F/E. For MCP Ab/Ad, the rotational angles at the surface and skeleton levels are equal with $R^2 = 1.000$, thus they are not shown in this figure.

Errors in Cartesian space

The Cartesian errors are calculated as the difference in terms of the Euclidean norm between marker positions estimated by the forward kinematics model and the positions directly measured by the motion tracking system (Figure 2.6). In surface kinematics, an error increase is noted along the serial chain from MCP landmark to the tip of 2nd – 5th digits. The same phenomenon was noted in Cordella et al. (2014) and Cerveri et al. (2007) as well. This can be explained by the nature of the fingers, which are actually slightly curved rather than straight (Cordella et al. 2014) and results in $D_k \neq 0$ and $d_k \neq 0$ in the D-H parameters used (Table 2.4 and Table 2.3). This problem is solved and the model accuracy is improved by experimentally calculating D_k from motion tracking data and fitting d_k as a function of q_k (Figure 2.6).

A comparison between the proposed model and the comparable models in the literature is shown in Table 2.10. The models of Miyata et al. (2004) and Cerveri et al. (2007) have a better accuracy ($E_i \leq 2.98$ mm) compared to the model of Cordella et al. (2014) ($E_i \leq 10.67$ mm). In comparison to these models, the proposed model has proved to be highly accurate without a noticeable difference between measured and estimated \mathbf{X}_i (Figure 2.17). This sub-millimetre accuracy evidences the model self-consistency (Figure 2.6) and, ergo, reliable skeletal rotational angles \mathbf{q} can be obtained using the proposed method.

Table 2.10: Comparison of accuracy among different finger models (2nd – 5th digits) from the literature. The error E_i was calculated as the maximum error of fingertip (Miyata et al. 2004), maximum of the errors in x -, y -, and z -directions (Cordella et al. 2014), and RMS error of the distance between estimated and measured marker positions (Cerveri et al. 2007).

Model	E_{Index} [mm]	E_{Middle} [mm]	E_{Ring} [mm]	E_{Pinky} [mm]
Miyata et al. (2004)	1.47	2.25	2.98	2.67
Cordella et al. (2014)	6.90	8.00	6.67	10.67
Cerveri et al. (2007)	0.42 – 1.66	n.a.	n.a.	n.a.

2.3.2 Skeletal dynamic model

The results of the implemented skeletal dynamic model (Equation 2.29b) are presented and discussed in this section. First the results of the link torque τ_{Link} are presented and then the results of the passive torque τ_{p} .

The link torque τ_{Link} is modelled for the 26 DoFs of the hand (Figure 2.3). However, due to space limitation only the results of τ_{Link} of the three joints of the 2nd–5th digits in F/E DoF are discussed in this section. Also, this provides a clear comparison to evaluate the model (i.e. fingers configuration with respect to gravity). For the current discussion

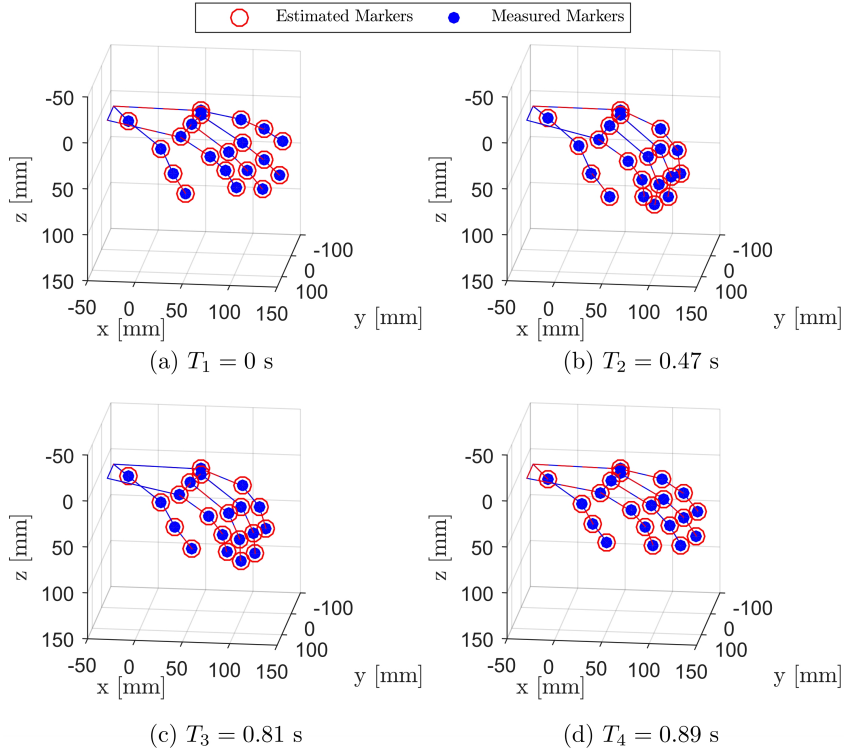


Figure 2.17: Comparison between measured and estimated \mathbf{X}_i in Task D2 for an exemplar subject at different instants (from T1 to T4). T1: start posture, T2: grasping, T3: start releasing, and T4: complete release.

a desired task of a repetitive F/E movement of the three joints is simulated using a sinusoidal function (Figure 2.18), which is defined as

$$\begin{aligned}
 q_{\text{MCP}} &= 55^\circ \sin(2t + 5.5) + 45^\circ, \\
 q_{\text{PIP}} &= 55^\circ \sin(2t + 5.5) + 55^\circ, \\
 q_{\text{DIP}} &= 40^\circ \sin(2t + 5.5) + 40^\circ.
 \end{aligned} \tag{2.34}$$

Among the three joints, a maximum peak-to-peak τ_{Link} of 0.013 N.m, 0.017 N.m, 0.013 N.m, and 0.007 N.m is observed at the MCP joint of the index, middle, ring, and pinky fingers, respectively (Figure 2.18). This is an expected result as the MCP joint is influenced by the whole finger weight. Similarly, as the middle finger has the highest bone segment weights compared to the other fingers (Table 2.5), it has the highest peak-to-peak τ_{Link} of 0.017 N.m, 0.006 N.m, and 0.001 N.m at the three joints, respectively (Figure 2.18).

The maximum resulting damping torque τ_d is 0.14 N.m, 0.05 N.m, and 0.02 N.m at the MCP, PIP, and DIP joints, respectively (Figure 2.19). The torque τ_d is linearly dependent on $\dot{\mathbf{q}}$, which is calculated as the derivative of the joint configuration \mathbf{q} . Consequently, τ_d

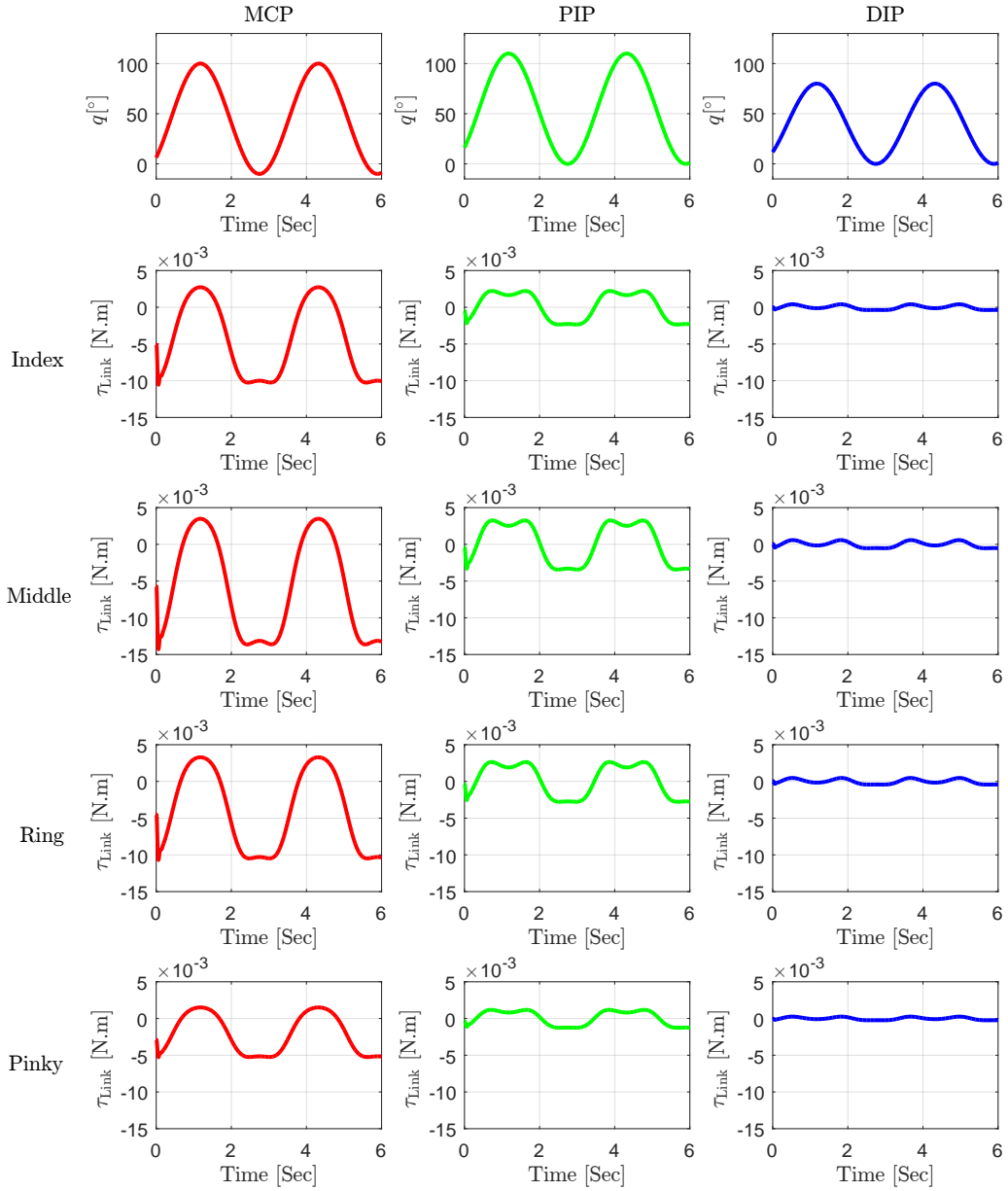


Figure 2.18: The resulting link torque τ_{Link} of the four fingers for a simulated repetitive F/E motion (Equation 3.17).

is positive when \dot{q} is positive due to the increase of q (joint flexion) and negative when \dot{q} is negative due to the decrease of q (joint extension).

The modelled stiffness torque τ_s at the MCP joint ranges between -0.15 N.m and 0.05 N.m (Figure 2.20). The torque τ_s shows exponential decrease/increase with joint increase/decrease. The torque of the PIP joint and the DIP joint shows almost a similar response between 0° and 80° . This might be due to the coupling between these two joints where a strong correlation between the DIP and PIP joints exist (Troncossi et al. 2016).

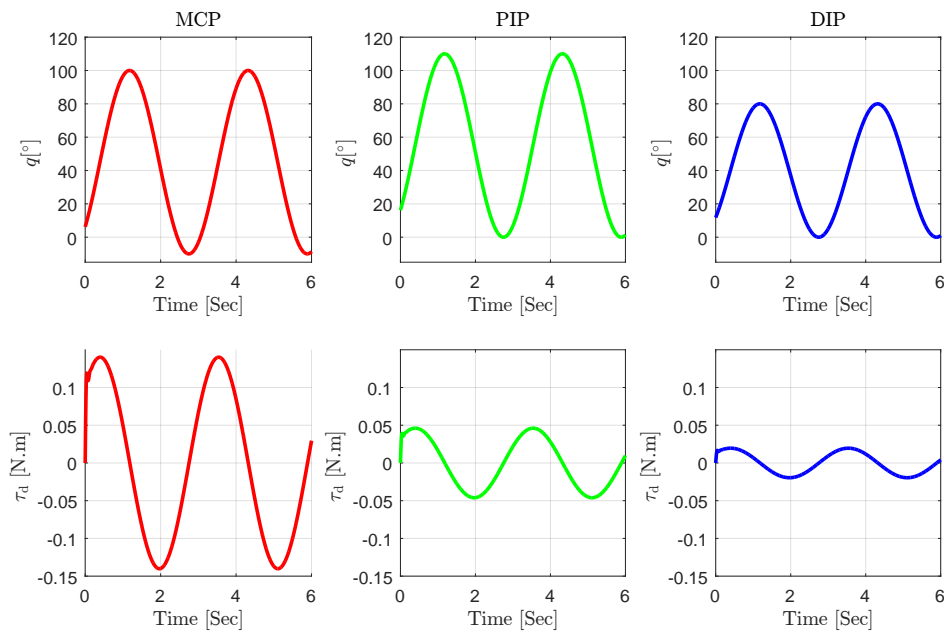


Figure 2.19: The results of the damping torque τ_d model in the index finger. Top: a simulated repetitive F/E motion for the three joints of the index finger (Equation 3.17). Bottom: the resulting τ_d .

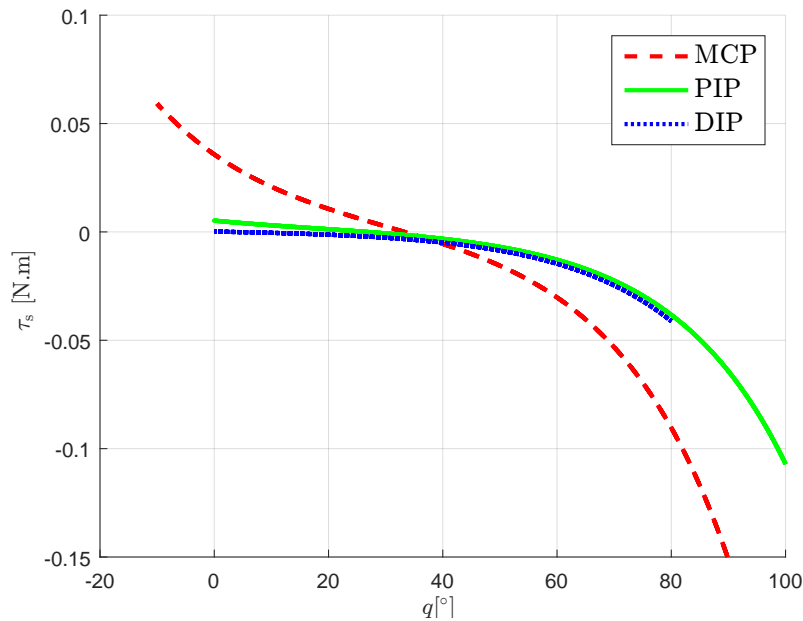


Figure 2.20: The modelled joint stiffness torque τ_s in the three joints of the index finger.

Finally, the three torques modelled, i.e. τ_{Link} , τ_d , and τ_s , at the index finger MCP joint for the same simulated MCP F/E motion in Equation 3.17 are shown in Figure 2.21. The peak-to-peak torques are 0.011 mN.m, 0.28 N.m, and 0.3 N.m for τ_{Link} , τ_d , and τ_s , respectively. The torque τ_{Link} is significantly smaller than the other two torques (τ_d and τ_s). This is in agreement with Deshpande et al. (2012) who pointed out that the visco-

elastic component is dominant over the dynamic component (τ_{Link}). This emphasises the importance of integrating the passive torque model in skeletal dynamic modelling.

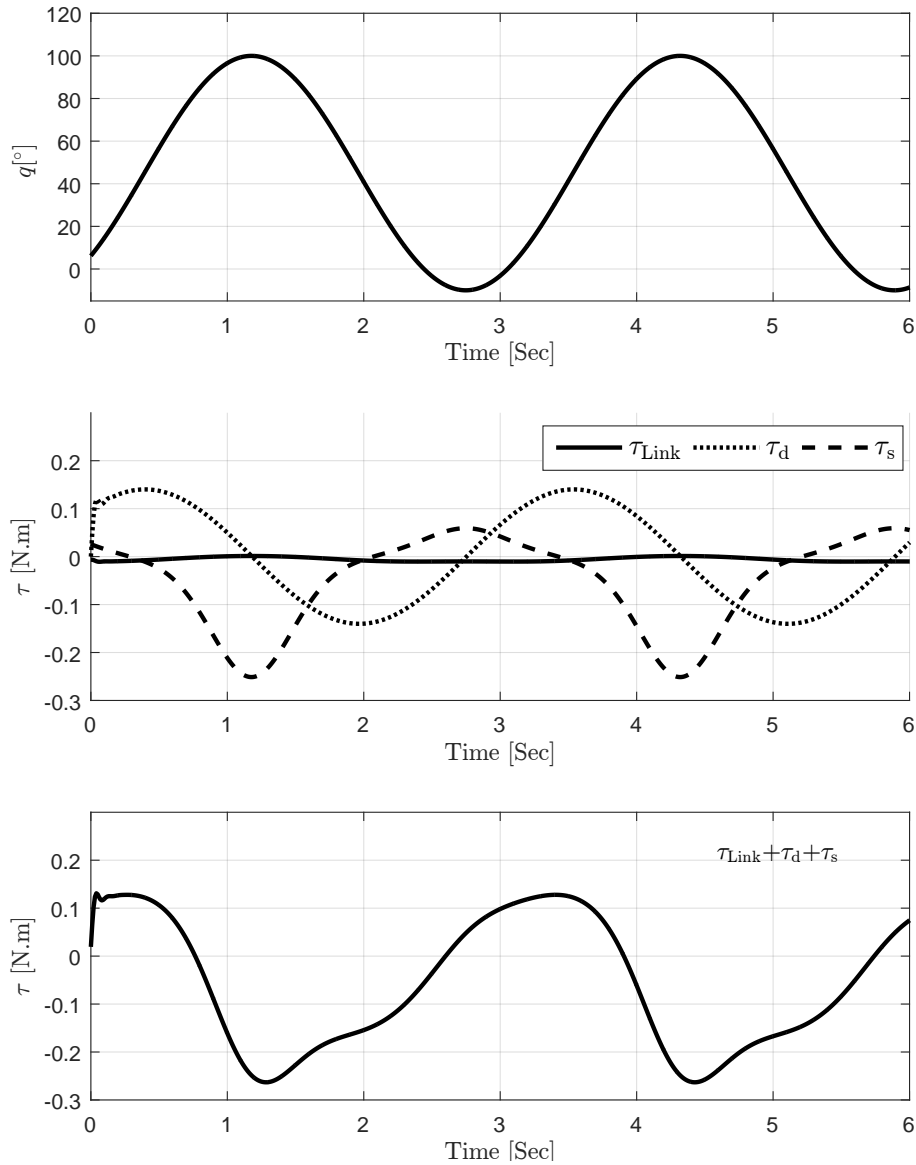


Figure 2.21: Torque components in the index MCP joint for a given joint configuration. Top: the given MCP joint configuration (Equation 3.17). Middle: the resulting link torque τ_{Link} , damping torque τ_{d} , and stiffness torque τ_{s} . Bottom: the resulting total torque, i.e. $\tau_{\text{Link}} + \tau_{\text{d}} + \tau_{\text{s}}$.

2.4 Conclusion

In this chapter, two skeletal models are presented: a kinematic model and a dynamic model. An accurate human hand kinematic model, including the four fingers (4 actuated DoFs each), the thumb (5 actuated DoFs and 1 passive DoF), and the palm arc (4 actuated DoFs), has been proposed along with an identification procedure that estimates

joint CoRs. The sub-millimetre difference between surface marker positions estimated by the forward kinematics model and the positions directly measured by the motion tracking system proves the fidelity of the mathematical formulations of the model and the associated identification procedure. The proposed thumb model with the 5 actuated DoFs (under-actuated by muscles) and the 1 passive DoF (driven by physical thumb-object interactions) has significantly improved accuracy compared to existing thumb models. Despite the fact that we did not investigate similar passive movements in the other digits, the passive DoFs obviously exist in the other digits and should be further investigated in the future. The skeletal dynamic model estimates both the link torque due to gravitational and inertial forces and the passive torque due to the passive joint properties. While the link torque model includes the complete hand DoFs, the passive torque is limited to the 6 DoFs of the thumb and 3 DoFs of the fingers (F/E DoFs only). Future work will address: 1) the passive DoFs (joint elasticity) in all hand joints with respect to the physical finger-object interaction, 2) the changes of the D-H parameter d_k during tasks and its relation to joint elasticity, and 3) extending the passive torque model to include the complete 26 DoFs of the human hand.

Chapter 3

Musculotendon kinematics and dynamics

*Parts of this chapter have been published in
Computer Methods in Biomechanics and Biomedical Engineering, 2019, 22(7):727-739,
and
The 16th International Symposium on Computer Methods in Biomechanics and
Biomedical Engineering, New York City, United States, Aug 2019.*

3.1 Introduction

The musculotendon unit represents the actuator of the human musculoskeletal system and transforms muscle activation into muscle contraction (force). Generally, in order to model and simulate the dynamic behaviour of a musculoskeletal system, one needs:

1. The musculotendon force model, e.g. a Hill-type muscle model (Hill 1938; Zajac 1989; Winters 1990).
2. The transformation from musculotendon forces to joint torques, which is the matrix of muscle moment arms $\mathbf{J}^T(\mathbf{q})$, commonly known as musculotendon excursion moment arms.

These requirements are met by two connected models, namely a musculotendon dynamic model and a musculotendon kinematic model (Figure 3.1). The musculotendon kinematic model computes the musculotendon lengths $l_{mt}(\mathbf{q})$, length change rates $\dot{l}_{mt}(\mathbf{q}, \dot{\mathbf{q}})$, and $\mathbf{J}^T(\mathbf{q})$ for a given joint configuration \mathbf{q} . The output of the musculotendon kinematic model alongside muscle activation \mathbf{u} are fed into the musculotendon dynamic model which estimates the musculotendon forces \mathbf{F}_{mt} and, together with the moment arms $\mathbf{J}^T(\mathbf{q})$, torques $\boldsymbol{\tau}_{mt}$.

This chapter discusses the theoretical background required to understand the developed models, state-of-the-art, model development, and results for the musculotendon kinematics and dynamics.

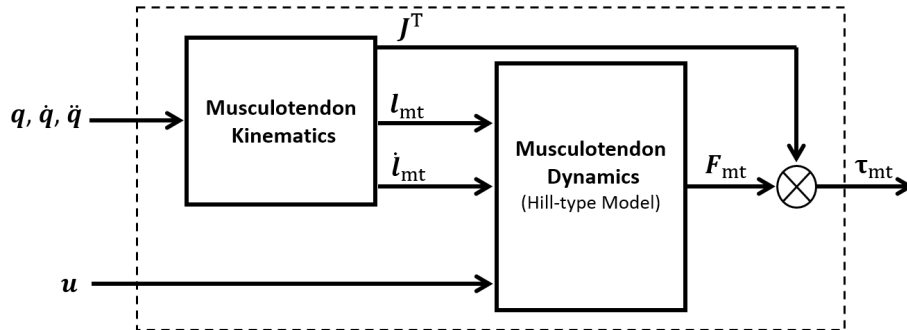


Figure 3.1: The connection between the musculotendon kinematic model and the musculotendon dynamic model.

3.1.1 Biomechanics of skeletal muscle

This sub-section explains the biomechanics of the skeletal muscle based on Oatis (2016) and Hall (2011). The functional unit that produces motion at a joint, which is the musculotendon unit, consists of two discrete units, i.e. the muscle belly and the tendon. The tendon is a connective tissue that binds the muscle belly to the bone. The muscle belly consists of muscle cells, or fibers, that produce the contraction and the connective tissue encasing the muscle fibers.

A skeletal muscle fiber is a long cylindrical, multinucleated cell that is filled with smaller units of filaments (Figure 3.2). The largest of the filaments is the myofibril, which is composed of subunits called sarcomeres. The sarcomere is the basic functional unit of the muscle. It contains two types of myofilaments, i.e. actin myofilament, which is the thinner myofilament composed of the actin protein molecules, and myosin myofilament, which is the thicker myofilament composed of the myosin protein molecules. The sliding of actin myofilament on the myosin chain is the basic mechanism of muscle contraction. Contraction of a whole muscle is actually the result of summation of singular contraction events occurring within the individual sarcomeres.

organisation of the sarcomere is shown in Figure 3.2. The sarcomere is compartmentalised between two Z lines and bisected by an M line. While the I band represents the zone of thin actin filaments only, the A band represents the zone occupied by both the actin and myosin filaments. In the centre of the A bands are the H zones, which contain only the thick myosin filaments. Contraction happens as a result of the formation of cross-bridges between the myosin and actin myofilaments, causing the actin chains to “slide” on the myosin chain (Figure 3.3). The tension of the resulting contraction depends on the number of cross-bridges formed between the actin and myosin. Thus, the maximum contractile force occurs at the maximum number of cross-links between

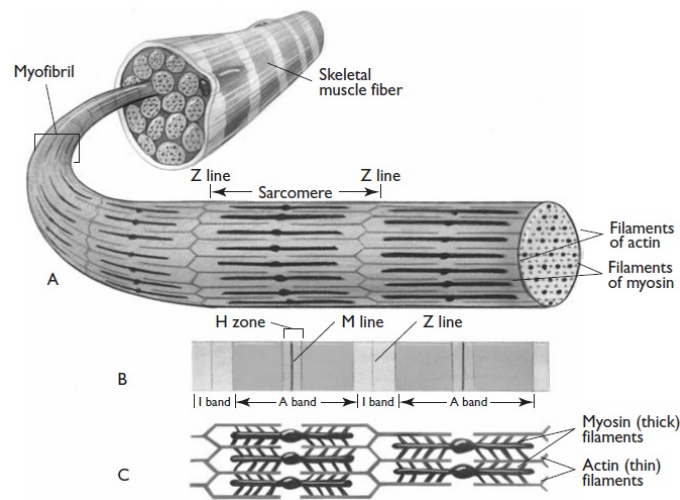


Figure 3.2: Structure of skeletal muscle. Adapted from Hall (2011).

the actin and myosin myofilaments. This maximum number of cross-links happens when the full length of the actin strands at each end of the sarcomere are in contact with the myosin molecule (Figure 3.4). This length is defined as the resting length or the optimal muscle length. The sarcomere can shorten from its resting length, which results in a reduction of the available sites for cross-bridge formation and consequently force of contraction decreases. Similarly, when the sarcomere is stretched from its resting length, contact between actin and myosin myofilaments decreases which results in a reduction in the number of cross-links and consequently the force of contraction decreases.

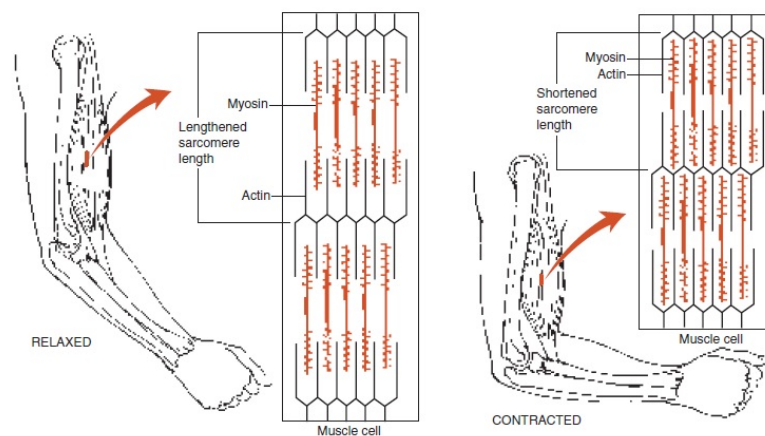


Figure 3.3: The sliding filament model. Sliding of the actin chains on the myosin chains results in contraction of the skeletal muscle. Adapted from Oatis (2016).

Muscle contraction is initiated by an electrical stimulus from the associated motor neuron (Figure 3.5). This stimulus causes depolarisation of the muscle fibre which results in Calcium release into the cell and binds with the regulating protein troponin. This combination of calcium with troponin acts as a trigger to bind actin to myosin, which

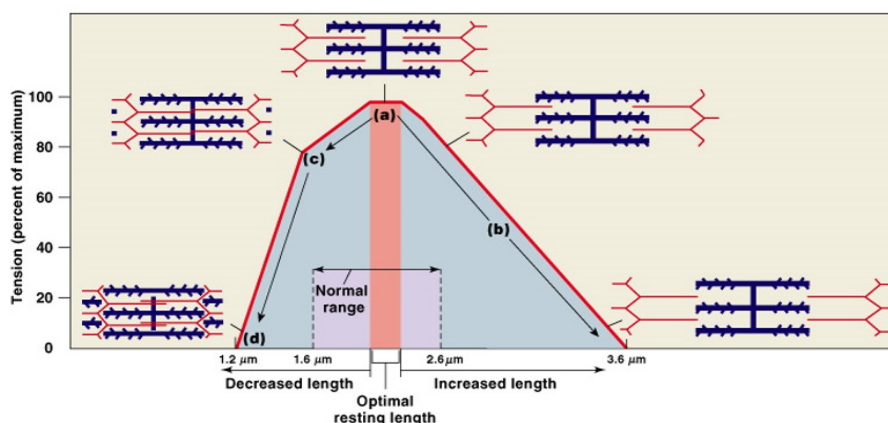


Figure 3.4: Length-tension curve. Adapted from Martini et al. (2012).

initiates the contraction. On the other hand, cessation of the nerve's stimulus results in a reduction in calcium levels within the muscle fibre, inhibiting the cross-bridges between actin and myosin, and finally the muscle relaxes. The aforementioned electromechanical stages of excitation-contraction produce an electromechanical temporal delay between the initiation of an action potential and the muscle contraction of between 10 ms and about 100 ms (Corcos et al. 1992; Buchanan et al. 2005) (Figure 3.6), i.e.

motor unit action potential \rightarrow open the ion channels (*delay*) \rightarrow Ca^{+2} flow (*delay*) \rightarrow
 free the bonding sites (*delay*) \rightarrow cross-bridging (*delay*) \rightarrow muscle contraction.

3.1.2 Musculotendon kinematic model

The tendon is a fibrous connective tissue that mechanically connects an acting muscle with a bone. When a muscle contracts, it pulls on the tendon, which in turn transfers load from the muscle to the bone to achieve the desired motion. The musculotendon excursion moment arm relates the change of musculotendon excursions to the change of joint angles and also the muscle forces to the joint torques. From the differential kinematics in robotics, it is well known that the relation between force and joint torque is given by the transposed Jacobian of the direct kinematics. Previous cadaveric and human studies showed that the moment arm matrix is a non-linear, a function of all joint angles, and subject dependent, i.e. that varies significantly from one person to another (An et al. 1983; Brand et al. 1975; Fowler et al. 2001; Deshpande et al. 2008). Thus, a kinematic model that is able to estimate $\mathbf{J}^T(\mathbf{q})$ while accounting for its variations is needed to more closely represent in-vivo muscle driven torque generation behaviour.

The musculotendon length $l_{\text{mt}}(\mathbf{q})$, which is required to derive $\mathbf{J}^T(\mathbf{q})$, can be derived from a so-called musculotendon path model. The musculotendon path describes the complete route of the musculotendon unit from its origin to its insertion by means of via-points and bony-structure wrapping in 3-D space. Muscles wrap and bend around underlying

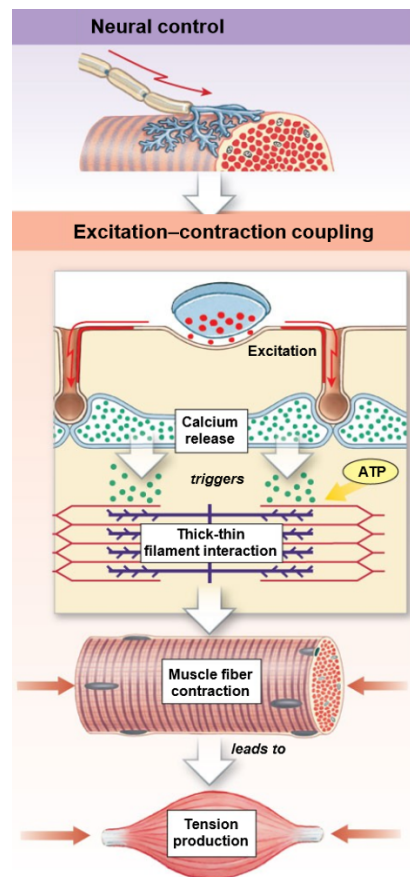


Figure 3.5: Steps of excitation-contraction. Adapted from Martini et al. (2012).

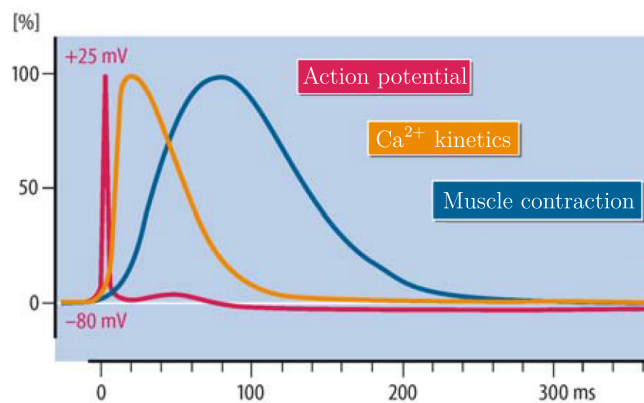


Figure 3.6: The associated time delay between action potential and muscle contraction. Adapted from Linke and Pfitzer (2007) and Hu (2015).

anatomical structures, i.e. bones, especially bony prominences (Pigeon et al. 1996). Computer models of the musculoskeletal system define via-points and wrapping surfaces to geometrically constrain the path from penetrating underlying structures (Blemker and Delp 2005) (Figure 3.7). These wrapping surfaces or the anatomical constraints are known as obstacles in computational models. Different obstacle-set geometries have been proposed to model different anatomical constraints (Garner and Pandy 2000) (Figure 3.8).

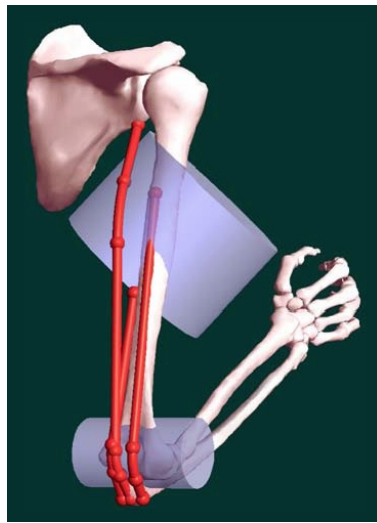


Figure 3.7: Illustration of the obstacle-set model used to represent the paths of the three heads of the triceps brachii. Adapted from Garner and Pandy (2000).

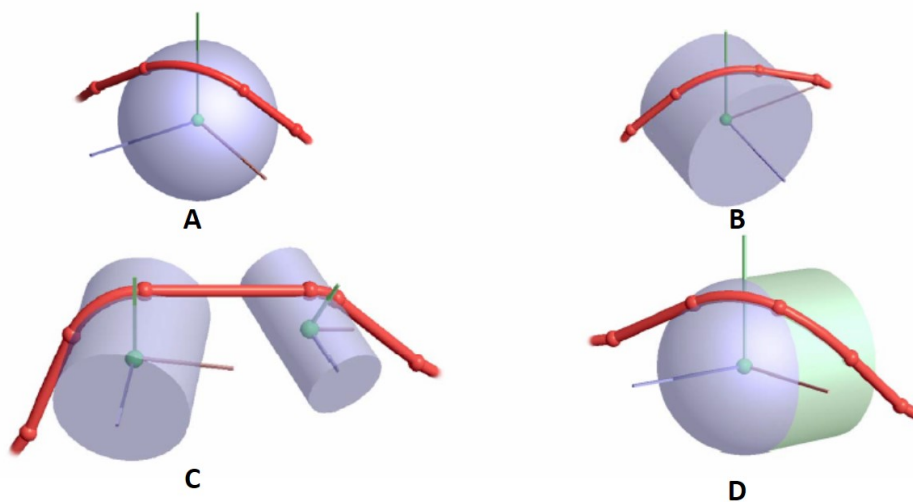


Figure 3.8: Graphical representation of obstacle-sets: (A) single sphere, (B) single cylinder, (C) double cylinder, and (D) sphere-capped cylinder. Adapted from Garner and Pandy (2000).

So far, only a few musculotendon path models for the human hand have been proposed (Holzbaur et al. 2005; Lee et al. 2015). These models have essential limitations related to: 1) the underlying skeletal kinematic model, 2) the muscles included, and 3) the software platform used (Table 3.1). The limitations of the state of the art are discussed as follows.

A Skeletal kinematic model

Skeletal kinematic models are used to define the bone-fixed coordinate systems where musculotendon attachment points, via-points, and obstacles are expressed. Human hand muscles are either extrinsic muscles, when the muscle belly is located in the forearm, or

intrinsic muscles, when the muscle belly is located in the hand. Therefore, in order to implement all the intrinsic and extrinsic muscles, the skeletal model should consist of the hand and at least the forearm. Thus, the skeletal models of the hand and the arm are discussed here.

The musculoskeletal model of Holzbaaur et al. (2005) includes 15 degrees of freedom (DoFs) representing the shoulder, elbow, forearm, wrist, thumb, and index finger. Lee et al. (2015) extended Holzbaaur et al. model by adding the DoFs of the middle, ring, and pinky fingers. Yet, this model still lacks some DoFs, i.e. the abduction/adduction of the thumb metacarpophalangeal (MCP) joint and of the carpometacarpal (CMC) joint of the ring and pinky fingers (Table 3.1). Modelling the complete DoFs of the digits results in an anatomically correct model with improved accuracy. For example, the proposed 6 DoF thumb model has an improved accuracy (i.e. sub-millimetre error) compared to the previously developed models of 4 DoFs and 5 DoFs (i.e. the error is up to 1.7 mm) as shown in Figure 2.13.

B Included muscles

In the upper limb model of Holzbaaur et al. (2005), the hand muscles were limited to the extrinsic muscles only, including: Flexor Digitorum Profundus (FDP), Flexor Digitorum Superficialis (FDS), Flexor Pollicis Longus (FPL), Extensor Digitorum (Communis) (EDC), Extensor Digiti Minimi (EDM), Extensor Indicis (Proprius) (EIP), Extensor Pollicis Longus (EPL), Extensor Pollicis Brevis (EPB), and Abductor Pollicis Longus (AbPL). Lee et al. (2015) extended this model to include more extrinsic and intrinsic finger muscles, e.g. Palmar Interossei (PI) and Dorsal Interossei (DI). Nevertheless, this model still lacks several intrinsic hand muscles such as Abductor Digiti Minimi (AbDM) and Opponens Digiti Minimi (ODM) (Table 3.1). Including all hand muscles results in an anatomically correct model that provides a better understanding of the human neuromechanics.

C Software platform

Both models of Holzbaaur et al. (2005) and Lee et al. (2015) were developed in OpenSim. OpenSim is an open-source platform on which the biomechanics community can model, simulate, and analyse the neuromusculoskeletal system (Delp et al. 2007). It has been successfully used to model the musculoskeletal movements and predict surgical outcomes. However, this model is implemented in MATLAB[®] Simulink[®] Toolbox (The MathWorks, Inc., USA) so that the developed musculotendon kinematic model will be easily integrated with the other models proposed in this thesis and their future work. On the other hand, Simulink[®] is more suitable for designing and implementing closed-loop human hand motor control and simulating rather complex physical interaction with the environment.

Table 3.1: State-of-the-art hand musculoskeletal models and the contribution of the present work.

Comparison		Holzbaur et al. (2005)	Lee et al. (2015)	This work	
Skeletal system	Hand				
	Thumb	4 DoFs	4 DoF	6 DoF ^a	
	Index finger	4 DoFs	4 DoFs	4 DoFs ^a	
	Middle finger	n.a	4 DoFs	4 DoFs ^a	
	Ring finger	n.a	4 DoFs	6 DoFs ^a	
	Little finger	n.a	4 DoFs	6 DoFs ^a	
	Arm				
	Shoulder	3 DoFs	3 DoFs	3 DoFs	
	Elbow	2 DoFs	2 DoFs	2 DoFs ^b	
Wrist	2 DoFs	2 DoFs	2 DoFs ^b		
Muscles	Extrinsic	Flexor Digitorum Profundus (FDP)	✓	✓ ^c	✓
		Flexor Digitorum Superficialis (FDS)	✓	✓ ^c	✓
		Flexor Pollicis Longus (FPL)	✓		✓
		Extensor Digitorum (Communis) (EDC)	✓	✓ ^c	✓
		Extensor Digiti Minimi (EDM)	✓		✓
		Extensor Indicis (Proprius) (EIP)	✓		✓
		Extensor Pollicis Longus (EPL)	✓		✓
		Extensor Pollicis Brevis (EPB)	✓		✓
		Abductor Pollicis Longus (AbPL)	✓		✓
	Intrinsic	Flexor Pollicis Brevis (FPB)			✓
		Adductor Pollicis (AdP)			✓
		Abductor Pollicis Brevis (AbPB)			✓
		Opponens Pollicis (OP)			✓
		Lumbricals (LU)		✓ ^c	✓
		Flexor Digiti Minimi (FDM)			✓
		Abductor Digiti Minimi (AbDM)			✓
		Opponens Digiti Minimi (ODM)			✓
		Palmar Interossei (PI)		✓ ^c	✓
		Dorsal Interossei (DI)		✓ ^c	✓
		Software platform	OpenSim ^d	OpenSim ^d	MATLAB [®] Simulink [®] Toolbox

^a The proposed 26 DoF skeletal kinematic model (Section 2.2.1)

^b Garner and Pandy (1999)

^c Lee et al. (2015) added these muscles to the model of Holzbaur et al. (2005)

^d Delp et al. (2007)

3.1.3 Musculotendon dynamic model

The dynamics of the muscle tissue can be divided into activation dynamics and muscle contraction dynamics (Zajac 1989) (Figure 3.9). These muscle dynamics types are explained in the following.

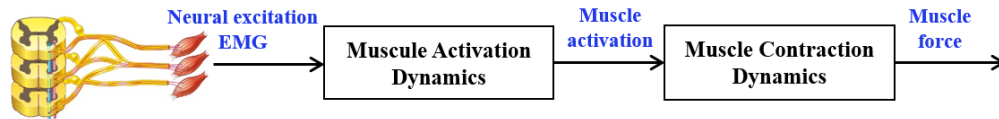


Figure 3.9: Muscle dynamics, which is divided into activation dynamics and muscle contraction dynamics.

A Activation dynamics

Activation dynamics is the process of transforming the neural excitation produced by the nervous system into activation of the contractile element (Figure 3.9). The surface electromyogram sEMG technique is used to measure the sum of all motor action potentials of a relevant muscle. Thus, the EMG signal contains information of the count of the firing motor units which are related to muscle force. However, it is not muscle activation yet; muscle contraction is coupled to the action potential electromechanically (Hu 2016) (Figure 3.5). These electromechanical stages, such as opening the ion channels and fluid flow of Ca^{+2} , produce electromechanical lag that has been reported to range from 10 ms to about 100 ms (Corcos et al. 1992; Buchanan et al. 2005) (Figure 3.6).

The activation dynamics, which is out of the scope of this thesis, can be modelled as a simplified first-order system (Winters 1990) or a second order system (Winters 1990; Thelen et al. 1994; Lloyd et al. 1996; Lloyd and Besier 2003; Buchanan et al. 2005). In these models, the EMG signal was processed before transforming it to activation. This processing includes averaging, filtering, rectification, and normalisation (Artemiadis and Kyriakopoulos 2007; Artemiadis and Kyriakopoulos 2010; Cram and Kasman 1998a; Cavallaro et al. 2005; Cavallaro et al. 2006; Konrad 2005; Hu 2015; Hu 2016).

B Muscle contraction dynamics

Muscle contraction dynamics is concerned with the transformation of muscle activation in muscle force (Figure 3.9). To simulate this process, mathematical models are used to describe the resulting musculotendon force for a specific motion. The mathematical description of muscle dynamics depends on the type of problem to solve (Romero and Alonso 2016). Despite the fact that the Huxley model (Huxley 1958) describes precisely the chemical and mechanical processes that take place during muscle contraction, the model complexity increases considerably in studies that include multiple musculotendon units (Romero and Alonso 2016). Therefore, Hill-type muscle models (Hill 1938) are used to calculate musculotendon forces in these studies because of their simplicity compared to the Huxley model (Romero and Alonso 2016).

The classical structure of the Hill-type muscle model, which is thoroughly described in Zajac (1989) and Winters (1990), consists of a contractile element (CE) that is surrounded both in series and in parallel by "passive" connective tissue. The series element (SE) represents the tendon and a parallel element (PE) represents the passive muscle stiffness (Figure 3.10). The CE is the active force generation element in the muscle and generates force that has both force-length and force-velocity properties. The PE describes the passive elastic properties of the muscle fibre and has force-length property.

Since the classic work of Hill (1938), physiologists and biomechanicians have proposed many models (Audo and Davy 1985; Van Soest and Bobbert 1993; Jager 1996; Martins et al. 1998; Rosen et al. 1999; Kaplan 2000; Silva 2003; Vilimek 2007; Kuo and Deshpande

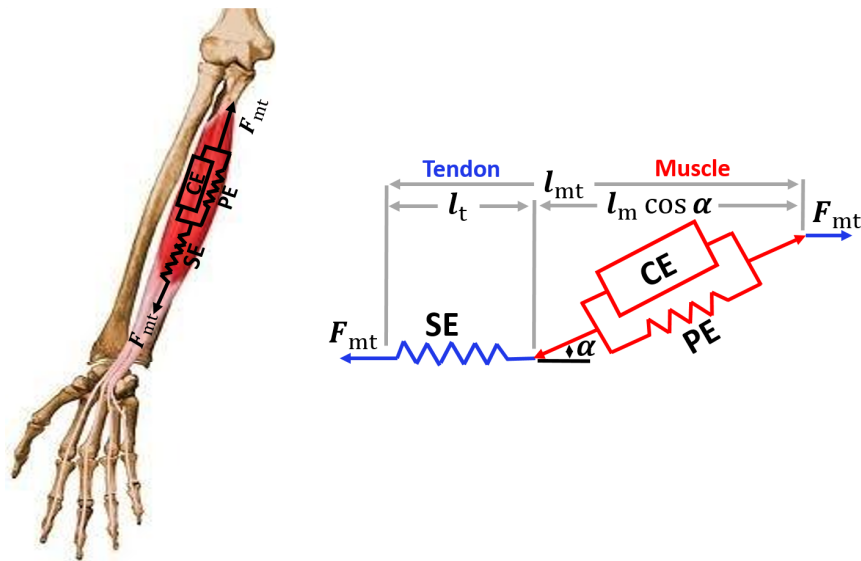


Figure 3.10: Representation of classical structure of Hill-type muscle model, with contractile element (CE), series element (SE, larger spring) representing the tendon, and parallel element (PE) representing the passive muscle stiffness.

2010; Haeufle et al. 2014; Jovanovic et al. 2015; Kuthe et al. 2015; Hu 2015; Hu 2016; Hamouda et al. 2016; Romero and Alonso 2016). A qualitative similarity can be noticed between different Hill-type muscle model curves with small differences that should be mentioned (Figure 3.11). The CE force–length relationship is not centred on the normalised muscle length $l_m/l_{m,o} = 1$ in some formulations (Silva 2003; Rosen et al. 1999), and the bell shape of the models of Silva (2003) and Rosen et al. (1999) is a bit flat in the middle. The CE force–velocity relationship is slightly different among the compared models, which may result in variations of the calculated force from different approaches. Despite the qualitative similarity between the curves of PE force–length relationship, especially in the normalised muscle length interval $[0 \ 1.6]$, a significant divergence is present for values of $l_m/l_{m,o} > 1.6$. However, these values are rarely reached in normal movements (Romero and Alonso 2016).

3.1.4 Contribution

This chapter discusses the development of the musculotendon kinematic and dynamic models. Specifically, the contributions are:

1. Developing a complete computational model for musculotendon paths and muscle–joint kinematics of all extrinsic and intrinsic hand muscles implemented in the MATLAB® Simulink® Toolbox. This model is based on the developed 26 DoF hand kinematic model (Section 2.2.1) with *all* intrinsic and extrinsic muscles which are represented by 47 musculotendon paths (Figure 3.12). The model is implemented in Simulink® as it provides a framework for designing and implementing closed-

loop human hand motor control and simulating rather complex physical interaction between the human hand and the environment.

- Extending the musculotendon kinematic model of the index finger to include a musculotendon dynamic model and an activation estimation model. The musculotendon dynamic model (Hill-type muscle model) is utilised that calculates the musculotendon forces for given musculotendon lengths and length change rates, which are obtained from the musculotendon kinematic model, and muscle activations. Muscle activations, which are obtained from the proposed muscle activation estimation model, are optimised with a minimum difference between the resulting torque from the musculotendon dynamic model and skeletal dynamic model.

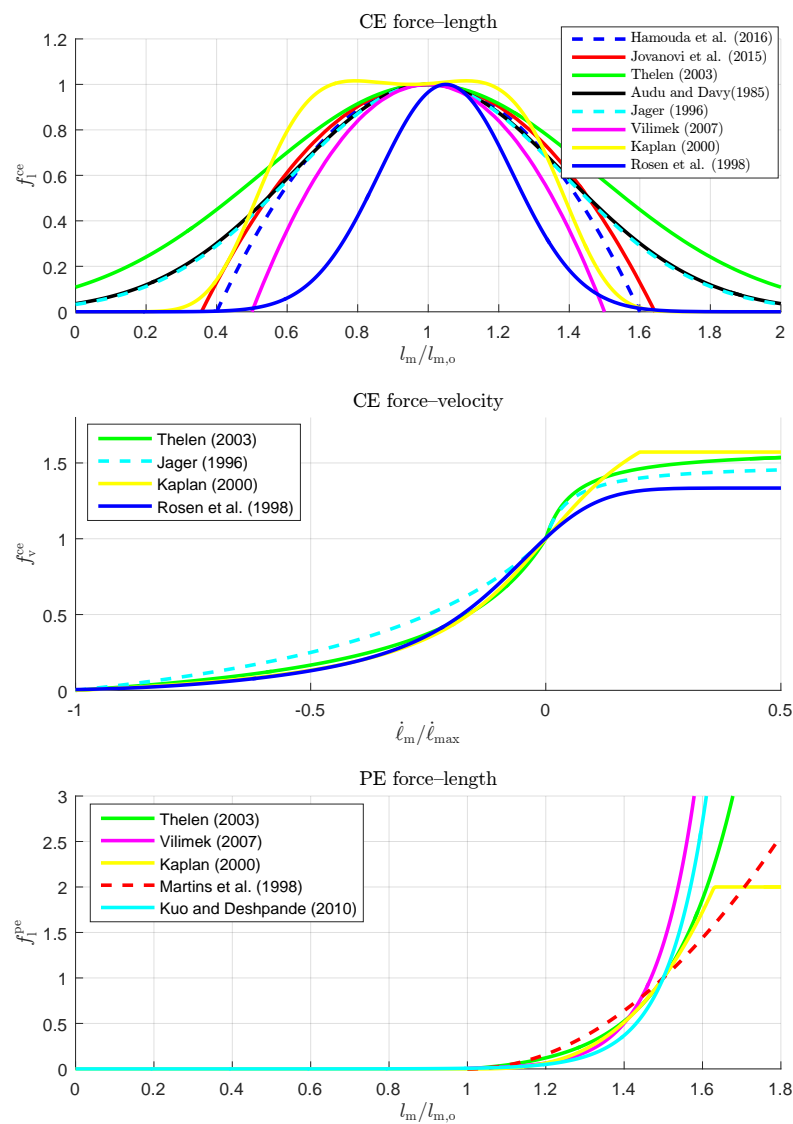


Figure 3.11: Comparison of different formulations of the Hill-type muscle model.

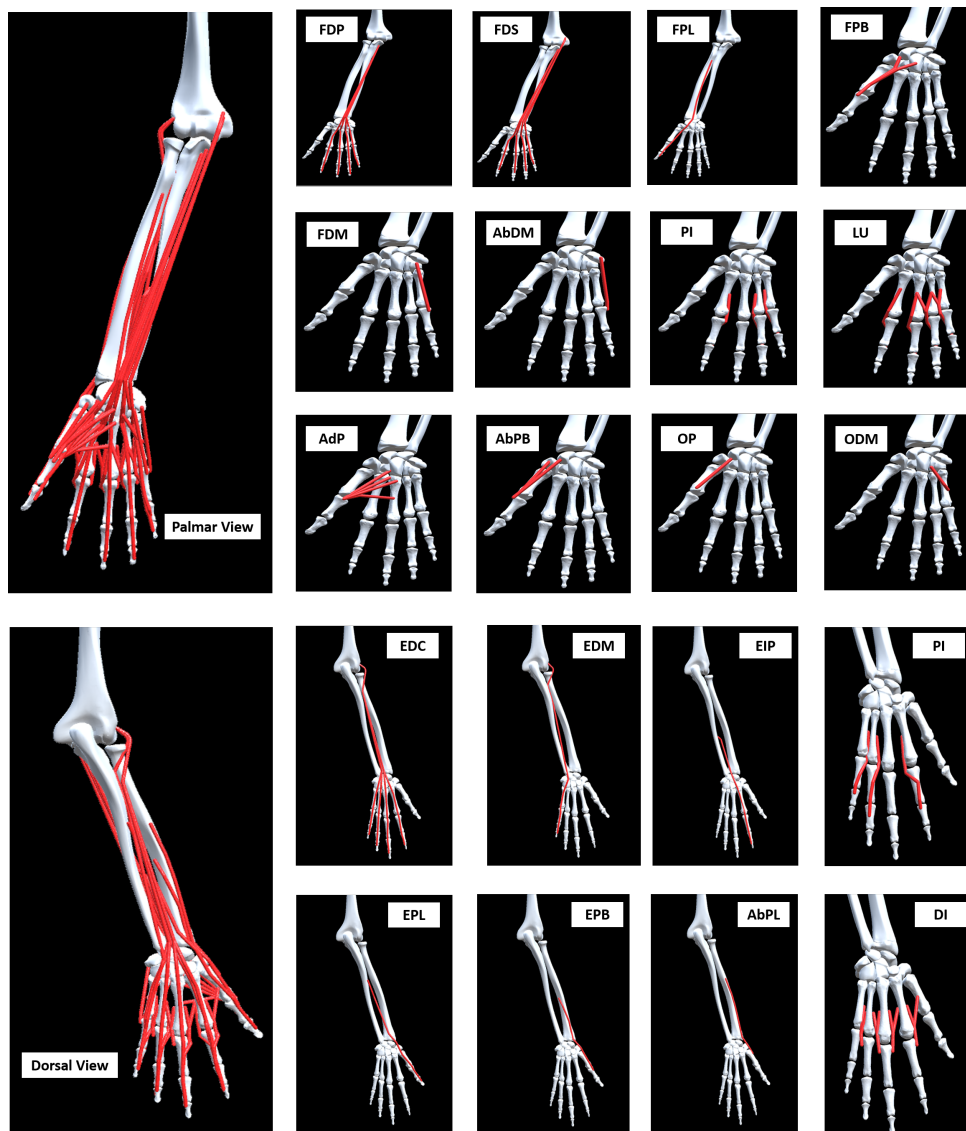


Figure 3.12: Modelled extrinsic and intrinsic hand muscles. Table 3.2 provides muscle descriptions and abbreviations.

Table 3.2: Modelled human hand muscles. The anatomical descriptions of muscles are based on Lippert (2011).

Proposed Model				
Name	Abbreviation	Origin	Insertion	Action
Flexor Digitorum Superficialis	FDS2-FDS5	Common flexor tendon, coronoid process, and radius	Sides of the middle phalanx of the four fingers	Flexes the MCP and PIP joints of the fingers
Flexor Digitorum Profundus	FDP2-FDP5	Upper three-fourths of the ulna	Distal phalanx of the four fingers	Flexes all the three joints of the fingers
Extensor Digitorum (Communis)	EDC2-EDC5	Lateral epicondyle of the humerus	Base of distal phalanx of the four fingers	Extends all the three joints of the fingers
Extensor Indicis (Proprius)	EIP	Distal ulna	Base of distal phalanx of the index finger	Extends all the three joints of the index finger
Dorsal Interossei	DI1-T and DI1-I	First and second metacarpals	Lateral side of the index finger	Abduct the index finger
	DI2-I and DI2-M	Second and third metacarpals	Lateral side of the middle finger	Abduct the middle finger laterally
	DI3-M and DI3-R	Third and fourth metacarpals	Medial side of the middle finger	Abduct the middle finger medially
	DI4-R and DI4-P	Fourth and fifth metacarpals	Medial side of the ring finger	Abduct the ring finger laterally
Palmar Interossei	PI1	Second metacarpals	Medial side of the index finger	Adducts the index finger
	PI2	Fourth metacarpals	Lateral side of the ring finger	Adducts the ring finger
	PI3	Fifth metacarpals	Lateral side of the pinky	Adducts the pinky finger
Lumbricals	LU1	Tendon of FDP2	Tendon of EDC2	Flex the MCP joint while extending the PIP and DIP joints
	LU2	Tendon of FDP3	Tendon of EDC3	
	LU3-M and LU3-R	Tendons of FDP3 and FDP4, respectively	Tendon of EDC4	
	LU4-R and LU4-P	Tendons of FDP4 and FDP5, respectively	Tendon of EDC5	
Extensor Digiti Minimi	EDM	Lateral epicondyle of humerus	Base of distal phalanx of the pinky finger	Extends all the three joints of the pinky finger
Flexor Digiti Minimi	FDM	Hamate and flexor retinaculum	Base of proximal phalanx of the pinky finger	Flexes CMC and MCP joints of the pinky finger
Abductor Digiti Minimi	AbDM	Pisiform and tendon of flexor carpi ulnaris	Proximal phalanx of the pinky finger	Abducts the MCP joints of the pinky finger
Opponens Digiti Minimi	ODM	Hamate and flexor retinaculum	Fifth metacarpal	Opposes the pinky finger
Flexor Pollicis Longus	FPL	Radius, anterior surface	Distal phalanx of the thumb	Flexes all three joints of the thumb
Flexor Pollicis Brevis	FPB1 and FPB2	Trapezium and flexor retinaculum, receptively	Proximal phalanx	Flexes CMC and MCP joints of the thumb
Extensor Pollicis Longus	EPL	Middle posterior ulna and interosseous membrane	Base of distal phalanx of the thumb	Extends all three joints of the thumb
Extensor Pollicis Brevis	EPB	Posterior distal radius	Base of proximal phalanx of the thumb	Extends CMC and MCP joints of the thumb
Abductor Pollicis Longus	AbPL	Posterior radius, interosseous membrane, middle ulna	Base of the first metacarpal	Abducts the thumb
Abductor Pollicis Brevis	AbPB1 and AbPB2	Trapezium, and flexor retinaculum, receptively	Proximal phalanx	Abducts the thumb (CMC joint)
Adductor Pollicis	AdPt, AdPo1-AdPo3	Capitate, base of second metacarpal, and palmar surface of the third metacarpal	Base of proximal phalanx of the thumb	Adducts the thumb (CMC joint)
Opponens Pollicis	OP	Trapezium, and flexor retinaculum	First metacarpal	Opposes the thumb (CMC joint)

3.2 Methodology

3.2.1 Musculotendon kinematic model

A Mathematical model

The proposed model is a complete computational model that takes joint angles and velocity vector as input and estimates the musculotendon lengths, length change rates, and excursion moment arms (Figure 3.13). This model can be divided into four main stages: musculoskeletal model, musculotendon lengths, musculotendon excursion moment arms, and musculotendon length change rates, as summarised in Algorithm 3.1 and explained in the following.

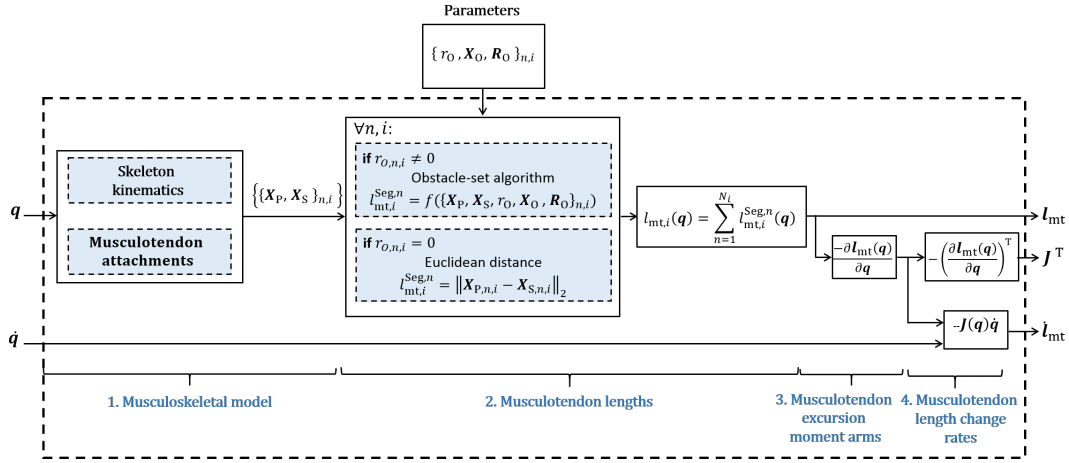


Figure 3.13: Proposed complete musculotendon paths and muscle-joint kinematic model.

Musculoskeletal model

The musculoskeletal model consists of the skeletal kinematic models and the musculotendon attachments. The skeletal kinematic models are used to define the bone-fixed coordinate systems where musculotendon attachment points, via-points, and obstacles are expressed. In order to implement all the intrinsic and extrinsic muscles, the proposed skeletal model in Section 2.2.1 and the skeletal model of Garner and Pandy (1999) are used for the hand and the arm, respectively (Figure 3.14). The DoFs of these models are shown in Table 3.1. Musculotendon paths, which describe the complete muscle route from its origin to its insertion, are implemented for each muscle based on the anatomical descriptions from Lippert (2011) and the human hand dissection description from An et al. (1983). Based on these muscle descriptions, some muscles are modelled with multiple subregions to represent each origin-insertion path when necessary to account for muscles with multiple tendons (e.g. FDS), or multiple heads (e.g. Dorsal Interossei (DI)), or wide attachments (e.g. Adductor Pollicis (AdP)) (Figure 3.12 and Table 3.2).

Algorithm 3.1 Muscle-joint kinematics algorithm

```

1: Parameters:  $\{r_O, \mathbf{X}_O, \mathbf{R}_O\}_{n,i}$  ▷  $r_O \in \mathbb{R}$ : Obstacle radius
2: ▷  $\mathbf{X}_O \in \mathbb{R}^3$ : Cartesian position of the obstacle centre
3: ▷  $\mathbf{R}_O \in \mathbb{R}^3$ : Orthonormal rotation matrix describing the obstacle orientation
4: ▷  $i$ : A musculotendon unit
5: ▷  $n$ : A segment of a musculotendon unit
6: Input:  $\mathbf{q} \in \mathbb{R}^{33 \times 1}, \dot{\mathbf{q}} \in \mathbb{R}^{33 \times 1}$  ▷ Joint angle and velocity vectors (Table 3.1)
7: Output:  $\mathbf{l}_{mt} \in \mathbb{R}^{47 \times 1}$  ▷ Musculotendon length vector
8:  $\mathbf{J}^T \in \mathbb{R}^{33 \times 47}$  ▷ Musculotendon excursion moment arm matrix
9:  $\dot{\mathbf{l}}_{mt} \in \mathbb{R}^{47 \times 1}$  ▷ Musculotendon change length vector
10: Procedure:
11:  $\{\{\mathbf{X}_P, \mathbf{X}_S\}_{n,i}\} := \text{Musculoskeletal\_Model}(\mathbf{q})$ 
12: ▷  $\mathbf{X}_{P/S} \in \mathbb{R}^{3 \times 1}$ : Cartesian position of bounding-fixed points P and S
13: for Musculotendon  $i = 1$  to  $i = I = 47$  do
14:   for Segment  $n = 1$  to  $n = N_i$  do
15:     if  $r_{O,n,i} \neq 0$  then
16:        $l_{mt,i}^{\text{Seg},n} := \text{obstacle\_set\_algorithm}(\{\mathbf{X}_P, \mathbf{X}_S, r_O, \mathbf{X}_O, \mathbf{R}_O\}_{n,i})$ 
17:     else
18:        $\{\mathbf{X}_{P,n,i}, \mathbf{X}_{S,n,i}\} := \{\mathbf{X}_P, \mathbf{X}_S\}_{n,i}$ 
19:        $l_{mt,i}^{\text{Seg},n} := \|\mathbf{X}_{P,n,i} - \mathbf{X}_{S,n,i}\|_2$ 
20:     end if
21:   end for
22:    $l_{mt,i} = \sum_{n=1}^{N_i} l_{mt,i}^{\text{Seg},n}$ 
23: end for
24:  $\mathbf{l}_{mt} := \left( l_{mt,1} \quad l_{mt,2} \quad \cdots \quad l_{mt,I} \right)^T$ 
25:  $\mathbf{J} = -\frac{\partial \mathbf{l}}{\partial \mathbf{q}}$  ▷ Implemented via finite difference (Equation 3.13)
26:  $\mathbf{J}^T = -\left(\frac{\partial \mathbf{l}}{\partial \mathbf{q}}\right)^T$ 
27:  $\dot{\mathbf{l}}_{mt} = -\mathbf{J}\dot{\mathbf{q}}$ 

```

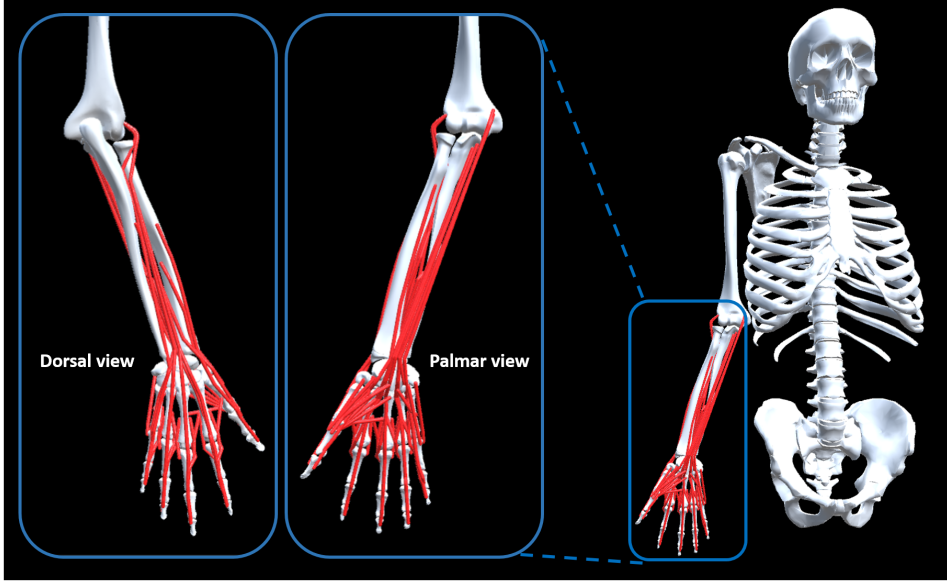


Figure 3.14: Three-dimensional visualisation of the proposed 27 muscles/47 musculotendon path model. The 3-D visualisation is implemented in Unity (Unity Technologies, USA).

Musculotendon lengths

Skeletal muscles that span multiple joints have multiple attachment points besides origin and insertion. These attachment points divide the musculotendon path into different segments, which connect origin, via-points, and insertion (Figure 3.15). For an arbitrary musculotendinous unit i , its length $l_{mt,i}$, which is modelled as a function of joint angles \mathbf{q} and expressed as $l_{mt,i}(\mathbf{q})$, is calculated as a summation of multiple muscle segment lengths. The length $l_{mt,i}(\mathbf{q})$ is defined as

$$l_{mt,i}(\mathbf{q}) = \sum_{n=1}^{N_i} l_{mt,i}^{\text{Seg},n}(\mathbf{q}), \quad (3.1)$$

where N_i denotes the number of muscle segments, and $l_{mt,i}^{\text{Seg},n}(\mathbf{q})$ is the length of the i -th musculotendon's n -th segment.

Each muscle segment is either a straight or curved line (Figure 3.15). The straight line segment spans between two adjacent via-points with the shortest Euclidean distance, while a curved line segment wraps around one or several anatomic structures that constrain the musculotendon path. In the proposed model, certain obstacles (or wrapping surfaces) are used to model these anatomical structures (Figure 3.15). Due to the presence of such obstacles, the via-points can be categorised into two types (Garner and Pandy 2000):

1. *Bounding-fixed via-points* which remain constant in a bone reference frame, see P and S in Figure 3.16. As the musculotendon path always passes through them, these via-points are indicated as *active* via-points.

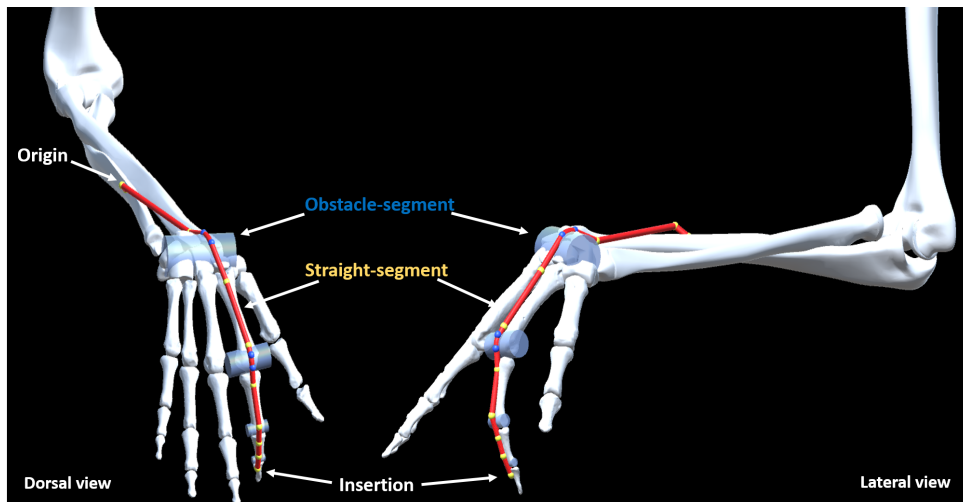


Figure 3.15: The musculotendon path is modelled as multiple segments defined by the attachment points. The yellow spheres represent musculotendon origin, via-points, and insertion. The blue spheres denote obstacle via-points and the light blue cylinders denote modelled obstacles. The 3-D visualisation is implemented in Unity.

2. *Obstacle "active/inactive" via-points* which are constrained to move on the surface of its underlying obstacle and define the beginning or the end of the musculotendon-obstacle contact, see Q and T in Figure 3.16. The existence of obstacle via-points is conditional, depending on whether the musculotendon path wraps the obstacle. Thus, these via-points are either *active*, when the musculotendon path passes through them, or *inactive*, when the musculotendon path does not pass through.

The obstacle-set method is used to calculate the length $l_{mt,i}^{\text{Seg},n}(\mathbf{q})$ in Equation 3.1 in curved line segment. In the proposed model, the single-cylinder obstacle-set algorithm developed by Garner and Pandy (2000) is used. With a cylindrical obstacle and two bounding-fixed via-points (P and S) as an input, this algorithm determines if the obstacle via-points (Q and T) are *active/inactive* using a warping condition and calculates the length of the curved musculotendon path P-Q-T-S or straight musculotendon path P-S (Algorithm 3.2). The parameters required to define the single-cylinder obstacle are the radius r_O , the centre \mathbf{X}_O , and the orientation \mathbf{R}_O of the cylinder in its bone-fixed coordinate systems. The values of these parameters are chosen based on the dimension of the corresponding anatomical structure and the muscles were checked that they do not penetrate bones or joints for joint full range of motion.

Algorithm 3.2 Single-cylinder obstacle-set (Garner and Pandy 2000; Hu 2016)

-
- 1: **Parameters:** $r_O, \mathbf{X}_O, \mathbf{R}_O$ ▷ $r_O \in \mathbb{R}$: Obstacle radius
- 2: ▷ $\mathbf{X}_O \in \mathbb{R}^3$: Cartesian position of the obstacle centre
- 3: ▷ $\mathbf{R}_O \in \mathbb{R}^3$: Orthonormal rotation matrix describing the obstacle orientation
- 4: **Input:** $\left\{ {}^{(W)}\mathbf{X}_P, {}^{(W)}\mathbf{X}_S \right\} := \text{Musculoskeletal_Model}(\mathbf{q})$
- 5: ▷ $\mathbf{X}_{P/S} \in \mathbb{R}^{3 \times 1}$: Cartesian position of bounding-fixed via-points P and S
- 6: **Output:** $\mathbf{X}_Q, \mathbf{X}_T, w_O, l_{PQTS}$
- 7: ▷ $\mathbf{X}_{Q/T} \in \mathbb{R}^{3 \times 1}$: Cartesian position of obstacle via-points Q and T
- 8: ▷ w_O : Wrapping condition
- 9: ▷ l_{PQTS} : musculotendon path length
- 10: **Procedure:**
- 11: $\begin{pmatrix} {}^{(O)}\mathbf{X}_P \\ 1 \end{pmatrix} = {}^O\mathbf{T}_W \begin{pmatrix} {}^{(W)}\mathbf{X}_P \\ 1 \end{pmatrix};$ ▷ Expressing P in {O}
- 12: $\begin{pmatrix} {}^{(O)}\mathbf{X}_S \\ 1 \end{pmatrix} = {}^O\mathbf{T}_W \begin{pmatrix} {}^{(W)}\mathbf{X}_S \\ 1 \end{pmatrix};$ ▷ Expressing S in {O}
- 13: ${}^{(O)}x_Q = \frac{{}^{(O)}x_P r_O^2 + {}^{(O)}y_P r_O \sqrt{{}^{(O)}x_P^2 + {}^{(O)}y_P^2 - r_O^2}}{({}^{(O)}x_P^2 + {}^{(O)}y_P^2)};$ ▷ Computing x -component of Q
- 14: ${}^{(O)}y_Q = \frac{{}^{(O)}y_P r_O^2 - {}^{(O)}x_P r_O \sqrt{{}^{(O)}x_P^2 + {}^{(O)}y_P^2 - r_O^2}}{({}^{(O)}x_P^2 + {}^{(O)}y_P^2)};$ ▷ Computing y -component of Q
- 15: ${}^{(O)}x_T = \frac{{}^{(O)}x_S r_O^2 - {}^{(O)}y_S r_O \sqrt{{}^{(O)}x_S^2 + {}^{(O)}y_S^2 - r_O^2}}{({}^{(O)}x_S^2 + {}^{(O)}y_S^2)};$ ▷ Computing x -component of T
- 16: ${}^{(O)}y_T = \frac{{}^{(O)}y_S r_O^2 + {}^{(O)}x_S r_O \sqrt{{}^{(O)}x_S^2 + {}^{(O)}y_S^2 - r_O^2}}{({}^{(O)}x_S^2 + {}^{(O)}y_S^2)};$ ▷ Computing y -component of T
- 17: $\begin{pmatrix} * \\ * \\ \sin \angle Q'OT' \end{pmatrix} = \frac{{}^{(O)}\mathbf{X}_{Q'} \times {}^{(O)}\mathbf{X}_{T'}}{\|{}^{(O)}\mathbf{X}_{Q'}\|_2 \|{}^{(O)}\mathbf{X}_{T'}\|_2};$ ▷ Computing the sine of the wrapping angle
- 18: **if** $\angle Q'OT' \leq 180^\circ$ **then**
- 19: $w_O = 1;$ ▷ Wrapping condition is *true*
- 20: $\angle QOT = \angle POS - \arccos \frac{|r_O|}{\|{}^{(O)}\mathbf{X}_P\|_2} - \arccos \frac{|r_O|}{\|{}^{(O)}\mathbf{X}_S\|_2};$
- 21: $l_{\widehat{Q'T'}} = |r_O| \angle Q'OT';$ ▷ Computing the length of Q-T segment in the x-y plane of {O}
- 22: ${}^{(O)}z_Q = {}^{(O)}z_P + \frac{({}^{(O)}z_S - {}^{(O)}z_P)l_{P'Q'}}{l_{P'Q'} + l_{\widehat{Q'T'}} + l_{T'S'}};$ ▷ Computing z -component of Q
- 23: ${}^{(O)}z_T = {}^{(O)}z_S - \frac{({}^{(O)}z_S - {}^{(O)}z_P)l_{T'S'}}{l_{P'Q'} + l_{\widehat{Q'T'}} + l_{T'S'}};$ ▷ Computing z -component of T
- 24: $l_{\widehat{QT}} = \sqrt{l_{\widehat{Q'T'}}^2 + ({}^{(O)}z_T - {}^{(O)}z_Q)^2};$ ▷ Computing the length of Q-T segment
- 25: $l_{PQ} = \|{}^{(O)}\mathbf{X}_P - {}^{(O)}\mathbf{X}_Q\|_2;$ ▷ Computing the length of P-Q segment
- 26: $l_{TS} = \|{}^{(O)}\mathbf{X}_T - {}^{(O)}\mathbf{X}_S\|_2;$ ▷ Computing the length of T-S segment
- 27: $l_{PQTS} = l_{PQ} + l_{\widehat{QT}} + l_{TS};$ ▷ Computing the length of musculotendon path P-Q-T-S
- 28: **else**
- 29: $w_O = 0;$ ▷ Wrapping condition is *false*
- 30: $l_{PQTS} = l_{PS} = \|{}^{(O)}\mathbf{X}_P - {}^{(O)}\mathbf{X}_S\|_2;$ ▷ Computing the length of musculotendon path P-S
- 31: **end if**
-

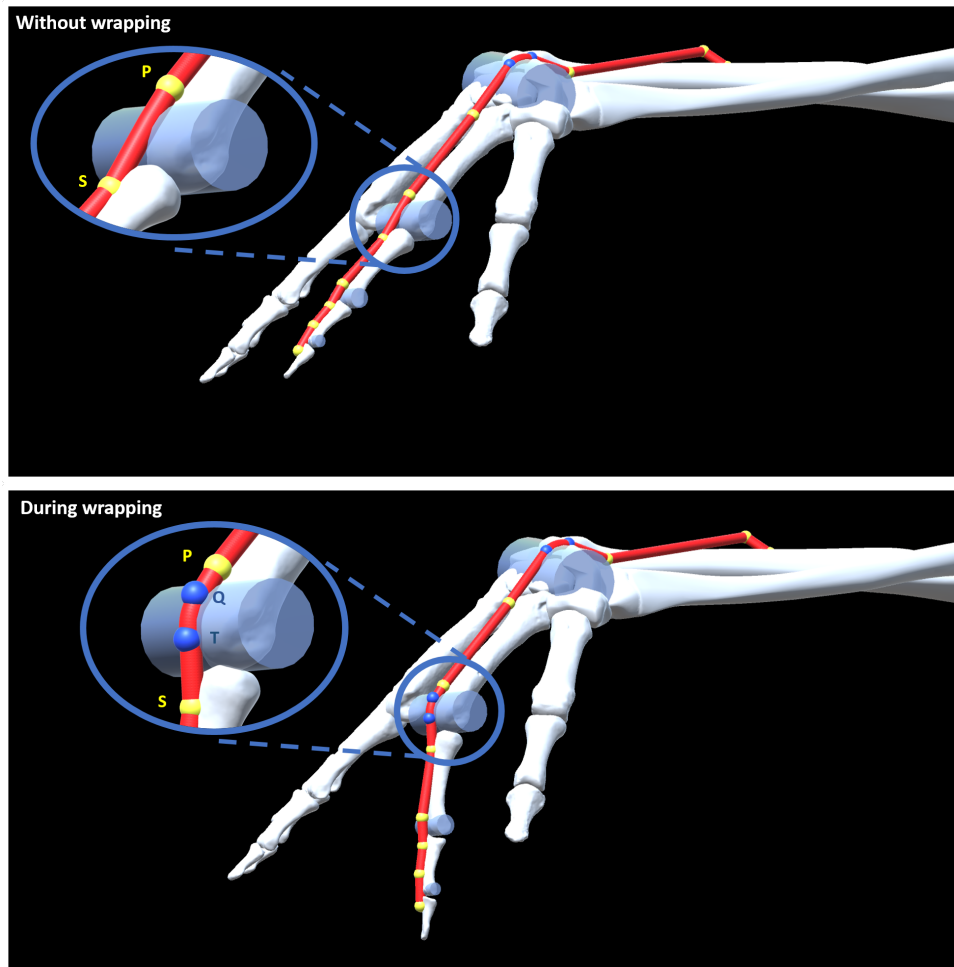


Figure 3.16: Graphical representation of the single-cylinder obstacle-set used in this model at the index metacarpophalangeal (MCP2) joint. Top: when MCP2 is at neutral position, no wrapping occurs and the P-S segment is a straight line. Bottom: when MCP2 is flexed, wrapping occurs where the P-Q and Q-S segments are straight lines and the Q-T segment forms an arc. The 3-D visualisation is implemented in Unity.

The single-cylinder obstacle-set algorithm has four main steps (Figure 3.17). This algorithm is explained in the following based on Garner and Pandy (2000) and Hu (2016).

Step 1: Expressing the positions of the two bounding-fixed via-points, P and S, in the cylinder reference frame $\{O\}$ by transformation from the world reference frame $\{W\}$ via

$$\begin{pmatrix} {}^{(O)}\mathbf{X}_P \\ 1 \end{pmatrix} = {}^O\mathbf{T}_W \begin{pmatrix} {}^{(W)}\mathbf{X}_P \\ 1 \end{pmatrix}, \quad (3.2a)$$

$$\begin{pmatrix} {}^{(O)}\mathbf{X}_S \\ 1 \end{pmatrix} = {}^O\mathbf{T}_W \begin{pmatrix} {}^{(W)}\mathbf{X}_S \\ 1 \end{pmatrix}, \quad (3.2b)$$

where ${}_{(O)}\mathbf{X}_P$ and ${}_{(O)}\mathbf{X}_S$ are the Cartesian positions of P and S expressed in $\{O\}$, respectively, ${}_{(W)}\mathbf{X}_P$ and ${}_{(W)}\mathbf{X}_S$ are the Cartesian positions of P and S expressed in $\{W\}$, respectively, and ${}^O\mathbf{T}_W$ is the transformation matrix from $\{W\}$ to $\{O\}$.

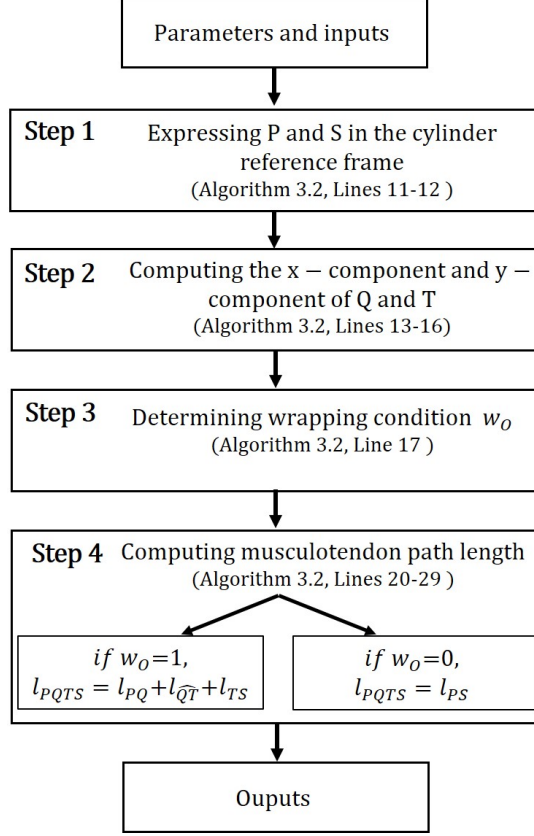


Figure 3.17: Flowchart of the single-cylinder obstacle-set algorithm developed by Garner and Pandy (2000).

Step 2: calculating the positions of the obstacle via-points, Q and T. Considering that the obstacle via-points are located on the surface of an obstacle, the straight line segments are tangential to the obstacle surface, and the cross-section of a cylindrical obstacle is circular, two constraint equations may be derived focusing on the P-Q segment (Figure 3.18), as

$$r_O^2 = {}_{(O)}x_Q^2 + {}_{(O)}y_Q^2, \quad (3.3a)$$

$$r_O^2 + ({}_{(O)}x_P - {}_{(O)}x_Q)^2 + ({}_{(O)}y_P - {}_{(O)}y_Q)^2 = {}_{(O)}x_P^2 + {}_{(O)}y_P^2, \quad (3.3b)$$

where r_O denotes the radius of the cylinder obstacle and can be both positive and negative for the single-cylinder obstacle-set, so that the correct wrapping direction is defined, ${}_{(O)}x_Q$ and ${}_{(O)}y_Q$ are the x -component and y -component of Q expressed in $\{O\}$, respectively, ${}_{(O)}x_P$ and ${}_{(O)}y_P$ are the x -component and y -component of P expressed in

$\{O\}$, respectively. By combining Equation 3.3a and Equation 3.3b, the solution of ${}_{(O)}x_Q$ and ${}_{(O)}y_Q$ is

$${}_{(O)}x_Q = \frac{{}_{(O)}x_P r_O^2 + {}_{(O)}y_P r_O \sqrt{{}_{(O)}x_P^2 + {}_{(O)}y_P^2 - r_O^2}}{({}_{(O)}x_P^2 + {}_{(O)}y_P^2)}, \quad (3.4a)$$

$${}_{(O)}y_Q = \frac{{}_{(O)}y_P r_O^2 - {}_{(O)}x_P r_O \sqrt{{}_{(O)}x_P^2 + {}_{(O)}y_P^2 - r_O^2}}{({}_{(O)}x_P^2 + {}_{(O)}y_P^2)}. \quad (3.4b)$$

Similarly, the x -component and y -component of T expressed in $\{O\}$ are calculated as

$${}_{(O)}x_T = \frac{{}_{(O)}x_S r_O^2 - {}_{(O)}y_S r_O \sqrt{{}_{(O)}x_S^2 + {}_{(O)}y_S^2 - r_O^2}}{({}_{(O)}x_S^2 + {}_{(O)}y_S^2)}, \quad (3.5a)$$

$${}_{(O)}y_T = \frac{{}_{(O)}y_S r_O^2 + {}_{(O)}x_S r_O \sqrt{{}_{(O)}x_S^2 + {}_{(O)}y_S^2 - r_O^2}}{({}_{(O)}x_S^2 + {}_{(O)}y_S^2)}, \quad (3.5b)$$

where ${}_{(O)}x_T$ and ${}_{(O)}y_T$ are the x -component and y -component of T expressed in $\{O\}$, respectively, ${}_{(O)}x_S$ and ${}_{(O)}y_S$ are the x -component and y -component of S expressed in $\{O\}$, respectively.

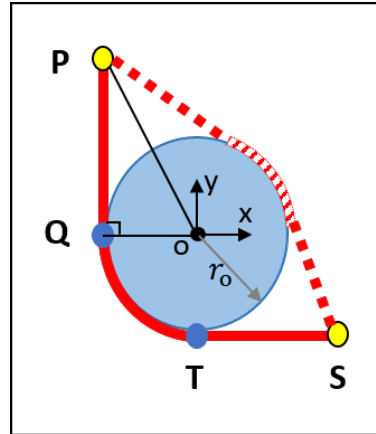


Figure 3.18: Illustration of the obstacle cross-section and the geometric conditions. The full musculotendon path is P-Q-T-S with the straight line segments, P-Q and T-S, being tangents to the obstacle surface. There are two possibilities for wrapping: the right-handed sense (solid line) and the left-handed sense (dashed line). Either wrapping direction can be specified using a signed value to the obstacle radius r_O , i.e. positive and negative values for r_O would correspond to right-handed and left-handed wrapping, respectively.

In the previous steps, the x -components and y -components of Q and T, which are needed to check the wrapping condition in step 4, are calculated. The z -components of Q and T are required to calculate the curved path length if the wrapping occurred, thus they are calculated using Equation 3.11 after checking the wrapping condition.

Step 3: Checking wrapping condition. Wrapping condition w_O is used to determine whether or not, for a given joint configuration, a musculotendon path wraps around an

obstacle. When joint configuration changes, the bounding-fixed via-points, i.e. P and S, move with respect to the obstacle, which results in a changing wrapping condition. The wrapping condition w_O is defined in terms of the angle formed by the arc from Q to T, defined as the wrapping angle $\angle Q'OT'$. The wrapping condition w_O is *true* and Q and T are *active* if $\angle Q'OT'$ is positive and smaller than or equal to 180° . Otherwise w_O is *false* and Q and T are *inactive* (Figure 3.19). Mathematically, w_O is defined as

$$w_O = \begin{cases} 1 & \text{if } r_O \sin \angle Q'OT' \geq 0 \\ 0 & \text{otherwise} \end{cases}, \quad (3.6)$$

where Q' and T' are the projections of Q and T in the x-y plane of $\{O\}$, respectively, and r_O denotes the radius of the cylinder obstacle. Computationally, $\sin \angle Q'OT'$ is calculated via

$$\begin{pmatrix} * \\ * \\ \sin \angle Q'OT' \end{pmatrix} = \frac{{}_O\mathbf{X}_{Q'} \times {}_O\mathbf{X}_{T'}}{\|{}_O\mathbf{X}_{Q'}\|_2 \|{}_O\mathbf{X}_{T'}\|_2}, \quad (3.7)$$

(Hu 2016), where * denotes irrelevant components, ${}_O\mathbf{X}_{Q'}$ and ${}_O\mathbf{X}_{T'}$ are the Cartesian positions of Q and T in the x-y plane of $\{O\}$ as 3-D vectors with the z-components equal to zero.

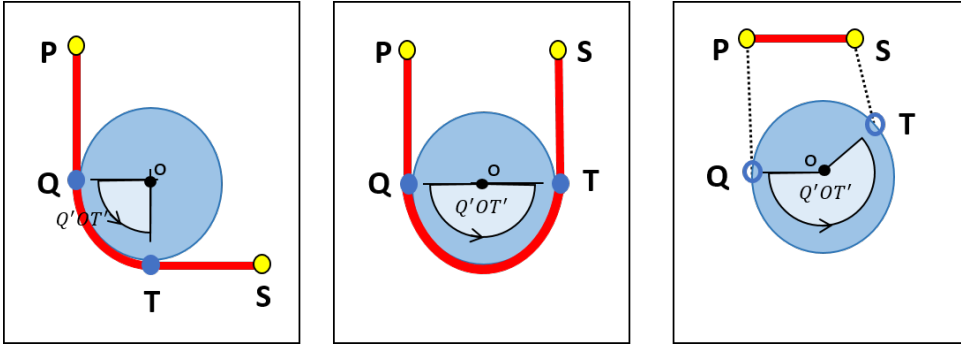


Figure 3.19: Illustration of the wrapping angle, defined as the angle formed by the arc from Q to T $\angle Q'OT'$. The wrapping condition w_O is *true*, i.e. $\angle Q'OT' \leq 180^\circ$, and Q and T are *active* (left and middle). Otherwise w_O is *false* and Q and T are *inactive* (right).

Step 4: Computing the musculotendon path segment lengths. In configurations when w_O is *false*, the obstacle via-points are *inactive* and the musculotendon path does not pass through them. In this case, the resulting musculotendon path P-S is a straight line segment only with a length calculated as

$$l_{PQTS} = l_{PS} = \|{}_O\mathbf{X}_P - {}_O\mathbf{X}_S\|_2, \quad (3.8)$$

where l_{PS} is the length of the straight line segment P-S without obstacle via-points.

In the other case when the w_O is *true*, the obstacle via-points are *active* and the musculotendon path passes through them. The resulting musculotendon path P-Q-T-S has two straight line segments, i.e. P-Q and T-S, and one curved line segment, i.e. Q-T. Thus, the total musculotendon path length l_{PQTS} is calculated as

$$l_{PQTS} = l_{PQ} + l_{\widehat{QT}} + l_{TS}, \quad (3.9)$$

where l_{PQ} and l_{TS} are the lengths of the straight line segments P-Q and T-S, respectively, and $l_{\widehat{QT}}$ is the length of the curved line segment. The lengths l_{PQ} and l_{TS} are calculated using

$$\begin{aligned} l_{PQ} &= \|({}_O)\mathbf{X}_P - ({}_O)\mathbf{X}_Q\|_2, \\ l_{TS} &= \|({}_O)\mathbf{X}_T - ({}_O)\mathbf{X}_S\|_2, \end{aligned} \quad (3.10)$$

where $({}_O)\mathbf{X}_Q$ and $({}_O)\mathbf{X}_T$ are the Cartesian positions of Q and T, respectively.

The x -components and y -components of Q and T are calculated using Equations 3.4–3.5 while the z -components of Q and T are calculated using similar triangle formulas as

$$({}_O)z_Q = ({}_O)z_P + \frac{(({}_O)z_S - ({}_O)z_P)l_{P'Q'}}{l_{P'Q'} + l_{\widehat{Q'T'}} + l_{T'S'}}, \quad (3.11a)$$

$$({}_O)z_T = ({}_O)z_S - \frac{(({}_O)z_S - ({}_O)z_P)l_{T'S'}}{l_{P'Q'} + l_{\widehat{Q'T'}} + l_{T'S'}}, \quad (3.11b)$$

where $({}_O)z_Q$, $({}_O)z_P$, $({}_O)z_S$, and $({}_O)z_T$ are the z -components of Q, P, S, T expressed in $\{O\}$, respectively, $l_{P'Q'}$ and $l_{T'S'}$ are the lengths of P-Q and T-S segments in the x - y plane of $\{O\}$, which are calculated analogously to Equation 3.10 using the projections of Q, P, S, and T on the x - y plane of $\{O\}$.

Finally, the length of the curved line segment $l_{\widehat{QT}}$ is calculated using the x -components, y -components, and z -components of Q and T obtained using Equations 3.4–3.5 and Equation 3.11 as

$$l_{\widehat{QT}} = \|{}_O\mathbf{X}_Q - {}_O\mathbf{X}_T\|_2. \quad (3.12)$$

Musculotendon excursion moment arms

The musculotendon excursion moment arms, which relate the change of musculotendon excursions to the change of joint angles, are commonly known as the transposed joint configuration-dependent muscle-joint Jacobian matrix $\mathbf{J}^T(\mathbf{q})$ according to the principle of virtual work (Hagan 1985; Hogan 1985). Thus, for a system with I musculotendinous units and K joint angles, $\mathbf{J}(\mathbf{q}) \in \mathbb{R}^{I \times K}$ is expressed as

$$\mathbf{J}(\mathbf{q}) = -\frac{\partial \mathbf{l}_{\text{mt}}(\mathbf{q})}{\partial \mathbf{q}} = \begin{bmatrix} -\frac{\partial l_{\text{mt}1}(\mathbf{q})}{\partial q_1} & -\frac{\partial l_{\text{mt}1}(\mathbf{q})}{\partial q_2} & \cdots & -\frac{\partial l_{\text{mt}1}(\mathbf{q})}{\partial q_K} \\ -\frac{\partial l_{\text{mt}2}(\mathbf{q})}{\partial q_1} & -\frac{\partial l_{\text{mt}2}(\mathbf{q})}{\partial q_2} & \cdots & -\frac{\partial l_{\text{mt}2}(\mathbf{q})}{\partial q_K} \\ \vdots & \vdots & \ddots & \vdots \\ -\frac{\partial l_{\text{mt}I}(\mathbf{q})}{\partial q_1} & -\frac{\partial l_{\text{mt}I}(\mathbf{q})}{\partial q_2} & \cdots & -\frac{\partial l_{\text{mt}I}(\mathbf{q})}{\partial q_K} \end{bmatrix}, \quad (3.13)$$

where the negative sign originates from the opposition between musculotendon force and length, i.e. muscle contraction (positive force) results in a shortening in the muscle length (negative length change) (Kühn et al. 2018).

Each column of $\mathbf{J}(\mathbf{q})$ represents the single-angle muscle moment arms about the k -th joint angle. Thus the vector of muscle moment arms about the k -th joint angle \mathbf{j}_k can be rewritten as

$$\mathbf{j}_k(\mathbf{q}) = -\frac{\partial \mathbf{l}_{\text{mt}}(\mathbf{q})}{\partial q_k} = \begin{pmatrix} -\frac{\partial l_{\text{mt}1}(\mathbf{q})}{\partial q_k} \\ -\frac{\partial l_{\text{mt}2}(\mathbf{q})}{\partial q_k} \\ \vdots \\ -\frac{\partial l_{\text{mt}I}(\mathbf{q})}{\partial q_k} \end{pmatrix}, \quad (3.14)$$

where q_k denotes the k -th joint angle. The partial derivatives in Equation 3.14 may be approximated by their forward differences (Sherman et al. 2013; Jäntschi 2014) as

$$-\frac{\partial \mathbf{l}_{\text{mt}}(\mathbf{q})}{\partial q_k} \approx \frac{\mathbf{l}_{\text{mt}}(q_1, \dots, q_k + \delta, \dots, q_K) - \mathbf{l}_{\text{mt}}(q_1, \dots, q_k, \dots, q_K)}{\delta}, \quad (3.15)$$

where $\delta = 10^{-5}$ rad, and the numerator is calculated using Equation 3.1.

Musculotendon length change rates

The musculotendon length change rate $\dot{\mathbf{l}}_{\text{mt}}(\mathbf{q}, \dot{\mathbf{q}})$ is calculated as

$$\dot{\mathbf{l}}_{\text{mt}}(\mathbf{q}, \dot{\mathbf{q}}) = -\mathbf{J}(\mathbf{q})\dot{\mathbf{q}}, \quad (3.16)$$

where $\mathbf{J}(\mathbf{q})$ is calculated using Equation 3.13.

B Computational model

The proposed mathematical model of the muscle-joint kinematics was implemented in the MATLAB® SimMechanics™ Toolbox (The MathWorks, Inc., USA). SimMechanics™ is a set of block libraries and simulation tools for modelling physical systems in the MATLAB® Simulink® Toolbox. It runs within the Simulink® environment and interfaces seamlessly with the rest of Simulink® and MATLAB®. Unlike other Simulink® blocks, which represent mathematical operations or operate on signals, SimMechanics™ blocks represent physical components or relationships directly. It simulates translational and ro-

tational motion in three dimensions of rigid bodies connected by joints, with the standard Newtonian dynamics of forces and torques. With SimMechanicsTM, mechanical systems are modelled and simulated with a suite of tools to specify bodies, their mass properties, possible motions, kinematic constraints, and coordinate systems; as well as to initiate and measure body motions.

The proposed muscle-joint kinematic model is implemented as rigid bodies (representing the bones) connected with joints (representing translational and rotational DoFs). Musculotendon attachments and obstacle-sets are defined in the corresponding rigid body coordinate systems. Using SimMechanicsTM body sensor, the positions of these via-points are measured, which are used to calculate $l_{mt,i}^{\text{Seg},n}(\mathbf{q})$ and consequently $\mathbf{l}_{mt}(\mathbf{q})$, $\dot{\mathbf{l}}_{mt}(\mathbf{q}, \dot{\mathbf{q}})$, and $\mathbf{J}^T(\mathbf{q})$ for a given joint configuration.

C Model validation

Limited cadaver data are available in the literature for moment arms with respect to joint variations. To validate the proposed model, a thorough simulation was performed and results are compared with previous experimental data from An et al. (1983) and Smutz et al. (1998), which are widely used in biomechanical model validations (Chang and Matsuoka 2006; Deshpande et al. 2008; Wu et al. 2009b; Deshpande et al. 2010; Wohlman and Murray 2013; Lee et al. 2015). The moment arms of all extrinsic and intrinsic hand muscles were computed for the 26 DoFs hand model represented in Figure 2.3; however, the comparison presented in the results (Section 3.3.1) is limited to the available experimental data (An et al. 1983; Smutz et al. 1998). The index finger muscles are validated for the metacarpophalangeal joint (MCP2) abduction/adduction (Ab/Ad) and flexion/extension (F/E) over a range of motion of $[0\ 50]^\circ$ and $[0\ 90]^\circ$, respectively. The thumb muscles are validated for carpometacarpal joint (CMC1) and MCP1 Ab/Ad and F/E and interphalangeal joint (IP) F/E over a range of motion of $[-20\ 20]^\circ$, $[-20\ 20]^\circ$, $[-10\ 10]^\circ$, $[0\ 60]^\circ$, and $[-10\ 60]^\circ$, respectively. These ranges of motion were chosen based on those of previously published experimental data (An et al. 1983; Smutz et al. 1998) and simulated using sinusoidal functions as

$$\begin{aligned}
 q_1 &= 20^\circ \sin(2t), \\
 q_2 &= 10^\circ \sin(2t), \\
 q_3 &= 20^\circ \sin(2t), \\
 q_4 &= 30^\circ \sin(2t) + 30^\circ, \\
 q_5 &= 35^\circ \sin(2t) + 25^\circ, \\
 q_7 &= 25^\circ \sin(2t) + 25^\circ, \\
 q_8 &= 45^\circ \sin(2t) + 45^\circ,
 \end{aligned} \tag{3.17}$$

where q_1, \dots, q_5 indicate CMC1 Ab/Ad, CMC1 F/E, MCP1 Ab/Ad, MCP1 F/E, and IP F/E, respectively, q_7 indicates MCP2 Ab/Ad, and q_8 indicates MCP2 F/E.

In order to consider the individual anthropometric differences when assessing the correctness of the model, the curve pattern of the moment arm-joint angle diagram shall be compared with the available cadaver measurements rather than the absolute moment arm magnitude values. To evaluate this pattern, an expressive coefficient of similarity is required. This similarity coefficient should indicate the correlation between two datasets with high variance, and be able to assess the similarity between two datasets with even almost constant values.

For lack of suitable existing metrics, a similarity coefficient s has been defined by Tingli Hu in Ma'touq et al. (2019) as

$$s = 1 - (1 - \rho) \sqrt{\frac{\sigma_1}{|\mu_1| + \sigma_1} \frac{\sigma_2}{|\mu_2| + \sigma_2}} \in [-1, +1], \quad (3.18)$$

$$c_{1,2} = \frac{\sigma_1}{|\mu_1| + \sigma_1} \frac{\sigma_2}{|\mu_2| + \sigma_2},$$

inspired by the Pearson's correlation coefficient, where ρ is Pearson's correlation coefficient between the moment arm magnitude values of the proposed model and the cadaver measurements from literature, μ_1 , σ_1 and μ_2 , σ_2 are the arithmetic means and standard deviations of the modelled and measured moment arm magnitude values over joint angle, respectively, and $c_{1,2}$ is the normalised covariance of the model and measured moment arm magnitude values over joint angle. The proposed similarity coefficient extends the Pearson's correlation coefficient to be applicable to datasets with low variance. For low-variance dataset ($c_{1,2} \rightarrow +0$), s approaches 1, indicating high similarity, while for high-variance datasets ($c_{1,2} \rightarrow +1$), s approaches ρ . Since the proposed similarity coefficient scales the Pearson's correlation coefficient, the characteristic values and their interpretation of Pearson's correlation coefficient can be applied (Hinkle et al. 2003), i.e.

- $s \in [-1, 0)$ for *no similarity*
- $s \in [0, 0.3)$ for *little similarity*
- $s \in [0.3, 0.5)$ for *low similarity*
- $s \in [0.5, 0.7)$ for *moderate similarity*
- $s \in [0.7, 0.9)$ for *high similarity*
- $s \in [0.9, 1.0]$ for *very high similarity*

3.2.2 Musculotendon dynamic model

A Mathematical model

The dynamic behaviour of the musculotendon unit is described using a Hill-type muscle model. Two assumptions are made to simplify the Hill-type muscle model used in this thesis (Figure 3.20). These assumptions are:

1. The pennation angle α_m is considered negligible. This angle is one of the muscle architecture parameters that affects muscle force-generating characteristics and is derived from dissection studies (cadaver studies). It has little effect if it is less than 20° (Zajac 1989; Lemay and Crago 1996; Garner and Pandy 2003), which is the case in the index finger muscles (Table 3.3), and can be treated as a constant in the passive joint torque model (Kuo and Deshpande 2012). Thus, α_m is neglected in this model for simplicity.
2. The CE and PE are modelled with respect to all their properties while the SE is assumed to be rigid (Millard et al. 2013; Hu 2015). Thus, with assuming $\alpha_m = 0$, the muscle length l_m and its shortening/lengthening velocity \dot{l}_m are defined as

$$l_m = l_{mt} - l_{t,o}, \quad (3.19a)$$

$$\dot{l}_m = \dot{l}_{mt}, \quad (3.19b)$$

(Hu 2016), where $l_{t,o}$ is the tendon slack length, which is equal to the SE length and calculated in Sub-section B Model parameters.

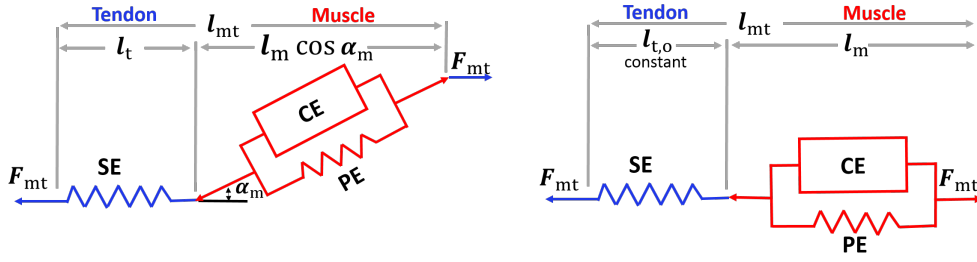


Figure 3.20: The representation of a Hill-type muscle model (left) versus the simplified Hill-type muscle model used in this thesis (right). The simplified model considers the tendon rigid with $l_{t,o} = \text{constant}$ and the pennation angle α_m is zero.

The musculotendon force F_{mt} is the summation of the forces generated by the CE and the PE. The force generated by the CE F_{ce} has both force-length and force-velocity characteristics, i.e. f_l^{ce} and f_v^{ce} , which depend on the length $l_m(q)$, the muscle activation u , and the shortening/lengthening velocity $\dot{l}_m(q)$. On the other hand, the force generated by the PE F_{pe} has force-length characteristic f_l^{pe} that depends on the length $l_m(q)$. Thus, the total musculotendon force produced by the eight muscles of the index finger $F_{mt} \in \mathbb{R}^8$ is given by

$$\begin{aligned} F_{mt}(u, l_{mt}, \dot{l}_{mt}) &= F_{ce}(u, l_m, \dot{l}_m) + F_{pe}(l_m), \\ &= F_{\max} u f_l^{ce}(l_m) f_v^{ce}(u, \dot{l}_m) + F_{\max} f_l^{pe}(l_m), \\ &= F_{\max} \left(u f_l^{ce}(l_m) f_v^{ce}(u, \dot{l}_m) + f_l^{pe}(l_m) \right), \end{aligned} \quad (3.20)$$

Table 3.3: Index finger muscles pennation angle α_m [°]

Study	FDS2	FDP2	EDC2	EIP	DI1	PI1	LU1	Method/Reference
Lieber et al. (1992)	6	7	3	6				Cadaver study
Jacobson et al. (1992)					9.2	6.3	1.2	Cadaver study
Holzbaaur et al. (2005)	6	7	3	6				Lieber et al. (1992)
Wu et al. (2008)	3.1	12.1	3.5	3.5	9.2	9.2	1.2	Based on Lieber et al. (1990), Lieber et al. (1992), and Jacobson et al. (1992)
Kuo and Deshpande (2012)	6	7	3	6	9.2	6.3	1.2	Lieber et al. (1992) and Jacobson et al. (1992)
Lee (2014)	6	7	3	6	9.2	6.3	1.2	Lieber et al. (1992) and Jacobson et al. (1992)
Mirakhorlo et al. (2016)	16 12	10	0	0	15 40	0		Cadaver study

where the muscle length l_m and its shortening/lengthening velocity \dot{l}_m are defined in Equation 3.19, F_{\max} is the maximum voluntary isometric contraction force, and F_{mt} , l_{mt} , \dot{l}_{mt} , F_{ce} , F_{pe} , F_{\max} , f_1^{ce} , f_v^{ce} , f_1^{pe} , u , l_m , and $\dot{l}_m \in \mathbb{R}^8$.

For a *single* musculotendon unit, the musculotendon force is calculated as

$$\begin{aligned}
 F_{mt}(u, l_{mt}, \dot{l}_{mt}) &= F_{ce}(u, l_m, \dot{l}_m) + F_{pe}(l_m), \\
 &= F_{\max} u f_1^{ce}(l_m) f_v^{ce}(u, \dot{l}_m) + F_{\max} f_1^{pe}(l_m), \\
 &= F_{\max} \left(u f_1^{ce}(l_m) f_v^{ce}(u, \dot{l}_m) + f_1^{pe}(l_m) \right),
 \end{aligned} \tag{3.21}$$

(Lloyd and Besier 2003; Buchanan et al. 2004). The components of Equation 3.21 are calculated as follows.

The maximum voluntary isometric contraction force F_{\max} is proportional to the physiological cross-sectional area PCSA and calculated as

$$F_{\max} = S \cdot \text{PCSA}, \tag{3.22}$$

(Zajac 1989; Lieber et al. 1992; Garner and Pandy 2003; Buchanan et al. 2004; Lee 2014; Holzbaaur et al. 2005; Wu et al. 2008), where the constant S represents the maximum muscle stress and ranges from 22 to 137 N.cm⁻² (Spector et al. 1980; Wickiewicz et al. 1984; Buchanan et al. 2004; Lee 2014; Garner and Pandy 2003; Weijis and Hillen 1985; Holzbaaur et al. 2005).

The force-length relation of the CE f_1^{ce} is modelled as a piecewise linear function based on the normalised force-length relationship (Rassier et al. 1999; Garner and Pandy 2003) with the ascending and descending parts as a sigmoid function. The f_1^{ce} is calculated as

$$f_1^{ce}(l_m) = \begin{cases} \frac{0.7}{1+\exp(-23.3(\tilde{l}_m-0.545))} & \tilde{l}_m < 0.545 \\ 4.436 \tilde{l}_m - 2.0674 & \text{if } 0.545 \leq \tilde{l}_m < 0.625 \\ 0.8697 \tilde{l}_m + 0.1574 & \text{if } 0.625 \leq \tilde{l}_m < 0.969 \\ 1 & \text{if } 0.969 \leq \tilde{l}_m < 1.032 \\ -1.9056 \tilde{l}_m + 2.965 & \text{if } 1.032 \leq \tilde{l}_m < 1.4 \\ 0.6 - \frac{0.6}{1+\exp(-12(\tilde{l}_m-1.40))} & \text{otherwise,} \end{cases} \quad (3.23)$$

(Hu 2016), and the normalised muscle length \tilde{l}_m is defined as

$$\tilde{l}_m = \frac{l_m}{l_{m,o}}, \quad (3.24)$$

where $l_{m,o}$ is the optimal muscle length, which represents the optimal resting length for producing the maximal tension, i.e. the actin-myosin overlap reaches the maximum (Figure 3.3).

The force-velocity relation of the CE f_v^{ce} is modelled as

$$f_v^{ce}(u, \dot{l}_m) = \frac{0.1433}{0.1074 + \exp\left(-1.3 \sinh\left(2.8 \frac{\dot{l}_m}{\dot{l}_{\max}(u)} + 1.64\right)\right)}, \quad (3.25)$$

(Winters 1990; Cavallaro et al. 2005), where \dot{l}_{\max} is the maximum contraction velocity above which the muscle cannot produce force (Zajac 1989) and calculated as

$$\dot{l}_{\max}(u) = \frac{5}{2}(u+1)l_{m,o}, \quad (3.26)$$

(Hu 2016).

The force-length relation of the PE f_1^{pe} is modelled as

$$f_1^{pe}(l_m) = \begin{cases} \frac{\exp\left(\frac{k_{pe}}{\varepsilon_{m,o}}\left(\frac{l_m}{l_{m,o}}-1\right)\right)-1}{\exp(k_{pe})-1} & \text{if } \tilde{l}_m \geq 1, \\ 0 & \text{if } \tilde{l}_m < 1 \end{cases}, \quad (3.27)$$

(Winters and Stark 1988; Winters 1995; Thelen 2003; Hu 2015; Hu 2016), where \tilde{l}_m is the normalised muscle length (Equation 3.24), k_{pe} is the shape parameter, which equals 3 (Winters and Stark 1988; Romero and Alonso 2016) or 5 (Thelen 2003), and $\varepsilon_{m,o}$ is the passive muscle strain due to maximum isometric force, which equals 0.5 (Thelen 2003; Hu 2015; Romero and Alonso 2016) or 0.6 (Winters 1995; Thelen 2003; Hu 2016).

These values were chosen by testing different combinations such that the resulting F_{pe} and $\tau_{mt,pe}$ are comparable to values from the literature (Kuo and Deshpande 2010).

B Model parameters

The muscle force-generating characteristics are determined using the proposed Hill-type muscle model (Equation 3.20), which requires three muscle parameters: F_{max} , $l_{m,o}$, and $l_{t,o}$. These parameters are related to muscle architecture and derived mainly from dissection studies (cadaver studies) (Amis et al. 1979; Brand et al. 1981; Lieber et al. 1992; Jacobson et al. 1992; Ward et al. 2006; Sharma et al. 2009; Mirakhorlo et al. 2016), or mathematically as in Garner and Pandy (2003). The parameter values of the index finger muscles appearing in the literature vary widely for even the same muscle (Table 3.4). In the proposed model, the physiological cross-sectional area PCSA, which is required to calculate F_{max} (Equation 3.22), was chosen based on the cadaver studies of Lieber et al. (1992) and Jacobson et al. (1992). These studies are consistent in their experimental protocol and provide the parameters of all extrinsic and intrinsic index finger muscles. The second parameter, i.e. the optimal muscle length $l_{m,o}$, was also adopted from the literature based on Holzbaaur et al. (2005), Lee (2014), and Kuo and Deshpande (2010). Finally, the third parameter, i.e. tendon slack length $l_{t,o}$, is not directly measurable and can be selected to match operating lengths when available (Murray et al. 2000), or to match muscle active and passive moment torque measurements (Holzbaaur et al. 2005). Thus, the tendon slack length $l_{t,o}$ is calculated while considering that the normalised muscle length is equal to one in resting posture (Equation 3.28), and the overall physiological muscle length ranges between $0.5l_{m,o}$ and $1.7l_{m,o}$ (Figure 3.21 and Equation 3.29). Based on that, $l_{t,o}$ was calculated for each muscle by solving

$$l_m/l_{m,o} = \frac{l_{mt} - l_{t,o}}{l_{m,o}} = 1, \quad (3.28)$$

where l_{mt} was calculated using the musculotendon kinematic model in Section 3.2.1 for a simulated resting posture as an input. After that, the resulting $l_{t,o}$ was used to check that for each muscle,

$$0.5 \leq \frac{l_{mt} - l_{t,o}}{l_{m,o}} \leq 1.7, \quad (3.29)$$

where l_{mt} was calculated using the musculotendon kinematic model in Section 3.2.1 for sinusoidal functions that simulate the joint full range of motion as an input. For index finger joints, the flexion/extension RoM is $[-10 \ 90]^\circ$, $[0 \ 110]^\circ$, $[0 \ 80]^\circ$ for MCP joint, PIP joint, and DIP joint, respectively. These RoM are based on Kapandji (2007), Cobos et al. (2010), and Deshpande et al. (2010).

Table 3.4: The state-of-the-art of muscle modelling parameters.

Study	Muscle							Method/Reference
	FDS2	FDP2	EDC2	EIP	DI1	PI1	LU1	
$PCSA [mm^2]$								
Amis et al. (1979)	620	343	94					Cadaver study
Lieber et al. (1992)	171	177	52	56				Cadaver study
Jacobson et al. (1992)					150	75	11	Cadaver study
Holzbaur et al. (2005)	140	150	40	50				Lieber et al. (1992)
Ward et al. (2006)	217	174						Cadaver study
Wu et al. (2008)	479	479	139	112	353	280	28	Brand and Hollister (1999)
Vignais and Marin (2014)	171	177	52	56	150	75	11	Lieber et al. (1992) and Jacobson et al. (1992)
Lee (2014)	140	150	40		150	80	10	Holzbaur et al. (2005) and Brand and Hollister (1999)
Mirakhorlo et al. (2016)	183	138.5	48.9	61	62.1	51.7	7.2	Cadaver study
$l_{m,o} [mm]$								
Amis et al. (1979)	32	57	55					Cadaver study
Lieber et al. (1992)	68	61	57	48				Cadaver study
Jacobson et al. (1992)					38.9	30.7	68	Cadaver study
Holzbaur et al. (2005)	84	75	70	59				Lieber et al. (1992)
Ward et al. (2006)	96.4	94.7						Cadaver study
Wu et al. (2008)	70	66	60	60	14	15	66	Brand and Hollister (1999)
Kuo and Deshpande (2010)	83.5	74.9	70	58.9	61.9	55.1	64.9	Derived from Lieber et al. (1992) and Jacobson et al. (1992)
Kuo and Deshpande (2012)	72.7	67.2	61.9	52.1	38.9	30.7	68	Lieber et al. (1992), Holzbaur et al. (2005), Wu et al. (2008), and Jacobson et al. (1992)
Lee (2014)	84	75	70		32	25	55	Holzbaur et al. (2005) and Brand and Hollister (1999)
Mirakhorlo et al. (2016)	52.1 34.9	90.9	42.6	45	39.6 19.6	25.6	78.4	Cadaver study
$l_{t,o} [mm]$								
Holzbaur et al. (2005)	275	294	322	186				Operating length Murray et al. (2000) and moment measurements
Ward et al. (2006)	229	292.6						Cadaver study
Kuo and Deshpande (2010)	338	322	385	248.04	31.7	25	55.4	Derived from Lieber et al. (1992) and Jacobson et al. (1992)
Kuo and Deshpande (2012)	247.5	265.2	289.9	167.7	31.7	25	55.4	Lieber et al. (1992), Holzbaur et al. (2005), Wu et al. (2008), and Jacobson et al. (1992)
Lee (2014)	275	294	322		296	249	228	Holzbaur et al. (2005) and Garner and Pandy (2003)
Mirakhorlo et al. (2016)	215	260	153	206	10.5 21.5	25		Cadaver study

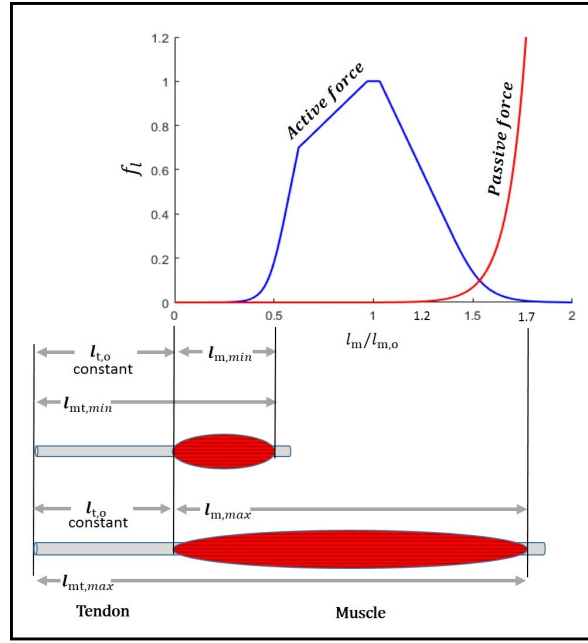


Figure 3.21: Illustration of the physiological muscle length. The effective operating range of a muscle to produce an active force is roughly between $0.5l_{m,o}$ and $1.5l_{m,o}$. A passive force is generated when a muscle is stretched between $1.2l_{m,o}$ and $1.7l_{m,o}$. Thus, the overall physiological muscle length ranges between $0.5l_{m,o}$ and $1.7l_{m,o}$.

C Muscle activation estimation

The force of the musculotendon unit \mathbf{F}_{mt} is calculated by adding \mathbf{F}_{ce} and \mathbf{F}_{pe} (Equation 3.21). As \mathbf{F}_{pe} depends only on $l_m(\mathbf{q})$, which is one output of the kinematic model, it can be directly calculated using Equation 3.27. The process of calculating \mathbf{F}_{ce} is not as straight forward as the \mathbf{F}_{pe} calculation. In order to calculate \mathbf{F}_{ce} , \mathbf{u} is needed alongside $\dot{l}_m(\mathbf{q})$ and $l_m(\mathbf{q})$. One option to calculate \mathbf{F}_{ce} is to solve

$$\boldsymbol{\tau} = \mathbf{J}^T(\mathbf{F}_{ce} + \mathbf{F}_{pe}). \quad (3.30)$$

As the system in Equation 3.30 is an underdetermined system (the number of muscles is greater than the number of joints), it is not simply invertible. This system redundancy results in an infinite number of solutions for muscle forces and joint reactions in each position (Collins 1995). Several optimisation approaches have been applied to solve this problem and estimate muscle forces (An et al. 1984; Anderson and Pandy 2001; Anderson and Pandy 2002; Collins 1995; Crowninshield and Brand 1981; Dul et al. 1984; Kaufman et al. 1991; Pedotti et al. 1978; Thelen et al. 2003; Thelen and Anderson 2006).

Static optimisation, which is applied in this thesis, is computationally efficient, allows full 3-D motion, and generally incorporates many muscles, e.g. 30 or more muscles per leg in gait studies (Anderson and Pandy 2001). It calculates muscle forces at each instant of the simulation time to minimise certain objective function and fulfil specific

constraints (Ackermann and Schiehlen 2009). In biomechanical analysis, the objective functions are used to model some physiological criteria optimised by the nervous system during a specific activity (Ackermann and Schiehlen 2009). They are implemented with the assumption that the human body applies muscle forces with criteria like minimum muscle activations or minimum muscle forces.

In the proposed model, the optimisation problem is formulated as: "*find a musculotendon force F_{mt} , while minimising the sum of squared muscle activation u^2 , to satisfy the joint torque τ at each joint*". Mathematically this optimisation problem is written as

$$\begin{aligned} & \text{minimise} && \sum_{i=1}^8 u_i^2, \\ & \text{subject to} && |\tau - \tau_{mt}| = 0, \end{aligned} \quad (3.31)$$

(Crowninshield and Brand 1981; Kaufman et al. 1991; Anderson and Pandy 2001), where i indicates the number of the musculotendon units passing through the joint, τ is the joint torques, and τ_{mt} is the musculotendon unit torque.

Muscle activation estimation is performed by taking angular position, velocity, and acceleration q, \dot{q}, \ddot{q} of a specific motion as input to the skeletal dynamic model and the musculotendon kinematic model (Figure 3.22). The output of the musculotendon kinematic model is used to calculate the musculotendon force F_{mt} and, together with the moment arms $J^T(q)$, the torque τ_{mt} . The torque resulting from the skeletal dynamic model τ and τ_{mt} are fed into the optimisation model to estimate u (Equation 3.31). This optimisation problem is performed off-line using the `fmincon` function from the MATLAB[®] Optimization Toolbox[™] (The MathWorks, Inc., USA).

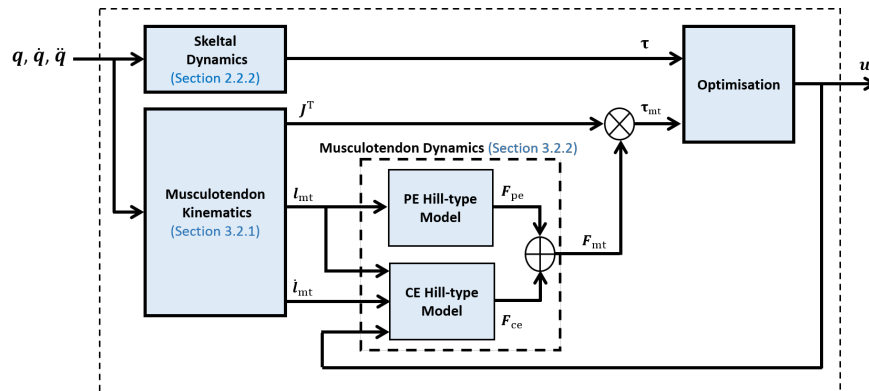


Figure 3.22: Block diagram of the proposed muscle activation model.

D Model validation

The proposed musculotendon dynamic model is validated by:

1. Comparing the resulting $l_m/l_{m,o}$ with the physiological operating range of the muscle, i.e. between 0.5 and 1.7, for joint full RoM. This validate the selected $l_{m,o}$ and calculated $l_{t,o}$.
2. Comparing the modelled F_{pe} and $\tau_{mt,pe}$ with values from the literature (Kuo and Deshpande 2012). The optimal approach would be to compare the musculotendon torque τ_{mt} resulting from the modelled musculotendon force F_{mt} with the measured one. However, the activation u is needed to calculate F_{ce} , which is required to calculate F_{mt} (Equation 3.21). As it is not possible to measure u for intrinsic muscles non-invasively, the model is validated by comparing the modelled F_{pe} and $\tau_{mt,pe}$ to values from the literature instead of F_{mt} and τ_{mt} .

3.3 Results and discussion

3.3.1 Musculotendon kinematic model

A high similarity ($s \geq 0.70$ for 92% of cases) and sign matching can be noticed between the modelled and measured moment arms (Figures 3.23–3.25). This sign matching indicates that the modelled musculotendon shortening/lengthening is correct and thus the musculotendon length change rate $\dot{l}(q, \dot{q})$ is also in the feasible domain. These results indicate the correctness of the proposed moment-arm model and imply that the musculotendon paths, lengths, and length change rates of the proposed musculotendon kinematic model are feasible. However, some differences still exist, which are discussed in the following paragraphs.

For the abduction/adduction (Ab/Ad) DoF of the index metacarpalphalangeal joint (MCP2), high similarity ($s \geq 0.96$) is noticed in all muscles except in the extensor digitorum communis muscle (EDC2) (Figure 3.23). While the literature data of the EDC2 muscle show abduction moment arm, i.e. negative value, the modelled one shows adduction moment arm, i.e. positive value, for the range of motion $\geq 20^\circ$. However, in the same literature, the adduction moment arm of the EDC2 was also reported in some cadaver specimens (two out of seven) (An et al. 1983). For the flexion/extension (F/E) DoF, a very high similarity ($s = 1.00$) between the modelled and measured moment arms is noticed for all extrinsic muscles (Figure 3.23). For the same DoF, the intrinsic muscles show a high similarity between the modelled and measured moment arms with $s \geq 0.75$.

All extrinsic thumb muscles show a very high similarity ($s \geq 0.90$) between the measured and modelled moment arms for the F/E of the CMC, the MCP, and the IP, while the intrinsic muscles show a high similarity with $s \geq 0.71$ (Figures 3.24–3.25). For the thumb CMC Ab/Ad and MCP Ab/Ad, almost all muscles exhibit a high similarity ($s \geq 0.71$) between the measured and modelled moment arms, except for the flexor pollicis longus (FPL) and the extensor pollicis brevis (EPB) (Figures 3.24–3.25). However, the moment arms of the FPL and EPB are still within two standard deviations (corresponds 95 % of population) of the cadaver measurements.

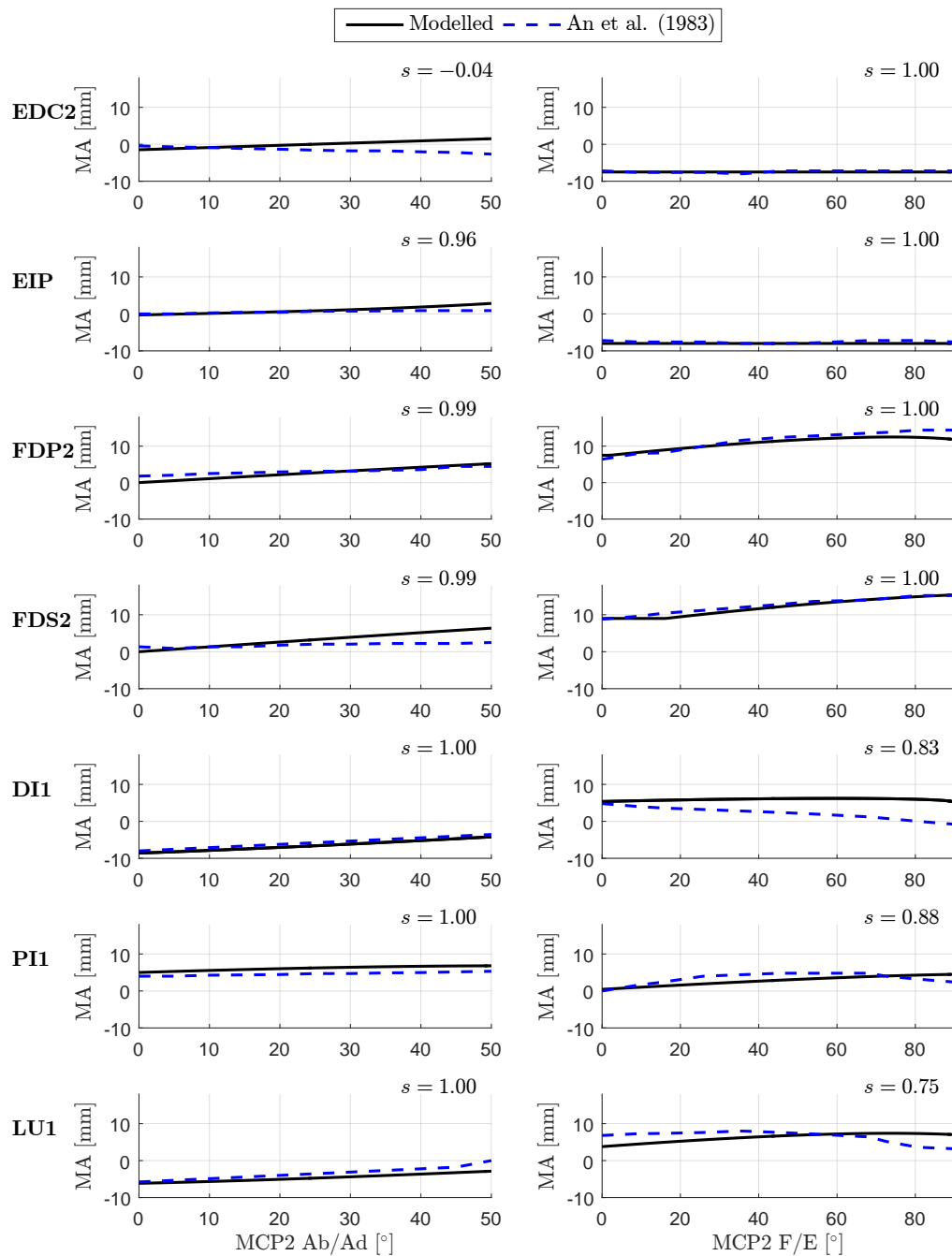


Figure 3.23: Comparison between modelled and measured moment arms (MA) with respect to the index finger metacarpalphalangeal joint (MCP2) degrees of freedom. The two degrees of freedom are presented by flexion/extension (F/E) and abduction/adduction (Ab/Ad).

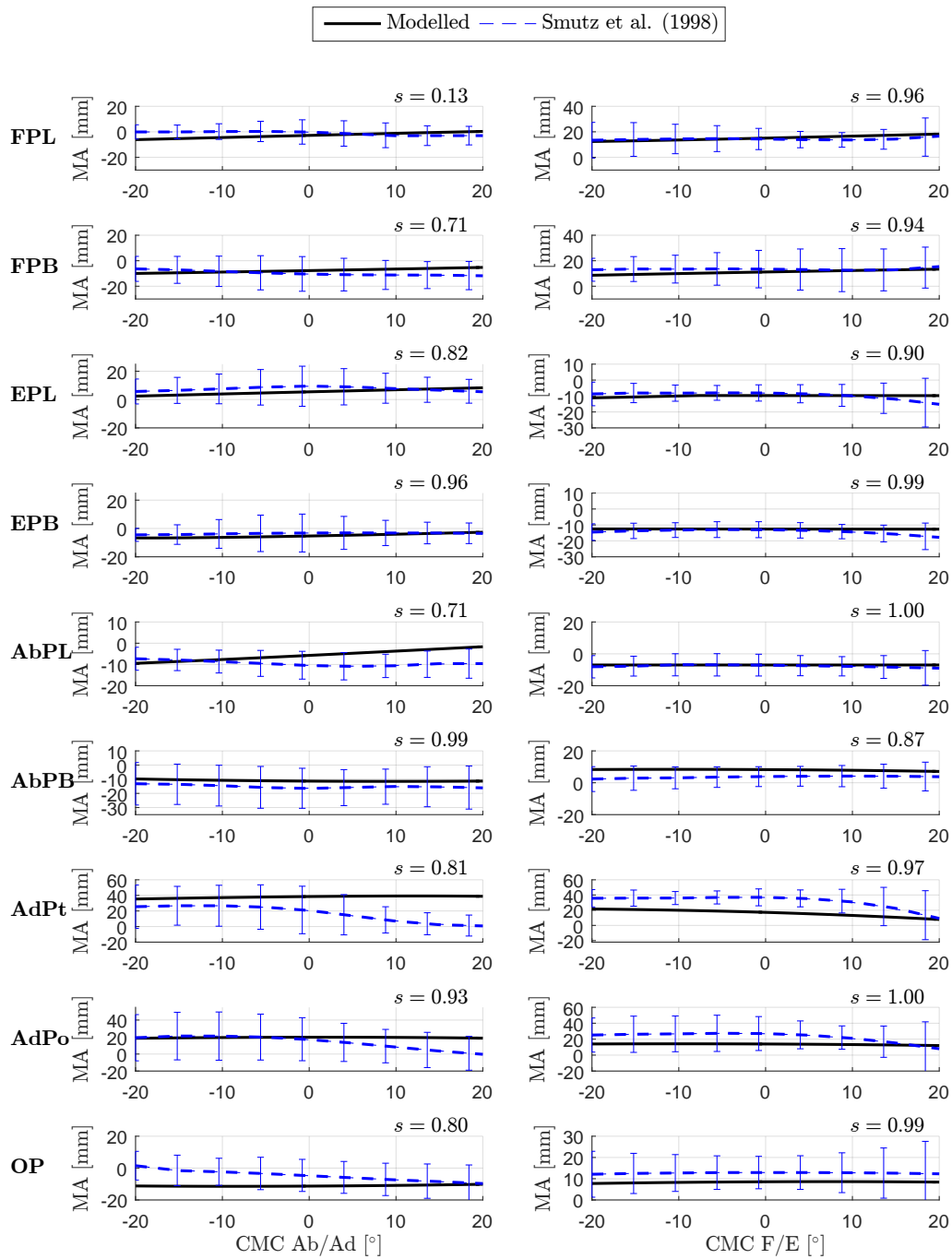


Figure 3.24: Comparison between modelled and measured moment arms (MA) with respect to the thumb carpometacarpal (CMC) joint degrees of freedom. These two degrees of freedom are presented by flexion/extension (F/E) and abduction/adduction (Ab/Add). Error bars denote standard deviations (95% rule in statistics).

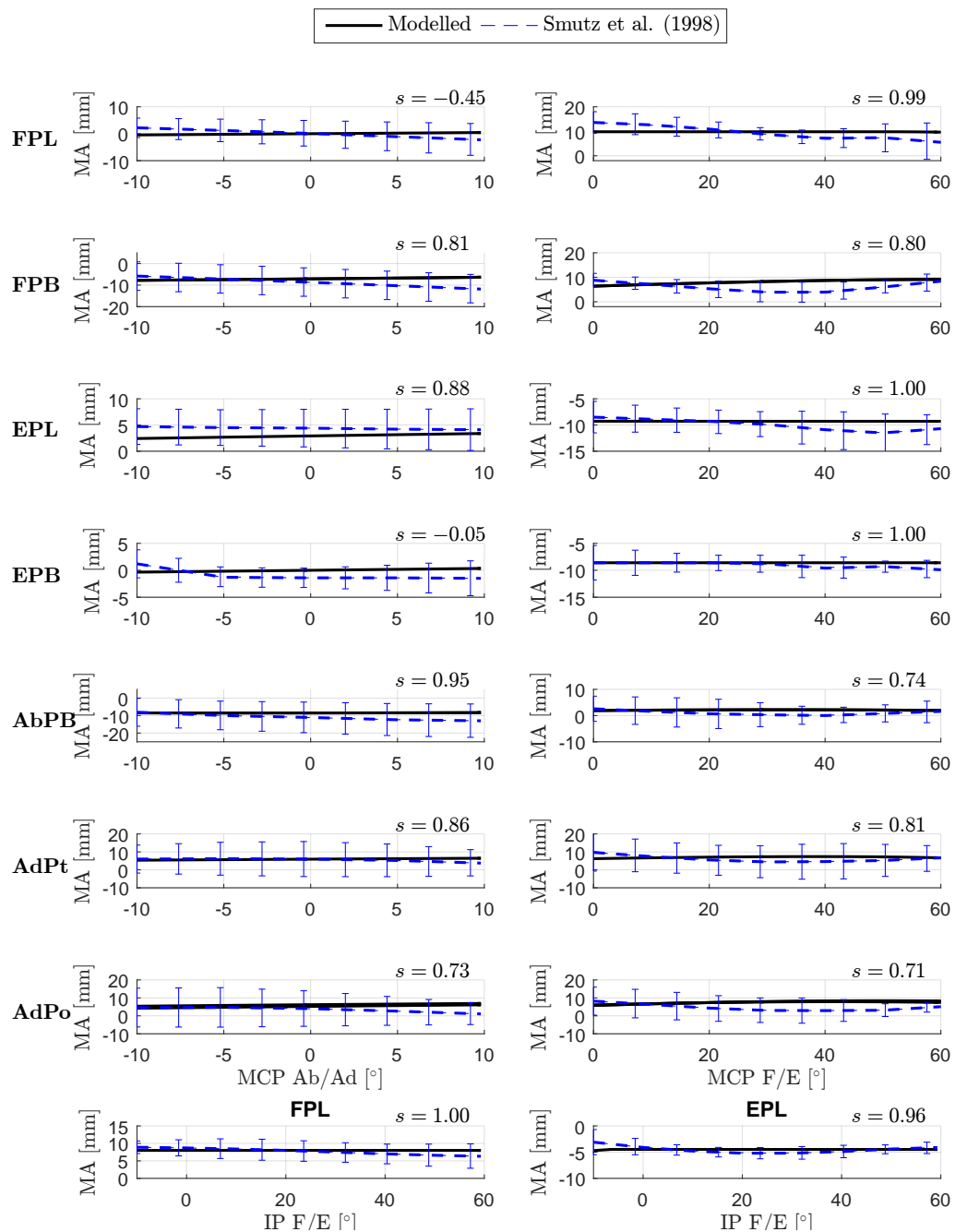


Figure 3.25: Comparison between modelled and measured moment arms (MA) with respect to the thumb metacarpalphalangeal (MCP) and interphalangeal (IP) joint degrees of freedom. The two degrees of freedom are presented by flexion/extension (F/E) and abduction/adduction (Ab/Ad). Error bars denote standard deviations (95% rule in statistics).

3.3.2 Musculotendon dynamic model

A Mathematical Hill-type muscle model

Using Equations 3.21–3.27, the total musculotendon force produced by the contractile and passive elements is constructed and graphically represented in Figure 3.26. The force–length relationship represents general isometric contractions performed with different muscle lengths, while the force–velocity relationship represents general isometric contractions performed with concentric–eccentric contractions shortening and lengthening. The CE force-length relationship shows that the maximum force is developed when the fully-activated muscle, i.e. $u = 1$, is held at its optimal length $l_{m,o}$. While the musculotendon active force is developed between $0.5l_{m,o}$ and $1.5l_{m,o}$, the passive force is developed when the muscle is stretched beyond its optimal length $l_{m,o}$. These curves are similar to the physiological force–length and force–velocity curves, which indicates the correctness of the proposed mathematical model for normalised force and normalised muscle length.

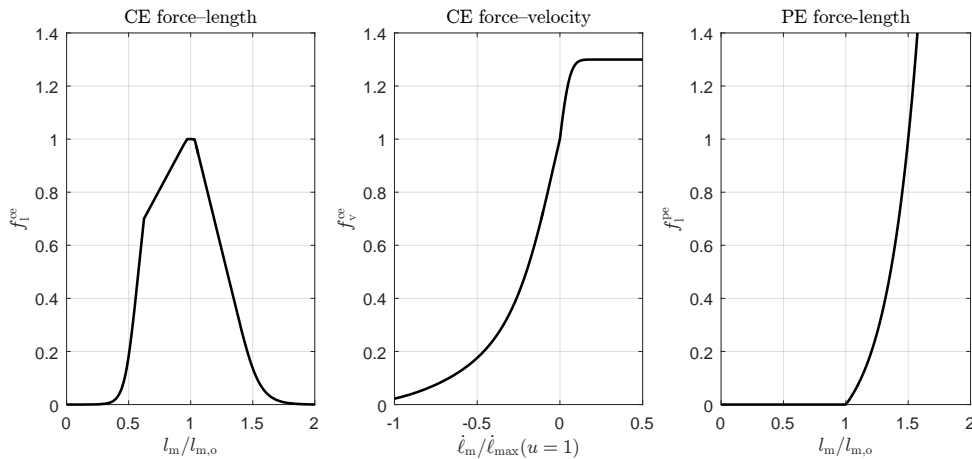


Figure 3.26: Model characteristics: active and passive force–length, and force–velocity relationships.

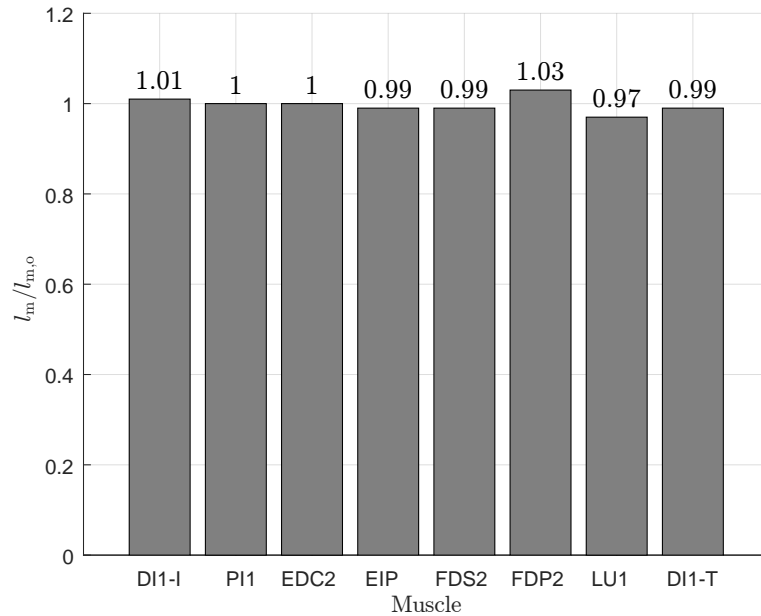
B Model parameters

The calculated tendon slack length is shown in Table 3.5. Based on these values, the resulting normalised muscle length $l_m/l_{m,o}$ for extrinsic and intrinsic index muscles in resting posture and simulated MCP2 joint F/E motion is shown in Figure 3.27 and Figure 3.28, respectively. While the $l_m/l_{m,o}$ ranges between 0.97 and 1.03 in the resting posture, it ranges between 0.5 and 1.7 for the MCP2 joint F/E motion.

The simulated MCP2 F/E (Equation 3.17) consists of three main phases, i.e. flexion, extension, and neutral (Figure 3.28). The flexion phase represents the phase where the flexion angle is increasing, e.g. between 2.7 and 3.8 seconds. The extension phase is the

Table 3.5: The calculated tendon slack length.

	Muscle							
	FDS2	FDP2	EDC2	EIP	DI1-I	DI1-T	PI1	LU1
$l_{t,o}$ [mm]	318	335	381	215	10	35	28	37

Figure 3.27: Normalised muscle length $l_m/l_{m,o}$ for the extrinsic and intrinsic index finger muscles in resting posture (Task S1 in Figure 2.9).

phase where the flexion angle is decreasing, e.g. between 0.8 and 2.0 seconds. Finally, the neutral phase represents the phase where the flexion angle is around zero, e.g. between 2.2 and 2.7 seconds.

During the flexion phase, the extrinsic extensor muscles, i.e. EDC2 and EIP, extend to reach a normalised length of 1.32, while the extrinsic flexor muscles, i.e. FDS2 and FDP2, contract to reach a normalised length of 0.50-0.62 (Figure 3.28). In the extension phase, the extrinsic extensor muscles contract, while the extrinsic flexor muscles extend to return to the normalised length of 1.0 as in the neutral phase (Figure 3.28). Compared to the length change of the extrinsic muscles (32-50%), the intrinsic muscles show less change (3-27%). This is in agreement with Kuo and Deshpande (2012), who pointed out that the extrinsic muscles have longer length stretching compared to the intrinsic muscles.

C Musculotendon force and torque

The extrinsic muscles (EDC2, EIP, FDS2, and FDP2) produce a higher F_{pe} (between 1 N and 4 N) compared to the intrinsic muscles (DI1-I, PI, LU1, and DI1-T) with $F_{pe} < 1$

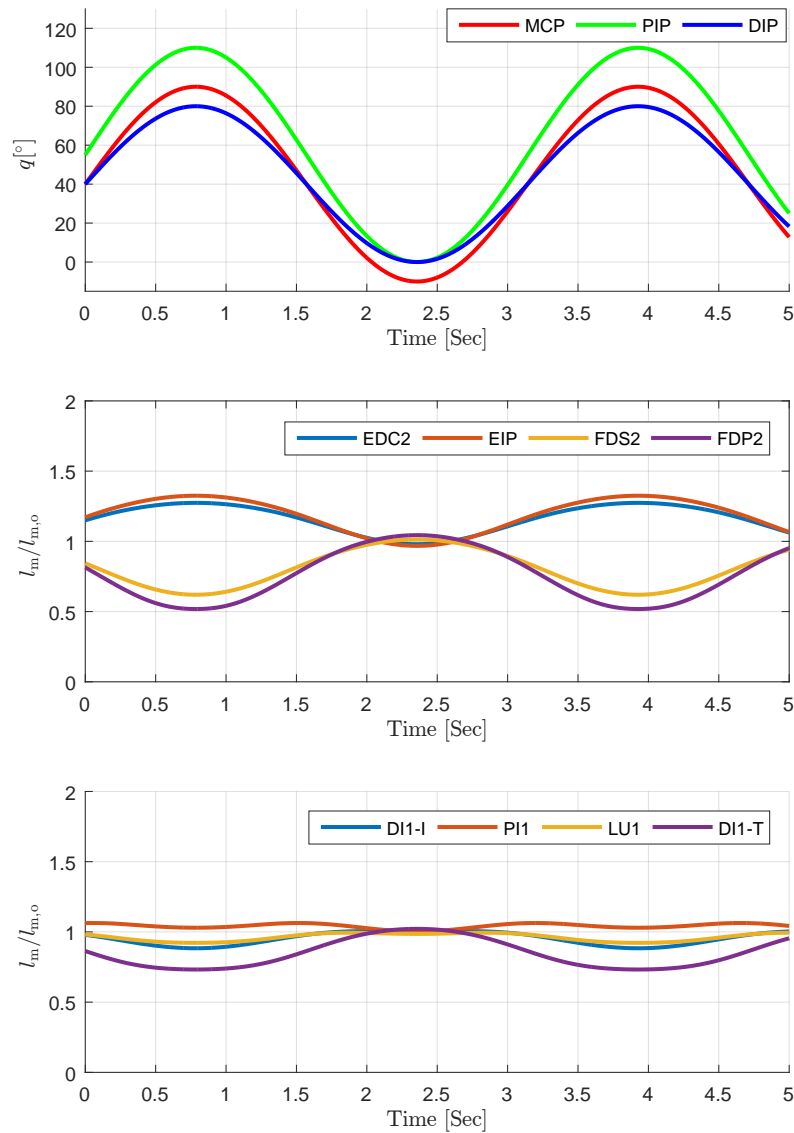


Figure 3.28: Normalised muscle length $l_m/l_{m,o}$ for a simulated index finger joint flexion/extension motion. Top: the simulated flexion/extension motion, which is obtained using sinusoidal functions as in Equation 3.17. Middle and bottom: the normalised muscle length during the motion for the extrinsic and intrinsic index finger muscles, respectively.

N (Figure 3.29). These results are in agreement with the results of Kuo and Deshpande (2012), who related the high force production of extrinsic muscles to their longer length stretching compared to the intrinsic muscles. In the extrinsic muscles, when the finger is flexed from neutral position, i.e. from 0° to 100° , the extensor muscles (EDC2 and EIP) are extended, which results in producing up to 4 N passive force. When the finger is extended beyond the neutral position, i.e. from 0° to -20° , the flexor muscles (FDS2 and FDP2) are extended more than the optimal length and thus produce up to 2.5 N passive force. The resulting passive forces in extrinsic muscles increase exponentially with

stretching length and thus the resulting moment has an exponential dependency on joint configuration (Kuo and Deshpande 2012).

As the force F_{pe} is zero for the flexors during flexion (from 0° to 100°) and the extensors during extension (from 0° to -20°), the resulting $\tau_{mt,pe}$ is likely-wise zero. A small difference is noticed between the $\tau_{mt,pe}$ resulting from the proposed model and Kuo and Deshpande model (Kuo and Deshpande 2012) (Figure 3.29). This might be due to the differences between subjects in this model and the literature model. These differences affect J^T , and hence the resulting $\tau_{mt,pe}$. Thus, in order to validate the resulting torque while considering the individual anthropometric variations, the curve pattern of the torque should be compared rather than the absolute difference. This was evaluated by calculating the Pearson's correlation coefficient ρ between the torque resulting from the proposed model and the one from the literature model. The high correlation coefficient ($\rho = 0.96$) indicates a very high similarity between the compared torques.

D Muscle activation estimation

The muscle activations resulting from the proposed muscle activation model are shown in Figure 3.30 for a simulated MCP2 F/E. At the beginning of the simulated motion, the index finger flexes, which results in an increase in the flexion angle to reach 100° . During this phase, the flexor muscles are activated, with muscle activations nearly up to 0.1. After that, the index finger starts to extend and accordingly the flexion angle decreases. At this extension phase, the extensor muscles are activated, with muscle activations nearly up to 0.6. The activation during extension phase is larger than during flexion phase. This might be explained due to moving the finger against gravity during extension, where greater force is needed and thus greater activation. The estimated u is fed to the proposed Hill-type muscle model (Equations 3.21–3.27) to calculate musculotendon forces. Finally, the torque resulting from the proposed Hill-type muscle model $\tau_{mt,pe}$ ranges between -0.26 N.m and 0.14 N.m and similar to the torque from the skeletal dynamic model τ .

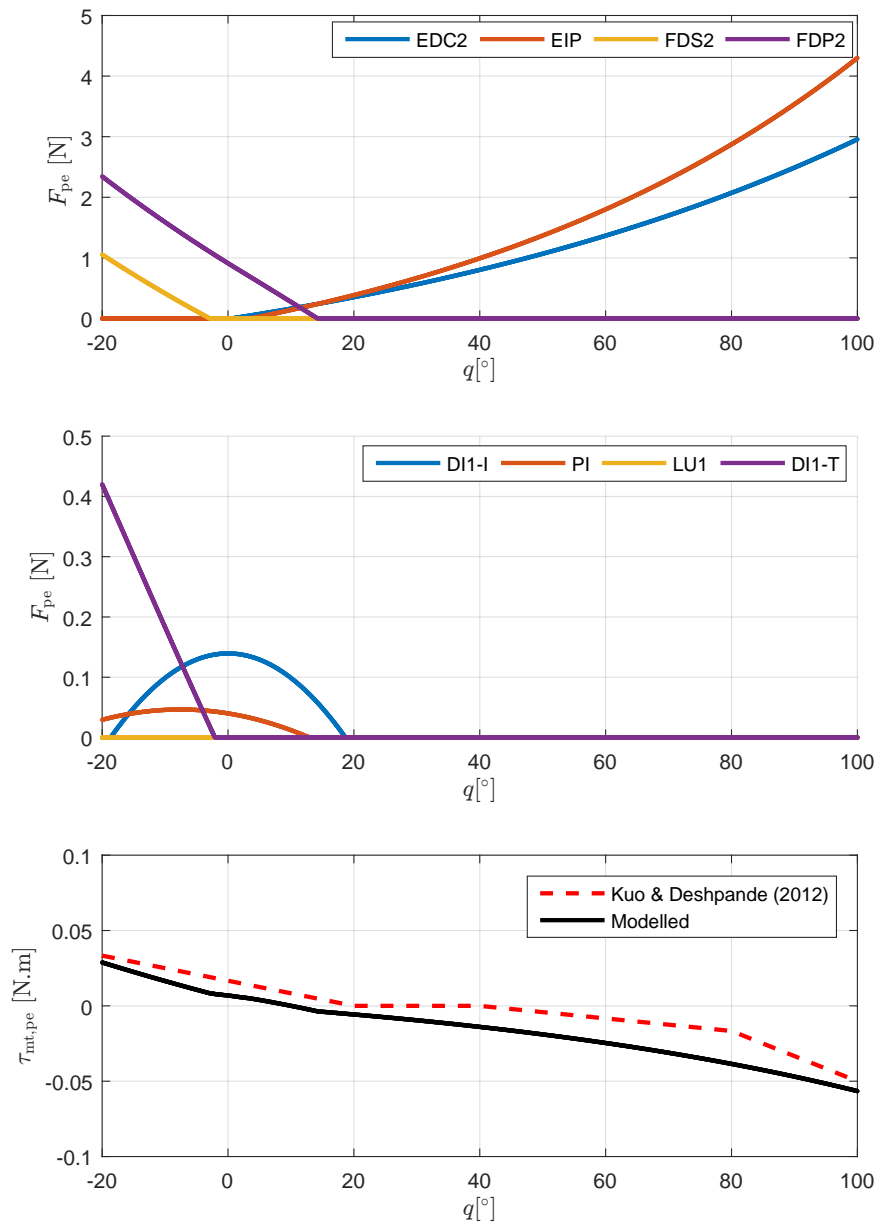


Figure 3.29: The resulting F_{pe} and $\tau_{mt,pe}$ at the index finger MCP joint. The passive musculotendon torque resulting from the proposed model is compared to the modelled torque from the literature (Kuo and Deshpande 2012).

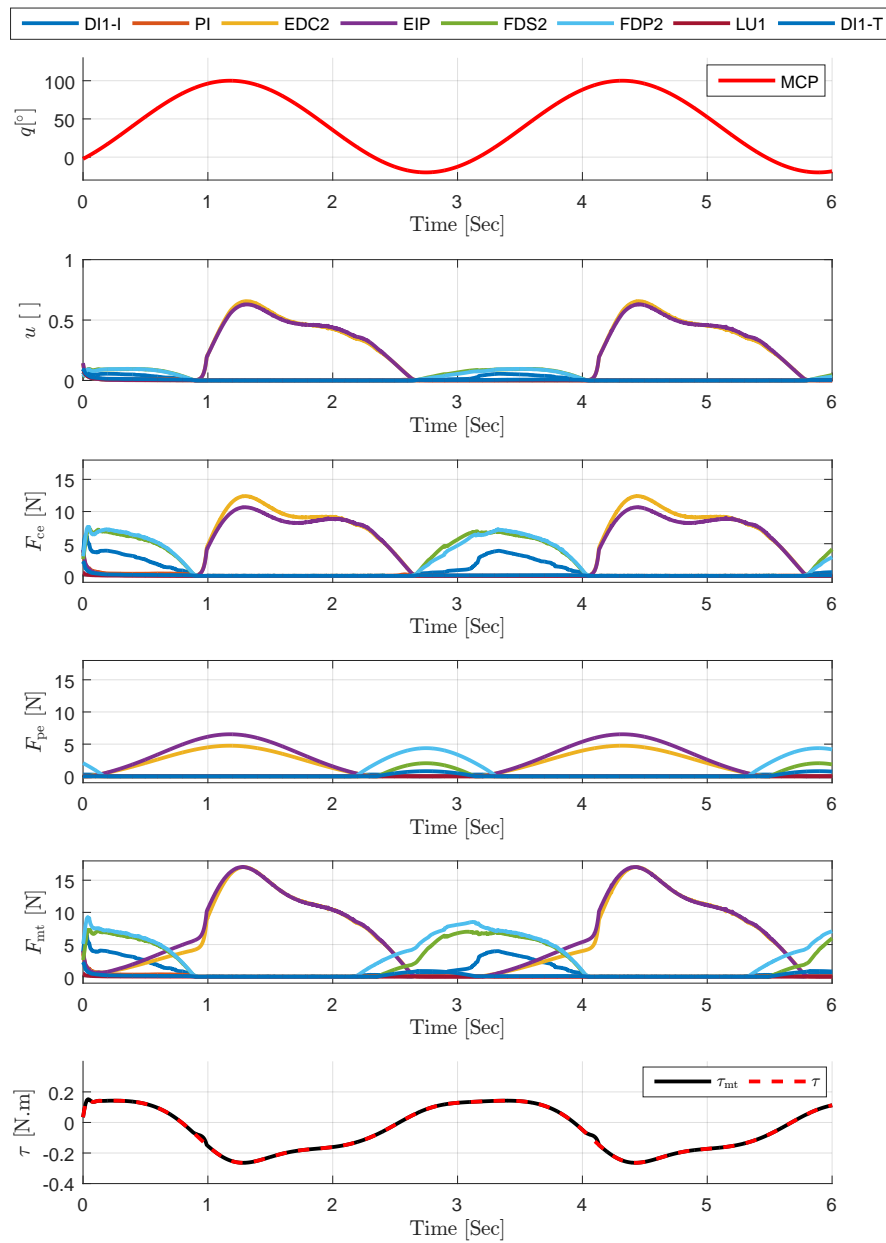


Figure 3.30: The resulting muscle activations, forces, and torque for a simulated MCP2 F/E motion. This motion is obtained using sinusoidal functions (Equation 3.17).

3.4 Conclusion

In this chapter, two musculotendon models are presented: the kinematic model and the dynamic model. In the kinematic model, a complete muscle-joint kinematic model of all 27 extrinsic and intrinsic hand muscles is proposed. This model considers these 27 muscles as 47 musculotendon paths and calculates musculotendon lengths, length change rates, and musculotendon excursion moment arms as a function of joint configuration. In the dynamic model, a Hill-type muscle model for the index finger muscles as well as its parameters are proposed. This model predicts the musculotendon forces for given musculotendon lengths, length change rates, and muscle activations. The musculotendon length and its change rates are obtained from the proposed musculotendon kinematic model, while muscle activations are obtained from the proposed muscle activation estimation model. Using this model, muscle activations are optimised with a minimum difference between the resulting torque from the musculotendon dynamic model and the skeletal dynamic model. The kinematic model is validated by comparing the modelled moment arms with the available cadaver measurements from the literature, while the dynamic model is validated by comparing the resulting forces and torques with the literature results when available, as well as the overall model consistency. For most muscles compared, high similarity with $s \geq 0.70$ for 92% of cases is shown between the modelled moment arms and cadaver measurements available from the literature. The overall consistency in the dynamic model, i.e. from muscle activation to torque, indicates the correctness of our proposed model. However, the complete musculotendon model has the following limitations: 1) to the best of the authors' knowledge, the moment arms for all muscles of the middle, ring and little fingers have not been reported in cadaver measurements, thus, the kinematic model is validated for available measurements, i.e. index MCP joint and thumb joints only, and 2) the muscle activation model is limited to index finger muscles for MCP joint F/E. Therefore, future work will address: 1) extensive experimental measurement of hand muscle moment arms, with which the complete hand muscle-joint kinematic model can be validated, 2) experimental measurement of the Hill-type muscle model parameters for the complete hand muscles, and 3) modelling of muscle activation estimation for the complete hand muscles with experimental validation using synchronised motion tracking and sEMG.

Chapter 4

Summary and future work

This thesis aimed to develop a human hand neuromusculoskeletal model that serves as a tool in studying and replicating human behaviour. This yielded the following objectives (Figure 4.1):

- O1)** Developing a complete highly accurate human hand kinematic model.
- O2)** Developing a skeletal dynamic model that is consistent with the musculoskeletal kinematic model and includes the passive visco-elastic properties of the finger joints.
- O3)** Developing a complete computational model that includes all intrinsic and extrinsic muscles, for musculotendon paths and muscle-joint kinematics.
- O4)** Proposing a musculotendon dynamic model, i.e. a Hill-type muscle model, for the index finger.
- O5)** Proposing a muscle activation estimation model for the index finger.

All posed objectives have been successfully achieved and the developed models have contributions and limitations as follows.

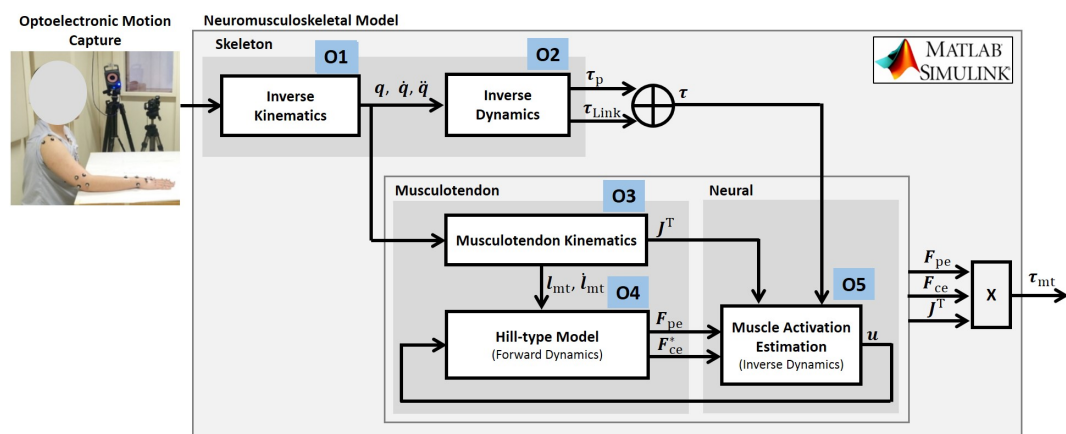


Figure 4.1: Block diagram of the proposed human hand neuromusculoskeletal model illustrates the corresponding objectives.

The first objective (**O1**) was to develop a skeletal kinematic model. This model has 26 DoFs, of which 4 DoFs describe each of the four fingers, 6 DoFs describe the thumb, and 4 DoFs describe the palm arc. It maps surface landmark positions into joint configurations based on forward and inverse mapping functions that estimate joint CoRs. Model identification was experimentally performed using an optoelectronic motion capture system. The fidelity of the mathematical formulations of the model and the associated identification procedure is demonstrated by the sub-millimetre difference between the surface marker positions estimated by the forward kinematics model and the positions directly measured by the motion tracking system. The proposed palm arc model has an improved accuracy (sub-millimetre) and pose estimation of the pinky and ring fingers compared to the proposed rigid palm models in the literature (error is up to 70.0 mm). Additionally, modelling the thumb with 6 DoFs (5 actuated DoFs and 1 passive DoF) and with its own reference system resulted in a significantly improved, accurate, and adaptable model that minimises the effect of the individual physiologic variations. Notably, with the development of the skeletal kinematic model, we were able to improve various modelling assumptions from the literature and address the most important limitations in the state-of-the-art models. Yet, this model has a few limitations that should be considered in the future including: 1) the passive DoFs and their relation to the change in the D-H parameter d_k were not investigated in the four fingers, and 2) the model was experimentally validated using three dynamic tasks and two static tasks of nine subjects. The dynamic tasks were limited to abduction/adduction and grasp/release of cylinders. These tasks did not clearly reflect the effects of the physical finger-object interactions and their relation to the model accuracy, i.e. pick and place objects with different weights.

The second objective (**O2**) was to develop a skeletal dynamic model that is compatible with the proposed skeletal kinematic model. This model calculates both the link torque (due to gravitational and inertial forces) and the passive torque (due to the passive joint properties) for a given joint configuration as an input. This model enhanced the previously developed human hand skeletal dynamic models in the literature by: 1) extending the 16 DoF model of Serbest et al. (2016) to include the 26 DoFs as proposed in the skeletal kinematic model (**O1**), and 2) incorporating the visco-elastic properties of the finger joints. As the passive visco-elastic properties of the complete hand joints are rarely studied in the literature, the passive torque model is limited to modelling the 6 DoFs of the thumb and the 3 DoFs of the fingers (F/E DoFs only).

The third objective (**O3**) was to develop a musculotendon kinematic model. This model considers all extrinsic and intrinsic hand muscles and calculates musculotendon lengths, length change rates, and musculotendon excursion moment arms as a function of joint configuration. The modelled musculotendon excursion moment arms considers the variations due to joint configuration and subject dependency, which results in a more realistic in-vivo muscle driven torque generation behaviour. The resulting musculotendon lengths, and their rate of change, as well as muscle activations are fed into the muscu-

lotendon dynamic model which estimates the musculotendon forces and, together with the moment arms, the musculotendon torques. The proposed model addressed the limitations of the state-of-the-art models by: 1) including the 26 DoFs of the human hand, 2) including all extrinsic and intrinsic hand muscles, and 3) implementing the model in Simulink[®] as it provides a framework for designing and implementing closed-loop human hand motor control and simulating rather complex physical interaction between the human hand and the environment. The high similarity (with similarity coefficient $s \geq 0.70$ for 92% of cases) between the modelled moment arms and the cadaver measurements available from the literature underlines the correctness of the modelled moment arms and imply the feasibility of modelled musculotendon paths, lengths, and length change rates. To the best of the authors' knowledge, the moment arms for all muscles of the four fingers with respect to all their DoFs have not been reported in cadaver measurements. Thus, the validation of this model was limited to the available measurements, i.e. the MCP joint of the index finger and the thumb joints only.

The fourth and fifth objectives were to develop a musculotendon dynamic model (a Hill-type muscle model) (**O4**) and an activation estimation model (**O5**). The musculotendon dynamic model calculates the musculotendon forces for given lengths, length change rates, and muscle activations. The musculotendon length and its change rates are obtained from the proposed musculotendon kinematic model (**O3**), while muscle activations are obtained from the proposed muscle activation estimation model (**O5**). The Hill-type muscle model parameters from the literature were modified to suit the mathematical description of the proposed model. Using muscle activation estimation model (**O5**), muscle activations are optimised with a minimum difference between the resulting torque from musculotendon dynamic model and skeletal dynamic model. The musculotendon dynamic model is validated by comparing the resulting forces and torques with literature results when available as well as the overall model consistency. However, the muscle activation model is limited to the index finger muscles for MCP joint F/E DoF.

Future work

This thesis opens new research opportunities either to enhance and extend the proposed models or to answer interesting open research questions that came up during this research. The proposed human hand neuromusculoskeletal model can be further enhanced by addressing the limitations in the developed models, including:

1. Experimental analysis of the passive DoFs (joint elasticity) in all hand joints with respect to the physical finger-object interactions.
2. Deeper analysis of the changes of the D-H parameter d_k while executing different tasks and their relation to joint elasticity.

3. Skeletal kinematic model validation using different experimental tasks that reflect the effects of the physical finger-object interactions and their relation to the model accuracy.
4. Experimental validation of the proposed link torque model.
5. Modelling the passive torque for the complete 26 DoFs of the human hand.
6. Extensive experimental measurement of hand muscle moment arms, with which the complete hand muscle-joint kinematic model can be validated.
7. Hill-type muscle model parameter measurement (Cadaver study) for the complete hand muscles.
8. Modelling of muscle activation estimation for the complete hand muscles with experimental validation using synchronised motion tracking and sEMG.

After addressing the limitations in the proposed human hand neuromusculoskeletal model, this model can be extended by integrating it with the complementary shoulder-arm model. This will result in a complete upper-limb neuromusculoskeletal model that can be used as a tool in studying and replicating human behaviour, which is essential in designing assistive devices, rehabilitation manipulators, prosthetic and orthotic devices, as well as evaluating safe human-robot interaction. It would be also interesting to answer open research questions such as:

1. Is the linear relationship between surface and skeleton rotational angles subject dependent, or task dependant, or both?
2. Do the four fingers have similar passive joint properties?
3. How do the passive joint properties change among subjects?

A summary of the open research points in the literature with the corresponding contributions and future work of the proposed five models is shown in Table 4.1.

Table 4.1: Summary of the contributions and future work of the models proposed in this thesis.

Anatomical structure	Modelling objective	Comparison	Models		Future work ^a
			State-of-the-art	Proposed	
Skeleton	O1: Kinematic	Four fingers	Specific joints, or reduced DoFs, or some digits only	Four fingers (4 DoFs each)	▷ Experimental analysis of the passive DoFs ▷ Investigating the change of the D-H parameter d_k
		Thumb	3 Dofs, 4 DoFs, and 5 DoFs Hand plane related reference system CoR not identified Error is up to 1.7 mm	6 DoFs Its own reference system CoR identified Sub-millimetre accuracy	
		CoR estimation	Direct translation, optimisation, and circle intersection	Systematic flexion/extension CoR estimation algorithm, including the forward and inverse kinematics mapping between surface and skeleton kinematics	
		Palm arc	Rigid palm Error is up to 70.0 mm	Two joints (4 DoFs) Sub-millimetre accuracy	
		Experimental set-up	Specially designed clusters or calibration tools are needed	Practical experimental set-up	
	O2: Dynamic	Total torque	Link torque only or passive torque only	Both link torque and passive torque	
		Link torque	16 DoFs	26 DoFs	▷ Experimental validation
Passive torque		Damping torque (26 DoFs) + stiffness torque (21 DoFs, linear)	Damping torque (26 DoFs) + stiffness torque (19 DoFs, double exponential)	▷ Modelling of the 26 DoFs of the hand	
Musculotendon	O3: Kinematic	Hand DoFs	15 DoFs, and 20 DoFs	26 DoFs	▷ Experimental validation of the modelled musculotendon excursion moment arms
		Muscles	Not all hand muscles are included	All extrinsic and intrinsic muscles	
		Software platform	OpenSim	MATLAB	
	O4: Dynamic	Different formulations of the Hill-type muscle model	Hill-type muscle model that consistent with the musculotendon kinematic model	▷ Cadaver measurement of the Hill-type muscle model parameters of the complete hand	
	O5: Muscle activation	Static optimisation	Static optimisation (Index finger muscles, MCP F/E DoF)	▷ Extend the model to estimate the activation for the complete hand muscles and DoFs ▷ Experimental validation using synchronised motion tracking and sEMG	

^a Experimental validation for the complete human hand neuromusculoskeletal model using synchronised motion tracking and sEMG for different daily activity tasks.

Appendix A

Solving for rotational angles

Q's for 1st digit. The 6 DoFs of the thumb are calculated as in (A.1a – A.1f).

$$Q_1 = \text{atan2}({}^0Y_{\text{MCP}}, {}^0X_{\text{MCP}}), \quad (\text{A.1a})$$

$$Q_2 = \text{atan2}({}^0Z_{\text{MCP}}, \frac{{}^0X_{\text{MCP}}}{\cos Q_1}), \quad (\text{A.1b})$$

$$Q_3 = \text{atan2}({}^2Y_{\text{IP}}, {}^2X_{\text{IP}}), \quad (\text{A.1c})$$

$$Q_4 = \text{atan2}({}^2Z_{\text{IP}}, \frac{{}^2X_{\text{IP}}}{\cos Q_3}), \quad (\text{A.1d})$$

$$Q_5 = \text{atan2}({}^4Y_{\text{Tip}}, {}^4X_{\text{Tip}}), \quad (\text{A.1e})$$

$$Q_6 = \text{atan2}({}^4Z_{\text{Tip}}, \frac{{}^4X_{\text{Tip}}}{\cos Q_5}), \quad (\text{A.1f})$$

where:

${}^0X_{\text{MCP}}$: is the x-component of MCP landmark position in {0}

${}^0Y_{\text{MCP}}$: is the y-component of MCP landmark position in {0}

${}^0Z_{\text{MCP}}$: is the z-component of MCP landmark position in {0}

${}^2X_{\text{IP}}$: is the x-component of IP landmark position in {2}

${}^2Y_{\text{IP}}$: is the y-component of IP landmark position in {2}

${}^2Z_{\text{IP}}$: is the z-component of IP landmark position in {2}

${}^4X_{\text{Tip}}$: is the x-component of Tip landmark position in {4}

${}^4Y_{\text{Tip}}$: is the y-component of Tip landmark position in {4}

${}^0\mathbf{X}_i$ is calculated by Equation 2.6 and the transformation matrix ${}^B\mathbf{T}_0$.

${}^k\mathbf{X}_i$ is calculated by Equation 2.6 and the $Q_{1\dots k}$ from the previous steps.

Q's for 4th and 5th digits. Equations (A.2a – A.2f) are used to calculate the rotational angles as follows:

$$Q_1 = \text{atan2}({}^B Y_{\text{MCP}}, {}^B X_{\text{MCP}}), \quad (\text{A.2a})$$

$$Q_2 = \text{atan2}({}^B Z_{\text{MCP}}, \frac{{}^B X_{\text{MCP}}}{\cos Q_1}), \quad (\text{A.2b})$$

$$Q_3 = \text{atan2}({}^2 Y_{\text{PIP}}, {}^2 X_{\text{PIP}}), \quad (\text{A.2c})$$

$$Q_4 = \text{atan2}({}^2 Z_{\text{PIP}}, \frac{{}^2 X_{\text{PIP}}}{\cos Q_3}), \quad (\text{A.2d})$$

$$Q_5 = \text{atan2}({}^4 Y_{\text{DIP}}, {}^4 X_{\text{DIP}}), \quad (\text{A.2e})$$

$$Q_6 = \text{atan2}({}^5 Y_{\text{Tip}}, {}^5 X_{\text{Tip}}), \quad (\text{A.2f})$$

where:

${}^B X_{\text{MCP}}$: is the x-component of MCP landmark position in {B}

${}^B Y_{\text{MCP}}$: is the y-component of MCP landmark position in {B}

${}^B Z_{\text{MCP}}$: is the z-component of MCP landmark position in {B}

${}^2 X_{\text{PIP}}$: is the x-component of PIP landmark position in {2}

${}^2 Y_{\text{PIP}}$: is the y-component of PIP landmark position in {2}

${}^2 Z_{\text{PIP}}$: is the z-component of PIP landmark position in {2}

${}^4 X_{\text{DIP}}$: is the x-component of DIP landmark position in {4}

${}^4 Y_{\text{DIP}}$: is the y-component of DIP landmark position in {4}

${}^5 X_{\text{Tip}}$: is the x-component of Tip landmark position in {5}

${}^5 Y_{\text{Tip}}$: is the y-component of Tip landmark position in {5}

${}^k X_i$ is calculated by Equation 2.6 and the $Q_{1\dots k}$ from the previous steps.

Bibliography

- Ackermann, M and W Schiehlen (2009). "Physiological methods to solve the force-sharing problem in biomechanics". In: *Multibody Dynamics: Computational Methods and Applications*. Ed. by CL Bottasso. Dordrecht: Springer Netherlands, pp. 1–23.
- Agarwal, P, A Hechanova, and AA Deshpande (2013). "Kinematics and dynamics of a biologically inspired index finger exoskeleton". In: *13th ASME dynamic systems and control conference*. Palo Alto, CA, USA.
- Amis, AA, D Dowson, and V Wright (1979). "Muscle strengths and musculo-skeletal geometry of the upper limb". In: *Engineering in Medicine* 8, pp. 41–48.
- An, KN, Y Ueba, EY Chao, WP Cooney, and RL Linscheid (1983). "Tendon excursion and moment arm of index finger muscles". In: *Journal of Biomechanics* 16.7, pp. 419–425.
- An, KN, BM Kwak, EY Chao, and BF Morrey (1984). "Determination of muscle and joint forces: a new technique to solve the indeterminate problem". In: *Journal of Biomedical Engineering* 106.4, pp. 364–367.
- Anderson, F and M Pandy (2001). "Static and dynamic optimization solutions for gait are practically equivalent". In: *Journal of Biomechanics* 34, pp. 153–61.
- Anderson, F and M Pandy (2002). "Individual muscle contributions to support in normal walking". In: *Gait and Posture* 17, pp. 159–169.
- Artemiadis, PK and KJ Kyriakopoulos (2007). "EMG-based teleoperation of a robot arm using low-dimensional representation". In: *2007 IEEE/RSJ International Conference on Intelligent Robots and Systems*. San Diego, CA, USA.
- Artemiadis, PK and KJ Kyriakopoulos (2010). "EMG-based control of a robot arm using low-dimensional embeddings". In: *IEEE Transactions on Robotics* 26.2, pp. 393–398.
- Audo, ML and DT Davy (1985). "The influence of muscle model complexity in musculoskeletal motion modeling". In: *Journal of Biomechanical Engineering* 107.2, pp. 147–157.
- Barnett, CH and AF Cobbold (1968). "Effects of age upon the mobility of human finger joints". In: *Annals of the rheumatic diseases* 27.2, 175–177.
- Blemker, SS and SL Delp (2005). "Three-dimensional representation of complex muscle architectures and geometries". In: *Annals of Biomedical Engineering* 33.8, pp. 1134–1134.
- Braido, P and X Zhang (2004). "Quantitative analysis of finger motion coordination in hand manipulative and gestic acts". In: *Human Movement Science* 22, pp. 661–678.
- Brand, PW, KC Cranor, and JC Ellis (1975). "Tendon and pulleys at the metacarpophalangeal joint of a finger". In: *The Journal of Bone and Joint Surgery* 57, pp. 779–784.

- Brand, PW, RB Beach, and DE Thompson (1981). "Relative tension and potential excursion of muscles in the forearm and hand". In: *The Journal of hand surgery* 6, pp. 209–19.
- Brand, PW and AM Hollister (1999). *Clinical Mechanics of the Hand*. English. 3rd edition. Mosby Inc.
- Buchanan, TS, DG Lloyd, K Manal, and TF Besier (2004). "Neuromusculoskeletal modeling: estimation of muscle forces and joint moments and movements from measurements of neural command." In: *Journal of Applied Biomechanics* 20.4, pp. 367–95.
- Buchanan, TS, DG Lloyd, K Manal, and TF Besier (2005). "Estimation of muscle forces and joint moments using a forward-inverse dynamics model". In: *Medicine and Science in Sports and Exercise* 37.11, pp. 1911–6.
- Buchholz, B, TJ Armstrong, and SA Goldstein (1992). "Anthropometric data for describing the kinematics of the human hand". In: *Ergonomics* 35.3, pp. 261–273.
- Bullock, IM, J Borràs, and AM Dollar (2012). "Assessing assumptions in kinematic hand models: a review". In: *The Fourth IEEE RAS/EMBS International Conference on Biomedical Robotics and Biomechatronics*.
- Carpinella, I, P Mazzoleni, M Rabuffetti, R Thorsen, and M Ferrarin (2006). "Experimental protocol for the kinematic analysis of the hand: definition and repeatability". In: *Gait and Posture* 23, pp. 445–454.
- Cavallaro, E, J Rosen, JC Perry, S Burns, and B Hannaford (2005). "Hill-based model as a myoprocessor for a neural controlled powered exoskeleton arm - parameters optimization". In: *Proceedings of the 2005 IEEE International Conference on Robotics and Automation*, pp. 4514–4519.
- Cavallaro, EE, J Rosen, JC Perry, and S Burns (2006). "Real-time myoprocessors for a neural controlled powered exoskeleton arm". In: *IEEE Transactions on Biomedical Engineering* 53.11, pp. 2387–2396.
- Cerveri, P, ED Momi, N Lopomo, G Baud-Bovy, R Barros, and G Ferrigno (2007). "Finger kinematic modeling and real-time hand motion estimation". In: *Annals of Biomedical Engineering* 35.11, pp. 1989–2002.
- Chang, LY and Y Matsuoka (2006). "A kinematic thumb model for the ACT hand". In: *Proceedings of the 2006 IEEE International Conference on Robotics and Automation*. Orlando, Florida, pp. 1000–1005.
- Chiu, H-Y, FC Su, S-T Wang, and H-Y Hsu (1998). "The motion analysis system and goniometry of the finger joints". In: *Journal of Hand Surgery: British and European Volume* 23B.6, pp. 788–791.

- Cobos, S, M Ferre, MA Sánchez-Urán, J Ortego, and R Aracil (2010). "Human hand descriptions and gesture recognition for object manipulation". In: *Computer Methods in Biomechanics and Biomedical Engineering* 13.3, pp. 305–317.
- Collins, JJ (1995). "The redundant nature of locomotor optimization laws". In: *Journal of Biomechanics* 28, pp. 251–267.
- Cook, JR, NA Baker, R Cham, E Hale, and MS Redfern (2007). "Measurements of wrist and finger postures: a comparison of goniometric and motion capture techniques". In: *Journal of Applied Biomechanics* 23, pp. 70–78.
- Cooney, WP, MJ Lucca, EYS Chao, and RL Linscheid (1981). "The kinesiology of the thumb trapeziometacarpal joint". In: *The Journal of Bone and Joint Surgery* 63-A.9, pp. 1371–1381.
- Corcos, DM, GL Gottlieb, ML Latash, GL Almeida, and GC Agarwal (1992). "Electromechanical delay: an experimental artifact". In: *Journal of Electromyography and Kinesiology* 2.2, pp. 59–68.
- Cordella, F, L Zollo, A Salerno, D Accoto, E Guglielmelli, and B Siciliano (2014). "Human hand motion analysis and synthesis of optimal power grasps for a robotic hand". In: *International Journal of Advanced Robotic Systems* 11.37, pp. 1–13.
- Craig, JJ (1989). *Introduction to robotics: mechanics and control*. 2nd edition. Addison-Wesley.
- Cram, JR and GS Kasman (1998a). "Instrumentation". In: *Introduction to surface electromyography*. Aspen Publishers, Inc. Chap. 3, pp. 43–80.
- Cram, JR and GS Kasman (1998b). "Introduction". In: *Introduction to surface electromyography*. Aspen Publishers, Inc. Chap. 1, pp. 3–8.
- Crowninshield, RD and RA Brand (1981). "A physiologically based criterion of muscle force prediction in locomotion". In: *Journal of Biomechanics* 14.11, pp. 793–801.
- Daumas, B, W Xu, and J Bronlund (2005). "Jaw mechanism modeling and simulation". In: *Mechanism and Machine Theory* 40.7, pp. 821–833.
- Degeorges, R, J Parasie, D Mitton, N Imbert, J-N Goubier, and F Lavaste (2005). "Three-dimensional rotations of human three-joint fingers: an optoelectronic measurement. Preliminary results". In: *Surgical and Radiologic Anatomy* 27.1, pp. 43–50.
- Delp, SL, FC Anderson, AS Arnold, P Loan, A Habib, CT John, E Guendelman, and DG Thelen (2007). "Opensim: open-source software to create and analyze dynamic simulations of movement". In: *IEEE Transactions on Biomedical Engineering* 54.11.
- Denavit, J and R Hartenberg (1955). "A kinematic notation for lower-pair mechanisms based on matrices". In: *Transactions ASME Journal of Applied Mechanics* 23, pp. 215–221.

- Deshpande, AD, R Balasubramanian, R Lin, B Dellon, and Y Matsuoka (2008). "Understanding variable moment arms for the index finger MCP joints through the ACT hand". In: *Proceedings of the 2nd Biennial IEEE/RAS-EMBS International Conference on Biomedical Robotics and Biomechatronics*. Scottsdale, AZ, USA.
- Deshpande, AD, R Balasubramanian, J Ko, and Y Matsuoka (2010). "Acquiring variable moment arms for index finger using robotic testbed". In: *IEEE Transactions on Biomedical Engineering* 57.8, pp. 2034–2044.
- Deshpande, AD, N Gialias, and Y Matsuoka (2012). "Contributions of intrinsic viscoelastic torques during planar index finger and wrist movements". In: *IEEE Transactions on Biomedical Engineering* 59.2, pp. 586–594.
- Deshpande, AD, J Ko, DieterFox, and Y Matsuoka (Jan. 2013). "Control strategies for the index finger of a tendon-driven hand". In: *The International Journal of Robotics Research* 32, pp. 115–128.
- Dionysian, E, JM Kabo, F J.Dorey, and R A.Meals (2005). "Proximal interphalangeal joint stiffness: measurement and analysis". In: *The Journal of Hand Surgery* 30.3, pp. 573–579.
- Dipietro, L, AM Sabatini, and P Dario (2003). "Evaluation of an instrumented glove for hand-movement acquisition". In: *Journal of Rehabilitation Research and Development* 40.2, pp. 179–190.
- Dounskaia, N, D Wisleder, and T Johnson (2005). "Influence of biomechanical factors on substructure of pointing movements". In: *Experimental Brain Research* 164.4, pp. 505–516.
- Dul, J, MA Townsend, R Shavi, and GE Johnsson (1984). "Muscularsynergism— I. On criteria for load sharing between synergistic muscles". In: *Journalof Biomechanics* 17, pp. 663–673.
- Eaton, RG and JW Littler (1969). "A study of the basal joint of the thumb, treatment of its disabilities by fusion". In: *The Journal of Bone and Joint Surgery* 51.4, pp. 661–668.
- Esteki, A and JM Mansour (1996). "An experimentally based nonlinear viscoelastic model of joint passive moment". In: *Journal of Biomechanics* 29.4, 443–450.
- Esteki, A and JM Mansour (1997). "A dynamic model of the hand with application in functional neuromuscular stimulation". In: *Annals of Biomedical Engineering* 25.3, pp. 440–451.
- Fok, KS and SM Chou (2010). "Development of a finger biomechanical model and its considerations". In: *Journal of Biomechanics* 43.4, pp. 701–713.

- Fowler, NK, AC Nicol, B Condon, and D Hadley (2001). "Method of determination of three dimensional index finger moment arms and tendon lines of action using high resolution MRI scans". In: *Journal of Biomechanics* 34.6, pp. 791–797.
- Garner, BA and MG Pandy (1999). "A kinematic model of the upper limb based on the visible human project (VHP) image dataset". In: *Computer Methods in Biomechanics and Biomedical Engineering* 2, pp. 107–124.
- Garner, BA and MG Pandy (2000). "The obstacle-set method for representing muscle paths in musculoskeletal models". In: *Computer Methods in Biomechanics and Biomedical Engineering* 3, pp. 1–30.
- Garner, BA and MG Pandy (2003). "Estimation of musculotendon properties in the human upper limb". In: *Annals of Biomedical Engineering* 31.2, pp. 207–220.
- Galias, N and Y Matsuoka (2006). "A musculotendon contribution for multijoint hand control". In: *2006 International Conference of the IEEE Engineering in Medicine and Biology Society*, pp. 4482–4485.
- Goodwin, J, C Clark, J Deakes, D Burdon, and C Lawrence (1992). "Clinical methods of goniometry: a comparative study". In: *Disability and Rehabilitation* 14.1, pp. 10–5.
- Gribble, PL and DJ Ostry (1999). "Compensation for interaction torques during single- and multijoint limb movement". In: *Journal of Neurophysiology* 82.5, pp. 2310–2326.
- Haeufle, D, M Günther, A Bayer, and S Schmitt (2014). "Hill-type muscle model with serial damping and eccentric force-velocity relation". In: *Journal of Biomechanics* 47.6, pp. 1531–1536.
- Hagan, N (1985). "Impedance control: An approach to manipulation: Part I - theory, Part II - implementation, Part III - applications". In: *J. Dynamic Systems, Measurement, and Control* 107, pp. 1–24.
- Hajian, AZ and RD Howe (1997). "Identification of the mechanical impedance at the human finger tip". In: *Journal of Biomechanical Engineering* 119, pp. 109–114.
- Hajian, AZ (1997). "A characterization of the mechanical impedance of human hands". PhD thesis. Harvard University.
- Hall, S (2011). *Basic Biomechanics*. McGraw-Hill Higher Education.
- Hamouda, A, L Kenney, and D Howard¹ (2016). "Dealing with time-varying recruitment and length in Hill-type muscle models". In: *Journal of Biomechanics* 49.14, pp. 3375–3380.
- Hill, AV (1938). "The heat of shortening and the dynamic constants of muscle". In: *Proceedings of the Royal Society of London. Series B, Biological Sciences* 126.843, pp. 136–195.
- Hinkle, D, W Wiersma, and S Jurs (2003). "Applied statistics for the behavioral sciences". In: 6th edition. Houghton Mifflin, Boston, MA.

- Hogan, N (1985). "The mechanics of multi-joint posture and movement control". In: *Biological Cybernetics* 52, pp. 315–331.
- Hollerbach, JM and T Flash (1982). "Dynamic interactions between limb segments during planar arm movement". In: *Biological Cybernetics* 44.1, pp. 67–77.
- Hollister, A, WL Buford, LM Myers, DJ Giurintano, and A Novick (1992). "The axes of rotation of the thumb carpometacarpal joint". In: *Journal of orthopaedic research: official publication of the Orthopaedic Research Society* 10.3, pp. 454–60.
- Holzbour, KRS, WM Murray, and SL Delp (2005). "A model of the upper extremity for simulating musculoskeletal surgery and analyzing neuromuscular control". In: *Annals of Biomed* 33.6, pp. 829–840.
- Hu, T (2015). "Analysis and modeling of human arm withdrawal reflexes using surface electromyography". MA thesis. Leibniz Universität Hannover.
- Hu, T (2016). "A physiological arm model based on the analysis of human withdrawal reflexes using surface electromyography". MA thesis. Leibniz Universität Hannover.
- Huxley, AF (1958). "Muscle structure and theories of contraction". In: *Progress in Biophysics and Biophysics Chemistry* 7, 257 - 318.
- Jacobson, MD, R Raab, BM Fazeli, RA Abrams, MJ Botte, and RL Lieber (1992). "Architectural design of the human intrinsic hand muscles". In: *Journal of Hand Surgery* 17.5, pp. 804–809.
- Jager, M de (1996). "Mathematical head-neck models for acceleration impacts". English. PhD thesis. Eindhoven University of Technology.
- Jamshidi, N, M Rostami, S Najarian, MB Menhaj, M Saadatnia, and S Firooz (2009). "Modelling of human walking to optimise the function of ankle-foot orthosis in Guillan-Barré patients with drop foot". In: *Singapore Medical Journal* 50 4, pp. 412–7.
- Jäntschi, M (2014). "Non-linear control strategies for musculoskeletal robots". PhD thesis. Technische Universität München.
- Jindrich, DL, AD Balakrishnan, and JT Dennerlein (2004). "Finger joint impedance during tapping on a computer keyswitch". In: *Journal of Biomechanics* 37.10, pp. 1589 –1596.
- Jovanovic, K, J Vranic, and N Miljkovic (Jan. 2015). "Hill's and Huxley's muscle models - tools for simulations in biomechanics". In: *Serbian Journal of Electrical Engineering* 12, pp. 53–67.
- Kamper, DG, TG Hornby, and WZ Rymer (2002). "Extrinsic flexor muscles generate concurrent flexion of all three finger joints". In: *Journal of Biomechanics* 35.12, pp. 1581 –1589.
- Kapandji, AI (2007). *The physiology of the joints: annotated diagrams of the mechanics of the human joints*. 6th ed. Vol. 2. Churchill Livingstone.

- Kaplan, M (2000). "Efficient optimal control of large-scale biomechanical systems". PhD thesis. Stanford University.
- Kaufman, KR, KN An, WJ Litchy, and EYS Chao (Feb. 1991). "Physiological prediction of muscle forces-II. Application to isokinetic exercise". In: *Neuroscience* 40, pp. 793–804.
- Keir, PJ, RP Wells, and DA Ranney (1996). "Passive properties of the forearm musculature with reference to hand and finger postures". In: *Clinical Biomechanics* 11.7, pp. 401–409.
- Knutson, JS, KL Kilgore, JM Mansour, and PE Crago (2000). "Intrinsic and extrinsic contributions to the passive moment at the metacarpophalangeal joint". In: *Journal of Biomechanics* 33, 1675–1681.
- Kofman, J, S Verma, and X Wu (2007). "Robot-manipulator teleoperation by markerless vision-based hand-arm tracking". In: *International Journal of Optomechatronics* 1.3, pp. 331–357.
- Konrad, P (2005). *The abc of emg - a practical introduction to kinesiological electromyography*. <http://www.noraxon.com/wp-content/uploads/2014/12/ABC-EMG-ISBN.pdf>. Accessed on June 9, 2015.
- Kuczynski, K (1974). "Carpometacarpal joint of the human thumb". In: *Journal of Anatomy* 118, pp. 119–126.
- Kühn, J, T Hu, M Schappler, and S Haddadin (2018). "Dynamics simulation for an upper-limb human-exoskeleton assistance system in a latent-space controlled tool manipulation task". In: *2018 IEEE International Conference on Simulation, Modeling, and Programming for Autonomous Robots (SIMPAR)*, pp. 158–165.
- Kuo, P-H and AD Deshpande (2010). "Contribution of passive properties of muscle-tendon units to the metacarpophalangeal joint torque of the index finger". In: *2010 3rd IEEE RAS & EMBS International Conference on Biomedical Robotics and Biomechanics*, pp. 288–294.
- Kuo, P-H and AD Deshpande (2012). "Muscle-tendon units provide limited contributions to the passive stiffness of the index finger metacarpophalangeal joint". In: *Journal of Biomechanics* 45.15, pp. 2531–2538.
- Kuthe, C, R Uddanwadiker, PM Padole, and A Ramteke (Mar. 2015). "Mathematical model for skeletal muscle to simulate the concentric and eccentric contraction". In: *Molecular & cellular biomechanics: MCB* 12, pp. 1–16.
- Lee, JH (2014). "A musculoskeletal model of the human hand to improve human-device interaction". PhD thesis. Arizona State University.
- Lee, JH, DS Asakawa, JT Dennerlein, and DL Jindrich (2015). "Finger muscle attachments for an opensim upper-extremity model". In: *PLoS ONE* 10.4, pp. 1–28.

- Lemay, MA and PE Crago (1996). "A dynamic model for simulating movements of the elbow, forearm, and wrist". In: *Journal of Biomechanics* 29.10, pp. 1319 –1330.
- Levangie, PK and CC Norkin (2005). *Joint structure and function: a comprehensive analysis*. 4th edition. Philadelphia (PA): F. A. Davis Co.
- Lieber, RL, BM Fazeli, and MJ Botte (1990). "Architecture of selected wrist flexor and extensor muscles". In: *The Journal of Hand Surgery* 15.2, pp. 244 –250.
- Lieber, RL, MD Jacobson, BM Fazeli, RA Abrams, and MJ Botte (1992). "Architecture of selected muscles of the arm and forearm: Anatomy and implications for tendon transfer". In: *The Journal of Hand Surgery* 17.5, pp. 787 –798.
- Linke, W and G Pfitzer (2007). "Physiologie des Menschen mit Pathophysiologie". In: 30th edition. Springer Medizin Verlag. Chap. 6 Kontraktionsmechanismen, pp. 111–139.
- Lippert, LS (2011). *Clinical Kinesiology and Anatomy*. 5th edition. F. A. Davis Co.
- Lloyd, D, RV Gonzalez, and TS Buchanan (1996). "A general EMG-driven musculoskeletal model for prediction of human joint moments". In: *Australian Conference of Science and Medicine in Sport*. Ed. by B Abernethy and M Torode. Sports Medicine Australia, pp. 236–237.
- Lloyd, DG and TF Besier (2003). "An EMG-driven musculoskeletal model to estimate muscle forces and knee joint moments in vivo". In: *Journal of Biomechanics* 36.6, pp. 765 –776.
- Lotti, F, P Tiezzi, G Vassura, L Biagiotti, G Palli, and C Melchiorri (2005). "Development of UB hand 3: early results". In: *Proceedings of the 2005 IEEE International Conference on Robotics and Automation*, pp. 4488–4493.
- Martini, FH, JL Nath, and EF Bartholomew (2012). *Fundamentals of Anatomy & Physiology*. 9th edition. Pearson Education, Inc.
- Martins, JAC, EB Pires, R Salvado, and PB Dinis (1998). "A numerical model of passive and active behavior of skeletal muscles". In: *Computer Methods in Applied Mechanics and Engineering* 151.3, pp. 419 –433.
- Ma'touq, J, T Hu, and S Haddadin (2019). "A validated combined musculotendon path and muscle-joint kinematics model for the human hand". In: *Computer Methods in Biomechanics and Biomedical Engineering* 22.7, pp. 727 –739.
- Matsuoka, Y and P Afshar (2004). "Neuromuscular strategies for dynamic finger movements: a robotic approach." In: *Conference proceedings : Annual International Conference of the IEEE Engineering in Medicine and Biology Society. IEEE Engineering in Medicine and Biology Society. Conference* 6, pp. 4649–52.

- Metcalf, CD, SV Notley, PH Chappell, JH Burridge, and VT Yule (2008). "Validation and application of a computational model for wrist and hand movements using surface markers". In: *IEEE Transactions on Biomedical Engineering* 55.3, pp. 1199–1210.
- Millard, M, T Uchida, A Seth, and SL Delp (2013). "Flexing computational muscle: model and simulation of musculotendon dynamics". In: *Journal of Biomechanical Engineering* 135, pp. 1–11.
- Mirakhorlo, M, JMA Visser, BAAXG de Monsabert, FCT van der Helm, H Maas, and HEJ Veeger (2016). "Anatomical parameters for musculoskeletal modeling of the hand and wrist". In: *International Biomechanics* 3.1, pp. 40–49.
- Miyata, N, M Kouchi, T Kurihara, and M Mochimaru (2004). "Modeling of human hand link structure from optical motion capture data". In: *Proceedings of 2004 IEEE/RSJ International Conference on Intelligent Robots and Systems*, pp. 2129–2135.
- Murray, WM, TS Buchanan, and SL Delp (2000). "The isometric functional capacity of muscles that cross the elbow". In: *Journal of Biomechanics* 33, pp. 943–952.
- Nataraj, R and Z-M Li (2013). "Robust identification of three-dimensional thumb and index finger kinematics with a minimal set of markers". In: *Journal of Biomedical Engineering* 135.9, pp. 0910021–0910029.
- Nataraj, R and Z-M Li (2015). "Integration of marker and force data to compute three-dimensional joint moments of the thumb and index finger jigits during pinch". In: *Computer Methods in Biomechanics and Biomedical Engineering* 18.16, pp. 592–606.
- Oatis, C (2016). *Kinesiology: The mechanics and pathomechanics of human movement: Second edition*. 3rd edition. Philadelphia: Lippincott Williams&Wilki.
- Parasuraman, S and CCS Zhen (2009). "Development of robot assisted hand stroke rehabilitation system". In: *International Conference on Computer and Automation Engineering*.
- Peña-Pitarch, E, JJ Yang, and K Abdel-Malek (2005). "SANTOS™ hand: A 25 degree-of-freedom model". In: *Proc. of SAE Digital Human Modeling for Design and Engineering, Iowa City, USA*.
- Peña-Pitarch, E, NT Falguera, and JJ Yang (2014). "Virtual human hand: model and kinematics". In: *Computer Methods in Biomechanics and Biomedical Engineering* 17.5, pp. 568–579.
- Pedotti, A, VV Krishnan, and L Stark (1978). "Optimization of muscle-force sequencing in human locomotion". In: *Mathematical Biosciences* 38.1, pp. 57 –76.
- Pigeon, P, L Yahia, and AG Feldman (1996). "Moment arms and length of human upper limb muscles as function of joint angles". In: *Journal of Biomechanics* 29.10, pp. 1365–1370.

- Pylatiuk, C, S Mounier, A Kargov, S Schulz, and G Bretthauer (Feb. 2004). "Progress in the development of a multifunctional hand prosthesis". In: *Annual International Conference of the IEEE Engineering in Medicine and Biology Society*. Vol. 6. IEEE Engineering in Medicine and Biology Society, pp. 4260–3.
- Qiu, D and DG Kamper (2014). "Orthopaedic applications of a validated force-based biomechanical model of the index finger". In: *2014 36th Annual International Conference of the IEEE Engineering in Medicine and Biology Society*, pp. 4013–4016.
- Rash, GS, PP Belliappa, MP Wachowiak, NN Somia, and A Gupta (1999). "A demonstration of the validity of a 3-D video motion analysis method for measuring finger flexion and extension". In: *Journal of Biomechanics* 32, pp. 1337–1341.
- Rassier, DE, BR Macintosh, and W Herzog (June 1999). "Length dependence of active force production in skeletal muscle". In: *Journal of applied physiology* 86, pp. 1445–57.
- Reddy, AC (2014). "Difference between Denavit-Hartenberg (D-H) classical and modified conventions for forward kinematics of robots with case study". In: *International Conference on Advanced Materials and manufacturing Technologies (AMMT)*. JNTUH College of Engineering Hyderabad.
- Romero, F and FJ Alonso (2016). "A comparison among different Hill-type contraction dynamics formulations for muscle force estimation". In: *Mechanical Sciences* 7.1, pp. 19–29.
- Rosen, J, MB Fuchs, and M Arcan (1999). "Performances of Hill-type and neural network muscle models – toward a myosignal-based exoskeleton". In: *Computers and Biomedical Research* 32.5, pp. 415–439.
- Sancho-Bru, JL, A Perez-Gonzalez, M Vergara-Monedero, and D Giurintano (2001). "A 3-d dynamic model of human finger for studying free movements". In: *Journal of Biomechanics* 34.11, pp. 1491–1500.
- Serbest, K, M Cilli, and O Eldogan (2015). "Biomechanical effects of daily physical activities on the lower limb". In: *Acta Orthop Traumatol Turc* 49.1, pp. 85–90.
- Serbest, K, M Cilli, MZ Yildiz, and O Eldogan (2016). "Development of a human hand model for estimating joint torque using MATLAB tools". In: *2016 6th IEEE International Conference on Biomedical Robotics and Biomechatronics (BioRob)*, pp. 793–797.
- Sharma, M, U Chhabra, S Kaushal, G Patnaik, and R Prashar (Jan. 2009). "A study of muscle morphology of anterior group of forearm muscles". In: *J Exercise Sci Physiotherapy* 5, pp. 34–37.
- Shen, ZL, TA Mondello, R Nataraj, MF Domalain, and Z-M Li (2012). "A digit alignment device for kinematic analysis of the thumb and index finger". In: *Gait Posture* 36.3, pp. 643–645.

- Sherman, MA, A Seth, and SL Delp (2013). "What is a moment arm? Calculating muscle effectiveness in biomechanical models using generalized coordinates". In: *ASME 2013 International Design Engineering Technical Conferences and Computers and Information in Engineering Conference*. Vol. 7B. Portland, Oregon, USA.
- Silder, A, B Whittington, B Heiderscheit, and D Thelen (2007). "Identification of passive elastic joint moment-angle relationships in the lower extremity". In: *Journal of Biomechanics* 40.12, 2628–2635.
- Silva, M (2003). "Human Motion Analysis Using Multibody Dynamics and Optimisation Tools". PhD thesis. Lisbon, Portugal: Instituto Superior Técnico, Universidade Técnica De Lisboa.
- Smutz, WP, A Kongsayreepong, RE Hughes, G Niebur, WP Cooney, and K-N An. (1998). "Mechanical advantage of the thumb muscles". In: *Journal of Biomechanics* 31, pp. 565–570.
- Spector, SA, PF Gardiner, RF Zernicke, RR Roy, and VR Edgerton (1980). "Muscle architecture and force-velocity characteristics of cat soleus and medial gastrocnemius: implications for motor control". In: *Journal of Neurophysiology* 44.5, pp. 951–960.
- Speirs, AD, CF Small, JT Bryant, DR Pichora, and BY Zee (2001). "Three-dimensional metacarpophalangeal joint kinematics using two markers on the phalanx". In: *Journal of Engineering in Medicine* 2015.4, pp. 415–419.
- Stillfried, G, U Hillenbr, M Settles, and P van der Smagt (2014). "The Human Hand as an Inspiration for Robot Hand Development". In: ed. by R Balasubramanian and VJ Santos. Vol. 95. Springer Tracts in Advanced Robotics. Springer International Publishing. Chap. 3: MRI-based skeletal hand movement model, pp. 49–75.
- Supuk, TG, W Harwin, and V Zanchi (2004). "Calculating positions of the finger joints centres of rotations in flexion-extension movement from reflective markers". In: *Proceedings of The IMEKO, IEEE, SICE 2nd International Symposium on Measurement, Analysis and Modeling of Human Functions*, pp. 363–366.
- Thelen, D (2003). "Adjustment of muscle mechanics model parameters to simulate dynamic contractions in older adults". In: *Journal of Biomechanical Engineering* 125, pp. 70–77.
- Thelen, DG and FC Anderson (2006). "Using computed muscle control to generate forward dynamic simulations of human walking from experimental data". In: *Journal of Biomechanics* 39.6, pp. 1107–1115.
- Thelen, DG, AB Schultz, SD Fassois, and JA Ashton-Miller (1994). "Identification of dynamic myoelectric signal-to-force models during isometric lumbar muscle contractions". In: *Journal of Biomechanics* 27.7, pp. 907–919.

- Thelen, DG, FC Anderson, and SL Delp (2003). "Generating dynamic simulations of movement using computed muscle control". In: *Journal of Biomechanics* 36, pp. 321–328.
- Tkany, C (2018). "Modeling and control of the human hand identification testbed". Student project, Institute of Automatic Control, Leibniz Universität Hannover.
- Troncossi, M, M Mozaffari-Foumashi, and V Parenti-Castelli (2016). "An original classification of rehabilitation hand exoskeletons". In: *Journal of Robotics and Mechanical Engineering Research* 1, pp. 17–29.
- Van Campen, A (2014). "Identification of the subject-specific parameters of a Hill-type muscle-tendon model for simulations of human motion". dut. PhD thesis. Katholieke Universiteit Leuven.
- Van Soest, AJ and MF Bobbert (Feb. 1993). "The contribution of muscle properties in the control of explosive movements". In: *Biological cybernetics* 69, pp. 195–204.
- Veber, M, T Bajd, and M Munih (2006). "Assessment of finger joint angles and calibration of instrumental glove". In: *Advances in Robot Kinematics*. Springer Netherlands, pp. 185–192.
- Veber, M and T Bajd (2006). "Assessment of human hand kinematics". In: *Proceedings of the 2006 IEEE International Conference on Robotics and Automation*, pp. 2966–2971.
- Vignais, N and F Marin (2014). "Analysis of the musculoskeletal system of the hand and forearm during a cylinder grasping task". In: *International Journal of Industrial Ergonomics* 44.4, pp. 535–543.
- Vilimek, M (2007). "Musculotendon forces derived by different muscle models". In: *Acta of Bioengineering and Biomechanics* 9.2, pp. 41–47.
- Ward, SR, GJ Loren, S Lundberg, and RL Lieber (2006). "High stiffness of human digital flexor tendons is suited for precise finger positional control". In: *Journal of Neurophysiology* 96.5, pp. 2815–2818.
- Weijs, WA and B Hillen (1985). "Cross-sectional areas and estimated intrinsic strength of the human jaw muscles". In: *Acta morphologica Neerlando-Scandinavica* 23, pp. 267–74.
- Wickiewicz, TL, RR Roy, PL Powell, JJ Perrine, and VR Edgerton (1984). "Muscle architecture and force-velocity relationships in humans". In: *Journal of Applied Physiology* 57.2, pp. 435–443.
- Windolfa, M, N Götzenb, and M Morlockb (2008). "Systematic accuracy and precision analysis of video motion capturing systems—exemplified on the Vicon-460 system". In: *Journal of Biomechanics* 41.12, pp. 2776–2780.

- Winters, JM (1990). "Hill-based muscle models: a systems engineering perspective". In: *Multiple muscle systems: biomechanics and movement organization*. Ed. by JM Winters and SL Woo. Springer-Verlag. Chap. 5, pp. 69–93.
- Winters, JM (1995). "An improved muscle-reflex actuator for use in large-scale neuromusculoskeletal models". In: *Annals of Biomedical Engineering* 23.4, pp. 359–374.
- Winters, JM and L Stark (1988). "Estimated mechanical properties of synergistic muscles involved in movements of a variety of human joints". In: *Journal of Biomechanics* 21.12, pp. 1027–1041.
- Wohlman, SJ and WM Murray (2013). "Bridging the gap between cadaveric and in vivo experiments: A biomechanical model evaluating thumb-tip endpoint forces". In: *Journal of Biomechanics* 46.5, pp. 1014–1020.
- Wu, G, FC van der Helm, HD Veeger, M Makhsous, PV Roy, C Anglin, J Nagels, AR Karduna, K McQuade, X Wang, FW Werner, and B Buchholz (2005). "ISB recommendation on definitions of joint coordinate systems of various joints for the reporting of human joint motion—Part II: shoulder, elbow, wrist and hand". In: *Journal of Biomechanics* 38.5, pp. 981–992.
- Wu, JZ, K-N An, RG Cutlip, K Krajnak, D Welcome, and RG Dong (2008). "Analysis of musculoskeletal loading in an index finger during tapping". In: *Journal of Biomechanics* 41.3, pp. 668–676.
- Wu, JZ, Z-M Li, RG Cutlip, and K-N An (2009a). "A simulating analysis of the effects of increased joint stiffness on muscle loading in a thumb". In: *BioMedical Engineering OnLine* 8.1, p. 41.
- Wu, JZ, K-N An, RG Cutlip, ME Andrew, and RG Dong (2009b). "Modeling of the muscle/tendon excursions and moment arms in the thumb using the commercial software anybody". In: *Journal of Biomechanics* 42.3, pp. 383–388.
- Xu, Z, E Todorov, B Dellon, and Y Matsuoka (2011). "Design and analysis of an artificial finger joint for anthropomorphic robotic hands". In: *2011 IEEE International Conference on Robotics and Automation*, pp. 5096–5102.
- Yun, M, H Jun Eoh, and J Cho (Apr. 2002). "A two-dimensional dynamic finger modeling for the analysis of repetitive finger flexion and extension". In: *International Journal of Industrial Ergonomics* 29, pp. 231–248.
- Zajac, F (Feb. 1989). "Muscle and tendon: Properties, models, scaling, and application to biomechanics and motor control". In: *Critical reviews in biomedical engineering* 17, pp. 359–411.
- Zhang, X, S-W Lee, and P Braido (2003). "Determining finger segmental centers of rotation in flexion–extension based on surface marker measurement". In: *Journal of Biomechanics* 36, pp. 1097–1102.

Publications

Journal publications

- **Ma'touq J.**, Hu T., and Haddadin S. (2019). 'A Validated Combined Musculotendon Path and Muscle-joint Kinematics Model for the Human Hand'. In: *CMBBE*, 22(7), pp. 727 - 739.
- **Ma'touq J.**, Hu T., and Haddadin S. (2018). 'Sub-millimetre Accurate Human Hand Kinematics: From Surface to Skeleton'. In: *CMBBE*, 8(3), pp. 113-128.
- Al-Nabulsi J., **Ma'touq J.**, Abdullah E. E., Haloubi T., and Manasra Ali. (2017). 'Blind Users Assistive Technology Based on Android Platform'. In: *IJICA*, 8(3), pp. 162-171.
- **Ma'touq J.**, Al-Nabulsi J., Al-Kazwini A., Baniyassien A., Al-Haj Issa G., and Mohammad H. (2014). 'Eye Blinking-Based Method for Detecting Driver Drowsiness'. In: *J. Med. Eng. Technol.*, 38(8), pp. 416-419.
- **Ma'touq J.**, Messenger N., Strauss D., Tayebjee M. and Stewart T. (2014). 'Spinal Angle and Foot Pressure During Cardiac Electrophysiological Procedures'. In: *Int. J. Cardiol.*, 172(3), pp. 398-400.
- Fraiwan, L., Al-Bataineh, O., **Ma'touq J.**, Haddad, S. and Bani-Amer, M. (2009). 'ECG-based Wireless Home Infant Apnoea Monitor'. In: *J. Med. Eng. Technol.*, 33(4), pp. 309-313.

Conference publications

- **Ma'touq J.** (2019). 'An Index Finger Musculoskeletal Dynamic Model'. In: *The 16th International Symposium on Computer Methods in Biomechanics and Biomedical Engineering*, New York City, United States.
- **Ma'touq J.** (2019). 'Anatomical Correct Human Hand Neuromusculoskeletal Model for Virtual Rehabilitation'. Poster presentation at: *The 16th International Symposium on Computer Methods in Biomechanics and Biomedical Engineering*, New York City, United States.
- Hu T., Kühn J., **Ma'touq J.**, and Haddadin S. (2018). 'Learning and Identification of Human Upper-limb Muscle Synergies in Daily-life Tasks with Autoencoders'. In: *OTWorld Congress*, Leipzig, Germany.

Curriculum Vitae

Name: Jumana Ma'touq
Date of birth: 13.06.1985
Place of birth: Amman, Jordan

Education

2015 - Present PhD Candidate
Institute of Automatic Control
Gottfried Wilhelm Leibniz Universität Hannover, Germany
2011 - 2012 MSc Medical Engineering
University of Leeds, UK
2003 - 2008 BSc Biomedical Engineering
Jordan University of Science and Technology, Jordan

Professional experience

2014 - 2015 Lecturer and Graduation Projects Coordinator
Department of Biomedical Engineering
German Jordanian University, Jordan
2013 - 2014 Lecturer
Department of Biomedical Engineering
Amman Al Ahliyyah University, Jordan
2010 - 2011 Teaching and Research Assistant
Department of Biomedical Engineering
German Jordanian University, Jordan
2009 - 2010 Logistic Support Engineer
Dallah Medical Co., Jordan
2008 - 2009 Sales Supervisor Assistant
United Medical and Electronic Co., Jordan

